2010

The Design and Validation of a Novel Computational Simulation of the Leg for the Investigation of Injury, Disease, and Surgical Treatment

Joseph Iaquinto
Virginia Commonwealth University

The Design and Validation of a Novel Computational Simulation of the Leg for the Investigation of Injury, Disease, and Surgical Treatment

A dissertation submitted in partial fulfillment of the requirements for the degree of
Doctor of Philosophy at Virginia Commonwealth University

By

Joseph Michael Iaquinto
B.S. Virginia Commonwealth University 2004
M.S. Virginia Commonwealth University 2006
Ph.D. Virginia Commonwealth University 2010

Director: Dr. Jennifer S. Wayne
Professor
Biomedical Engineering

Virginia Commonwealth University,
Richmond Virginia
May 2010

Acknowledgements

"Acknowledgements" paints the mental picture of an end-of-lecture nod to someone unseen in the audience, I prefer a firm handshake and warm smile of thanks, and thus re-name this page the "thank you".

I would first like to thank my advisor and mentor Dr. Jennifer Wayne. Over the course of my education at this institution she has maintained a fantastic balance between supportive encouragement, very constructive criticism and guidance towards self improvement as a researcher. Dr. Wayne has always made the time to enlighten myself and others in details ranging from the tenure process, to external funding sources, to the intricate organization of professional societies. Her willingness to share her valuable experiences along with her dedication, time and effort in guiding this research are noticed and very appreciated.

In the medical field I thank Dr. Robert Adelaar for serving both on my masters and doctoral committees. Dr. Adelaar has always shown very strong support and excitement over the potential uses for my work, and that has been a great source of encouragement to a developing medical researcher. Also Dr. Curtis Hayes for his support with medical scanning at the MCV radiology department, he has spent considerable time describing the abilities and limitations of the various imaging techniques available.

I wish to thank John Owen, who is a phenomenal friend and colleague. His ability to identify, calculate and engineer solutions to all manner of hurdles associated with laboratory function is inspirational. He has a fantastic sense of humor which, coupled with his unending supply of mints, can fuel tedious research deep into the night.

I would like to acknowledge the support and kind words of Dr. Gerald Miller, who has always made me feel welcome and leaves me with a smile. Joyce Wilkins, who is a good friend and fantastic person, I have enjoyed knowing her over the years. As well as Norma Briggs who has been very helpful in my endeavors. I also thank my dissertation committee for taking the time to review this work and past works of mine; they have given me much encouragement and very helpful criticism. I would like to thank my fellow graduate students, particularly Peter Liacouras, Kelly Shields, Karin Wartella, Justin Fisk, and Meade Spratley all of whom I have been very happy to have met and worked with. Karin has been a fantastic and supportive office colleague and Meade is very helpful in finding clever solutions to challenging problems. I would like to thank the numerous undergraduates, graduates and clinical researchers who have shown support and interest in my work over the years, they are too numerous to list but every question, criticism, suggestion and attentive audience they have given me worked to strengthen my dedication to this field and the wonderful, intelligent people that work in it.

I would like to thank my girlfriend Geneviève who, also as a doctoral student, has been very understanding of my schedule and extremely supportive of my work. Her sunny disposition, wonderful intellect and great sense of humor are a joy to experience.

Last but certainly not least I would like to thank my parents Jo and Joseph. They both posses the intelligent and deep minds of engineers and thus bestowed me both with great genetics and a loving and encouraging upbringing. Their support has been coupled with that of my brother, Jonathan, who is the best sibling anyone could ask for. They have shown me how to excel in the face of adversity, laugh at the humor in life, and what it means to have family.

Table of Contents

List of Figures

List of Tables

List of Equations

List of Abbreviations

AAFD	Adult Acquired Flatfoot Deformity
AP	Anteroposterior View
AP-T1MT	AP Talo 1st Metatarsal Angle
AP-TN	AP Talonavicular Angle
CCDA	CalcaneoCuboid Distraction Arthrodesis
CT	Computed Tomography
DICOM	Digital Imaging and COmmunications in Medicine
Evans	Evans opening wedge osteotomy
FEA	Finite Element Analysis
IGES	International Graphics Exchange Specification
L-T1MT	Lateral Talo 1st Metatarsal Angle
L-TC	Lateral Talocalcaneal Angle
L-CP	Lateral Calcaneal Pitch
LCL	Lateral Column Lengthening
MCO	Medializing Calcaneal Osteotomy
MRI	Magnetic Resonance Imaging
MIMICS	Materialise's Interactive Medical Imaging Control System
mm	Millimeter
N	Newton
N/mm	Newtons per millimeter
PTT	Posterior Tibial Tendon

SIMM	Software for Interactive Musculoskeletal Modeling
TKA	Total Knee Arthroplasty
Voxel	Volumetric Pixel
VIMS	Virtual Interactive Musculoskeletal System
2D	Two Dimensional
3D	Three Dimensional
.stl	Stereolithographic file format
°	Degree
±	Plus or Minus
%	Percent

Abstract

THE DESIGN AND VALIDATION OF A NOVEL COMPUTATIONAL SIMULATION OF THE LEG FOR THE INVESTIGATION OF INJURY, DISEASE, AND SURGICAL REPAIR.

By Joseph Michael Iaquinto, M.S.

A dissertation submitted in partial fulfillment of the requirements for the degree of Doctor of Philosophy in Biomedical Engineering at Virginia Commonwealth University.

Virginia Commonwealth University, 2010.

Major Director: Jennifer S. Wayne, Ph.D.
Professor, Biomedical Engineering & Orthopaedic Surgery; Director, Orthopaedic Research Laboratory

Computational modeling of joints and their function, a developing field, is becoming a significant health and wellness tool of our modern age. Due to familiarity of prior research focused on the lower extremity, a foot and ankle 3D computational model was created to explore the potential for these computational methods. The method of isolating CT scanned tissue and rendering a patient specific anatomy in the digital domain was accomplished by the use of MIMICS™ , SolidWorks™, and COSMOSMotion™ – all available in the commercial domain. The kinematics of the joints are driven solely by anatomically modeled soft tissue applied to articulating joint geometry. Soft tissues are based on highly realistic measurements of anatomical dimension and behavior. By restricting all model constraints to true to life anatomical approximations and recreating their behavior, this model uses inverse kinematics to predict the motion of the foot under various loading conditions. Extensive validation of the

function of the model was performed. This includes stability of the arch (due to ligament deficiency) and joint behavior (due to disease and repair). These simulations were compared to a multitude of studies, which confirmed the accuracy of soft tissue strain, joint alignment, joint contact force and plantar load distribution. This demonstrated the capability of the simulation technique to both qualitatively recreate trends seen experimentally and clinically, as well as quantitatively predict a variety of tissue and joint measures. The modeling technique has further strength by combining measurements that are typically done separate (experimental vs. clinical) to build a more holistic model of foot behavior. This has the potential to allow additional conclusions to be drawn about complications associated with repair techniques. This model was built with the intent to provide an example of how patient specific bony geometry can be used as either a research or surgical tool when considering a disease state or repair technique. The technique also allows for the repeated use of anatomy, which is not possible experimentally or clinically. These qualities, along with the accuracy demonstrated in validation, prove the integrity of the technique along with demonstrating its strengths.

Chapter 1 - Introduction

1.1 Computational Modeling

Investigative methods for studying health problems are numerous and diverse. In the field of orthopaedics these methods include: prospective or retrospective clinical studies which report direct patient outcomes, which contain limits in evasive observation and measurement; in vitro tissue or cellular studies that allow for vastly increased ability to observe and measure outcomes, but are by definition limited to the target tissue or sample; and computational modeling, which grants the ability to reuse identical specimens in perpetuity as well as observe a multitude of effects in ways that are not feasible clinically and experimentally. Such computational studies are limited by the knowledge base of material behavior as well as the modelers' capability to realistically depict native tissue. The focus of this work was at the computational level. This work details the development of a simulation method which uses patient specific bone geometry and realistic ligament restraint to recreate native tissue behavior. This is an effort to develop a clinically and experimentally useful tool for disease/surgical outcome prediction and analysis.

Considering the utility of computational modeling, these methods are capable of demonstrating extensive improvement in predicting the results of a study when used in conjunction with traditional forms of research (i.e. *in vitro, in vivo, in situ* etc…). Such models could be used to investigate prototype improvements in surgical procedure by applying theoretical hardware and various tissue procedures (both soft tissue and bony) to an anatomical database. These models could also be used in reconstructive surgery to visualize bony three-dimensional architecture and soft tissue location, aiding the surgeon in the reconstructive

process. As presented here, these models can evaluate soft tissue and bony anatomy in combinations of disease, injury and repair. Such evaluation can be extremely potent in revealing joint angles/contact loads, overall foot morphology, ligament strain/load, and plantar contact distributions; quantities which are otherwise difficult to evaluate either in live subjects or experimentally. These results can not only show the potential success for a treatment, but identify key areas of concern that can lead to complications later in life.

The benefits of computational modeling have been recognized by researchers in the development of a variety of existing orthopaedic computational models. Computational techniques are currently in use in four major ways in the field of orthopaedic joint kinematics.

1.2 Computational Use

The first major use of these methods is in Finite Element Analysis (FEA) of limb/joint structure. A model for Total Knee Arthroplasty (TKA) contact stress and contact area was developed with FEA with comparison to a previously documented physical knee simulation[1]. Anderson et al. developed a FEA model of the tibio-talar joint for concurrent comparison with contact stress in the same anatomical geometry used with cadaveric experimentation[2]. Cheung, et al. have published extensively in the past few years documenting a Magnetic Image (MR) derived foot model for FEA application[3-8]. Their model was developed and validated with mechanically tested cadaver geometry. Their technique was used to investigate the effects of a variety of footwear and shoe orthotics[3-5].

The second major approach to joint level orthopaedic computational modeling is an experimental kinematics study. These studies are ways of modeling and then viewing behavior that is otherwise difficult to observe and quantify, such as internal contact in the knee. These techniques are a combination of Computed Tomography (CT) and/or Magnetic Resonance (MR)

scan imagery of live patient movement which are used in conjunction with various motion capture systems. Li et al. have published extensively in this field to study knee kinematics. This method uses a dual plane fluoroscopic motion capture on the femur and tibia during various activities and superimposes MR scan derived geometry onto these motion images. From such data various measures of ACL, PCL, and medial & lateral menicscal contact can be made[9-12]. Similar methods are being explored by Tashman et al. using a CT based approach and high-speed biplane radiography[13]. Research focus for these works was cartilage interaction and determination of 3D spatial motion of bones during activities[14,15]. These methods were also explored for the shoulder[16]. These kinematic approaches for investigation exhibit strength in accurately quantifying 3D motion of bones at joints, which has yielded information about contact location, pressures, and tissue strains for *in situ* moving joints. These methods provide excellent data to analyze the results of a procedure or the behavior of an injury state, but require significant patient contact pre- and postsurgical. These methods are also pure motion studies with little investigation into joint internal loading.

The third major approach uses inverse kinematics. These mathematical or computational models are predictors of internal tissue forces and strains. Such prediction is made by using a purely motion capture kinematics method, then applying analytical dynamics to calculate the specific joint biomechanics such as contact forces and ligament strain. They are used extensively in research of gait and other movement analysis. Dao et al.[17] performed a sensitivity study on the selection of patient parameters such as height and muscle cross sectional area. That study highlighted the importance of physiological parameter selection in obtaining lower error rates when considering joint function and motion – this was a combination forward and inverse kinematics study. Leanerts et al.[18] performed an inverse kinematic study on the hip. By varying,

again, patient parameters they established the importance of subject specific information in determining accurate hip contact force, moments, and muscular forces. Stief et al.[19] performed a combination motion and force study which used inverse kinematics to calculate moments during various methods of walking and running. The biomechanical benefit of these techniques, to persons who may have weak lower extremities, was rated by the magnitude of moment and forces generated by the activities. These methods again require extensive patient contact and measurement during activities to perform inverse kinematic investigation of joint function.

The fourth major approach to joint level orthopaedic computational modeling is a forward kinematic approach. The forward kinematic method is a predictive model of motion, based on pre-programmed material behavior and boundary/external constrains. This is achieved by accurately reproducing the behavior of a joint or joint system, such that it is capable of predicting that structures response to internal or external perturbation. Such works have been used in purely mathematical models of motion to predict how alterations in movement patterns from damage or training can impact gait or sports activities[20-22]. The bulk of such methods use a simplified system of formulaic relations to describe joint motion and body position based on general limb dimensions, estimated joint torques and muscle activation. There are examples of extensive models of this technique, which are used to create a simplified motion model of the human body. Two commercially available motion analysis programs are SIMM (Software for Interactive Musculoskeletal Modeling) and VIMS (Virtual Interactive Musculoskeletal System). SIMM is a prefabricated musculoskeletal system that defines kinematics based on muscular activation. This software contains a standardized skeleton and controls motion with simplified joint primates (i.e. ball/socket, hinge) and not by defining motion based on articulating anatomical geometry and corresponding ligament and musculature anatomy. SIMM has

extensive utility in analyzing motion schemes based on muscular contraction and anatomy, and has been used to investigate joint contact force and internal bony loading[23,24]. VIMS is a tool described as a database of anatomy and tissue mechanical behavior coupled with static and dynamic analysis tools. The system has been used in several publications but it is not currently available to the public[25-27].

The modeling approach discussed in this work incorporates the strengths of 3D rigid body motion simulation, based on patient anatomy and coupled with a forward kinematic approach which approximates joint behavior to predict response. This method provides a tool that will fill a niche in current modeling techniques. The purpose of this tool is to augment research power by creating predictive musculoskeletal models. As mentioned, the research community has tools to analyze soft and hard tissue deformation at a tissue and joint level and to inversely derive the conditions present at joints based on patient motion – but anatomically accurate patient specific motion predictors are currently not available.

These methods can be applied to any joint of the human body and modified by any existing surgery or disease that alters material behavior and geometry. For the purposes of this study and due to prior research in this area, the foot and ankle region was considered for modeling. The creation of such a patient specific foot and ankle model, to which a variety of disease and injury states can be simulated, will prove to be an invaluable assistive tool in treating the particular deficiencies of that patient's anatomy with tailored fit treatment. The development of this approach is detailed in the following chapters and incorporates CT derived bony anatomy, anatomical ligament geometry and soft tissue behavior. This technique recreates disease/repair states to generate a model that can be used in conjunction with reported experimental and clinical findings to obtain a more detailed perspective of common foot and ankle conditions. This model

allows the user extensive freedom to create and apply external and internal loading as well as physical objects such as surgical hardware to simulate their effect on joint function. The model was validated by several comparisons to experimental findings. One area of validation was accomplished by simulating soft tissue contribution to arch stability and soft tissue strain in the presence of a fascia release surgery (fasciotomy). Another validation was performed by simulating Adult Acquired Flatfoot Deformity (AAFD) and its repair methods. The results of that model were compared to experimental and clinical findings. From a developmental standing, throughout this work methods were identified to increasing model stability, automate/standardize model creation and reduce computation time. All of the methods and software used in this development are in the commercial market.

Chapter 2 - Background

2.1 Previous Modeling Technique

Computational modeling was first investigated in this laboratory with a previous foot model that focused on ankle function[28]. This model used geometry from the male CT dataset of the National Library of Medicine's, Visible Human Project (NLM-VHP) (U.S. National Library of Medicine, Bethesda, MD). This data was processed in MIMICS (Materialise's Interactive Medical Imaging Control System, Materialise, Ann Arbor MI) to create IGES (Initial Graphics Exchange Specification) files. These files were arrays of stacked 2D curves of the bones of the foot which described high resolution axial profiles of long bone geometry. This geometry was imported to SolidWorks (SolidWorks Corporation, Concord MA) to form surface geometries that were further processed to yield solid bone geometry. These bones were then assembled to yield the hind-, midfoot and ankle. In COSMOSMotion (a SolidWorks add-on) a network of linear spring elements were added to simulate the soft tissue constraint imparted by ligaments. The ligaments and consequent bony motion modeled was restricted to the ankle joint and movement of the talus, tibia and fibula. This technique and subsequent validation and sensitivity investigations were focused at the ankle level. Validation was performed with a series of simulations of experimental and clinical studies. Comparisons were made which showed that under a variety of simulated injury and surgical configurations the model demonstrated agreement with results pertaining to bony rotations and ligament contribution to ankle stability[28].

With the success of this previous model established and having cultivated a further interest in computational modeling, the work presented here is both a continuation of the previous model in terms of creating a more detailed and comprehensive foot simulation model,

and a vast divergence from much of this previously established methodology and technique. These new approaches and further depths of simulation detail increase flexibility, computational stability, and the potential usefulness for these simulations.

2.2 Foot Anatomy

To properly introduce the foot and ankle and put into perspective the task undertaken here, the following section will describe the anatomy which was studied and modeled. The figures in the following section are 3D reconstruction of actual bone anatomy. All images are of a right leg and have been drawn with guidance from anatomy text[29,30], literature[31-34] and in-house dissection. This anatomical description should serve to put into perspective the scope of bony and soft tissue anatomy this technique seeks to address. This includes the size disparity between some of the modeled bones, the variety of bony features, the combinations of both two dimensional and three dimensional ligament structures and the interplay between all of the architecture from distal knee to distal phalange. Hopefully this description will also impart some of the reverence the author has developed for this intricate and beautiful structure which supports us in our daily lives.

Bone and Joint

Considering the lower extremity, there are a number of significant joints: the femoral acetabular articulation (hip), tibiofemoral (knee) and tibiotalar (ankle). Further distal are the multitude of articulations of the foot. For the scope of this work, our most proximal interest is in musculature originating from the femur. The distal posterior supracondylar aspect of the femur is the origin of the dual heads of the gastrocnemius muscle. The gastrocnemius is one of the two muscles which, distally, form the Achilles tendon. From the floor of the knee joint down, the

two bones of the leg are the tibia and fibula (Figure 2.1). The fibula is tied to the tibia with a thick sheet of material called the interosseous membrane and a proximal and distal fibrous articulation.

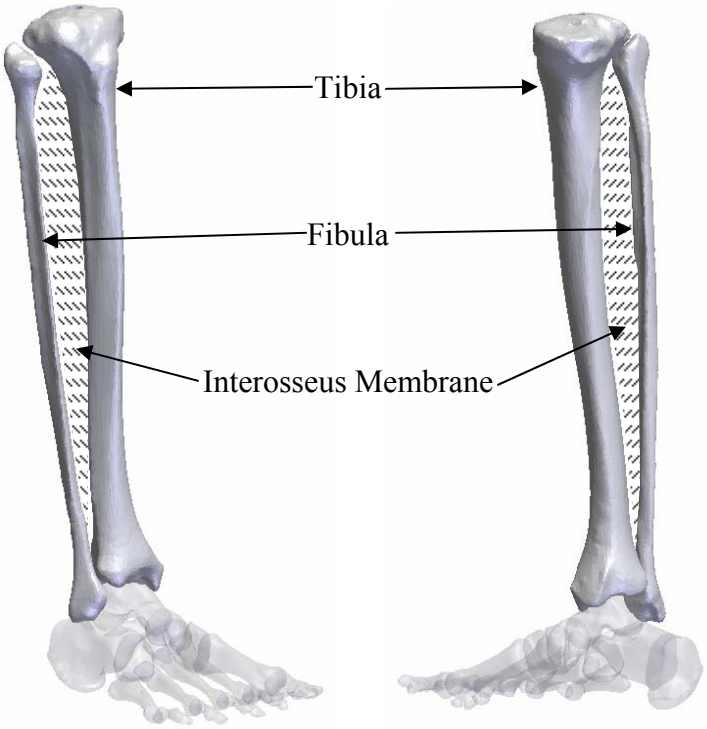

Figure 2.1: Bones of the Leg. The tibia and fibula, pictured above in the anterolateral (left) and the posteromedial (right) views. These two bones comprise the bony anatomy of the leg. The interosseous membrane runs the length of the facing surfaces of these bones (hatched). Right leg, foot semi-transparent for orientation.

The tibia is by far the larger of the two, making a clear supportive pillar between the knee and ankle. The fibula is load bearing but functions more for stability at the ankle by creating portions of the ankle joints' bony anatomy. The fibula also provides, in conjunction with the tibia and the interosseous membrane, a broader bony field to which large muscles of the leg can originate. Distally, the tibia and fibula each possess a bony prominence called a malleolus which

serves both to restrict motion at the ankle as well as to provide ample bony anatomy for the anchoring of numerous ankle ligaments (discussed in the next section) (Figure 2.2). The composite of these two joined bones is rigid enough to provide the support needed for ambulation, cooking pizza, fencing, gymnastics, etc… while simultaneously providing enough flexibility to allow for the ankle to operate in a full range of motion under such crushing impacts.

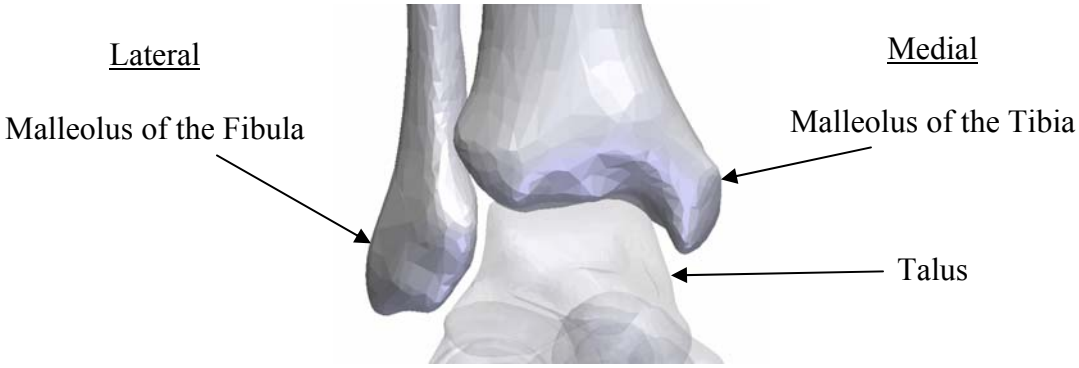

Figure 2.2: Maleoli of the Ankle. Anterior view of the medial and lateral maleoli clearly. These structures form the bony sides of the ankle joint as they encapsulate the talar body.

Of greater role in this model are the bones of the foot and their articulations. The talus and calcaneus together comprise the hindfoot. Immediately forward of these bones are the bones of the midfoot: the cuboid, with its calcaneal articulation at the calcanealcuboid joint; the navicular which articulates against the anterior talus; and the cuneiforms - medial, intermediate and lateral. The cuboid and cuneiforms together articulate with the forefoot. The forefoot is composed of five metatarsals and fourteen phalanges, three phalanges to each toe except the great toe with only two (the same distribution as the hand). Each metatarsal with its associated phalangeal column is known as a ray, with the great toe belonging to the first ray. The smallest toe which is also the most lateral belongs to the fifth ray. The first ray has its root almost exclusively on the medial cuneiform. Rays two through four may share some slight overlapping

origin on the medial, intermediate and lateral cuneiform as well as the distal cuboid. The fifth ray articulates exclusively with the distal cuboid (Figure 2.3).

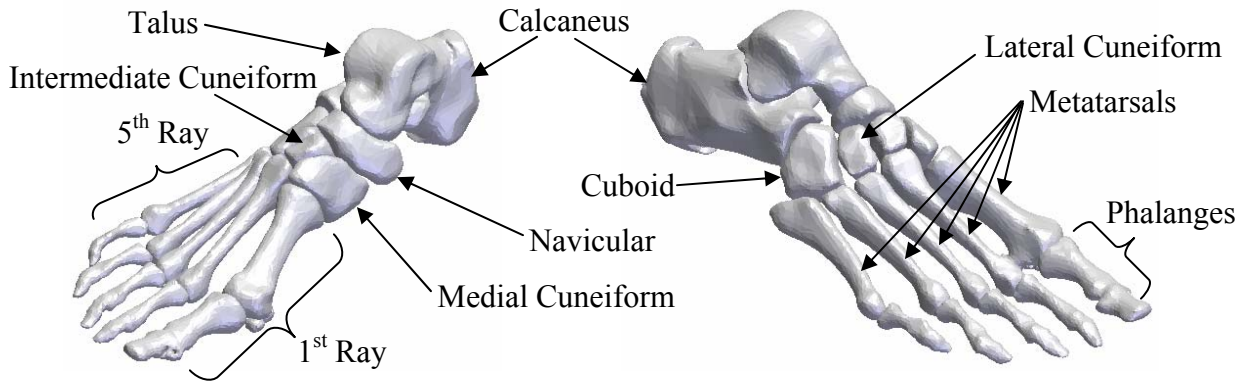

Figure 2.3: The Foot. Anteromedial (left) and lateral (right) views of the right foot. These perspectives help visualize the full bony anatomy. The demarcations of the hind-, mid-, and forefoot bones are clear, as are the structures of the rays.

Returning to the hindfoot and specifically the major articulator at the ankle joint is the talus, a distinct bone of the hindfoot that is sculpted with numerous articular facets above, fore, aft, astride and beneath. The talus lies across the splayed anatomy of the calcaneus, the largest bone of the foot. The talus articulates with the calcaneus at several of its extensive articular facets both on the superoanterior body as well as on the winging architecture of the sustentaculum tali and the anterior body of the bone. The calcaneus, in addition to supporting the talus and with it forming the subtalar hindfoot articulation, also possesses an anterior articular facet for the cuboid. The posterior of the calcaneus is a large prominent tuberosity that is the insertion site of the Achilles tendon (Figure 2.4).

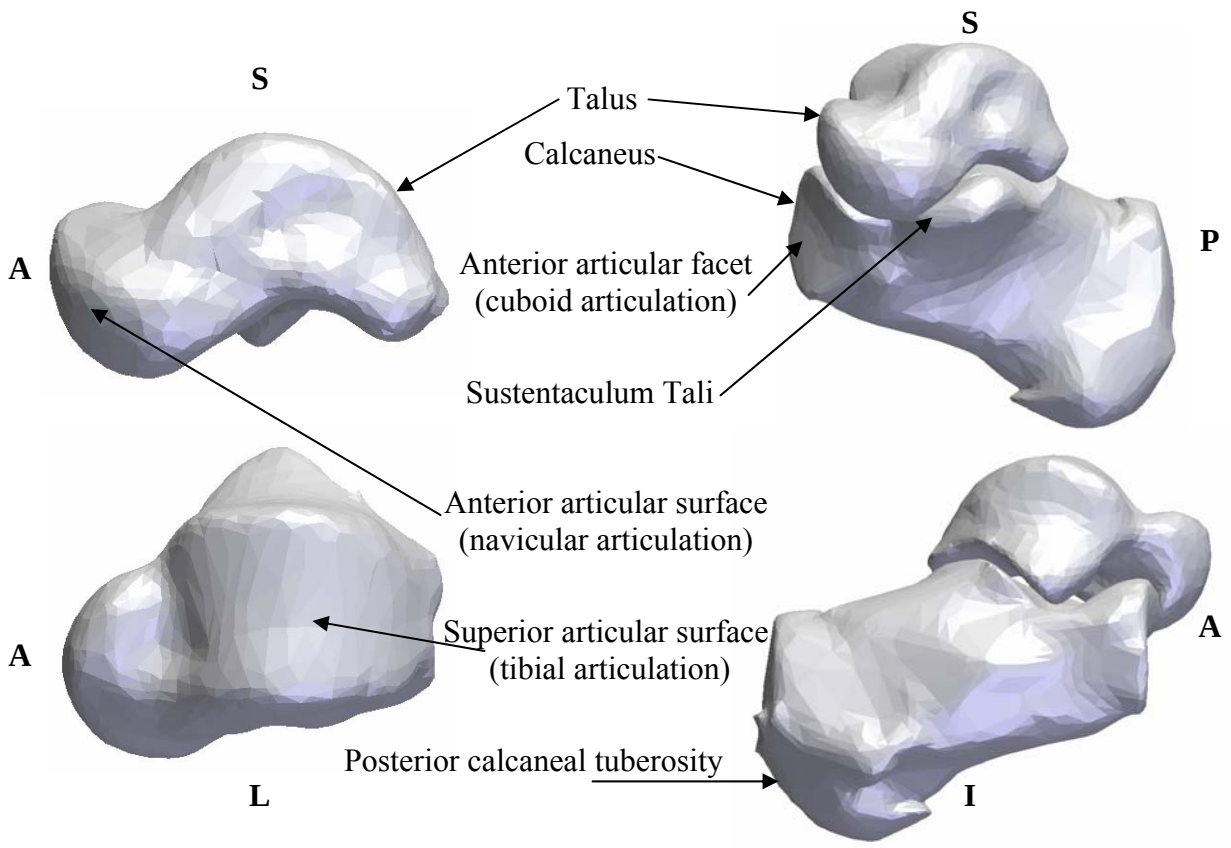

Figure 2.4: The Hindfoot. View of the talus (left) and the complete hindfoot articulation (talus and calcaneus, right). Orientation is given with respect to Anterior (A), Posterior (P), Superior (S), Inferior (I) and Lateral (L) aspects. Major articular features are identified on both of these bones. The subtalar joint is a complex articulation between the talus and the calcaneus as depicted in the right set of images.

The origin of the gasterocnemius, one of the muscles which form the Achilles tendon, was discussed prior as on the posterior femur. The second muscle forming the Achilles tendon, the soleus, originates across the deep posterior compartment of the leg formed. This compartment is formed by the interaction of the tibia, fibula, and interosseous membrane. The tendon itself is quite robust, easily shouldering up to several hundred Newton's of force – an

importance that will be more significant during discussion of a disease of the foot. These bones act together to create some important supportive geometry. The flow of the talus and calcaneus around each other forms the foundation of an arch lying in the sagittal plane and extending down the long axis of the foot. Observing the architecture of the foot from the medial side one can see this arch clearly, formed by the line of the calcaneus, talus, navicular, medial cuneiform, and the first ray. The apex of this arch is roughly centered on the talonavicular articulation (Figure 2.5, left). From the lateral perspective, there is a very mild arch formed by the calcaneus, cuboid and fifth ray, this architecture has been referred to as an arch but more commonly as the lateral column due to its relative straightness (Figure 2.5, right).

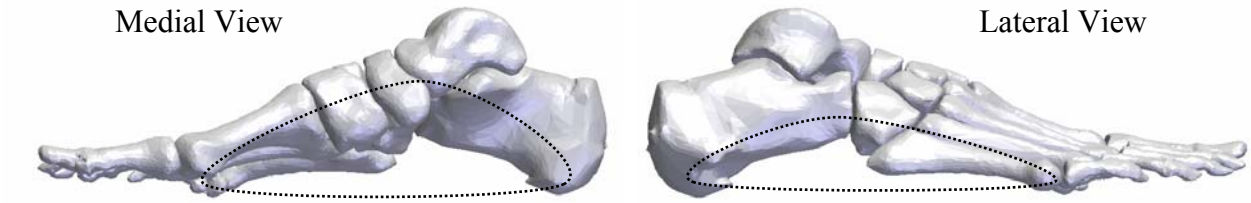

Figure 2.5: The arches of the Foot. Views of the medial and lateral arches. These are highlighted by a superimposed arch following the medial arch geometry, left; and the lateral column similarly, right. Note the difference in distance to ground between the 1st and 5th metatarsal base as well as the distance of the navicular and cuboid bones to the ground.

Ligament

While the position of the bones is assisted by their interlocking shape and well mated articular surfaces, ligaments provide the bulk of the connective support between the bones. At the deepest tissue levels these bones are small and close enough that their joint capsules merge almost completely to encase the foot in a mesh of soft tissue. There are notable thickenings of this network around sites of importance of the ankle: the fibulocalcaneal, anterior and posterior fibiotalar, and medial talocalcaneal which act as a lateral counterpart to the deltoid ligament and

provide support against inversion; the tibiofibular which bind the bones of the leg distally (Figure 2.6); the anterior and posterior tibiotalar ligaments, which tie the leg and foot by crossing and supporting the medial ankle joint, in conjunction with the medial tibiocalcaneal; and the tibionavicular ligament. These large groups of medial bands are known together as the deltoid ligament, which stabilize the ankle against eversion (Figure 2.7).

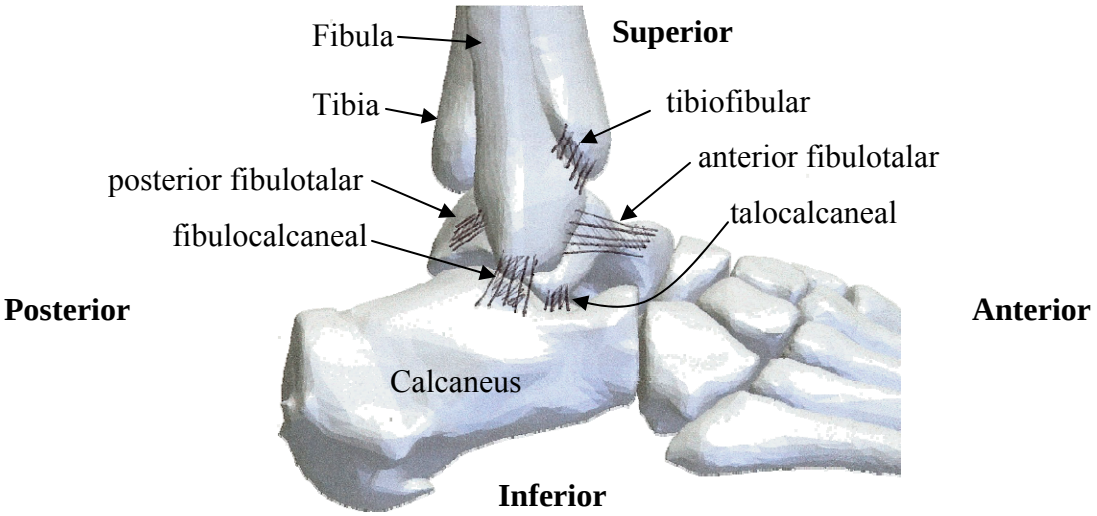

Figure 2.6: Lateral Ankle Ligaments. Major structures of the lateral ankle joint. Ligament shape and placement represented from dissection, anatomy text[29,30], and literature[31-34].

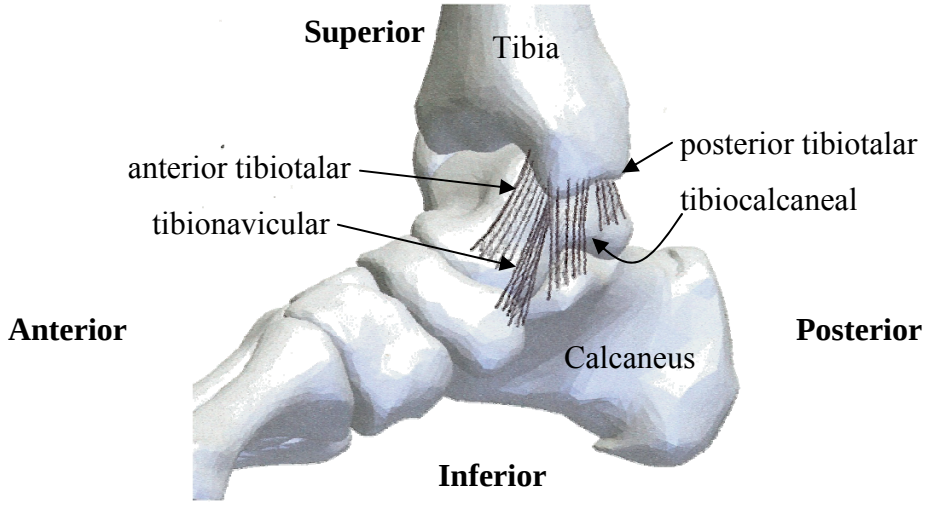

Figure 2.7: Medial Ankle Ligaments. Major structures of the medial ankle joint, the deltoid ligament. Shape and placement represented from dissection, anatomy text[29,30], and literature[31-34].

A structure of particular importance to the stability of the medial arch is the capsule network around the talonavicular joint, remembering that this site is the apex of the medial arch. The thickened bands of ligament about this structure are known as the spring ligament. The spring ligament has superior, medial, and inferior portions. The superior portions also include the tibionavicular ligament which passes over the talus. The medial portions are slighter, supported by the tibialis posterior tendon (discussed in the next section), and include bands of the calcaneonavicular ligament. The inferior portions are typically the thickest bands (Figure 2.8). The inferior spring ligament serves not only to maintain joint unity, but as part of the joint architecture itself. This thickened ligament may contain thin regions of articular cartilage and even bone, which aid in supporting load as the talonavicular joint resists depression under loading. The origin of the inferior spring ligament is centered around the anteromedial calcaneus and its sustentaculum tali. Nearby ligament bands arise from the cuboid and are known as the cuboideonavicular ligament – these are not associated with the spring ligament complex.

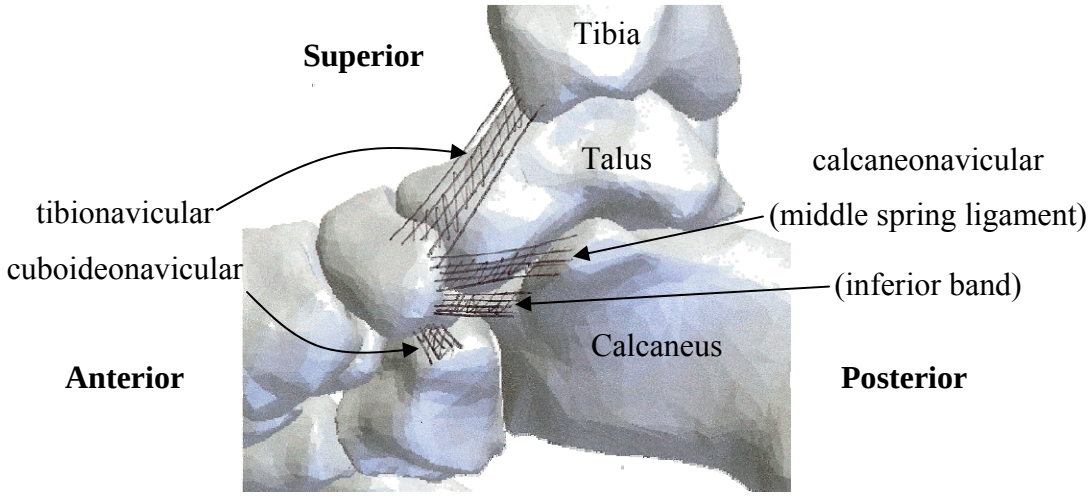

Figure 2.8: The Spring Ligament. Major portions of the spring ligament complex as viewed medially. Shape and placement represented from dissection, anatomy text[29,30], and literature[31-34]

The physically more extensive ligaments of the foot are the long and short plantar ligaments, and the plantar fascia (aponeurosis). The long and short plantar ligaments originate on the inferior and middle/posterior surface of the calcaneus; they are of middle depth in the arch of the foot. The short plantar ligament (also known as the plantar calcaneocuboid ligament) crosses the calcaneocuboid joint with some bands crossing to and inserting into the cuneiforms. The long plantar ligament goes further, extending to the distal cuboid and cuneiforms distal with attachment into the proximal metatarsal bases (Figure 2.9).

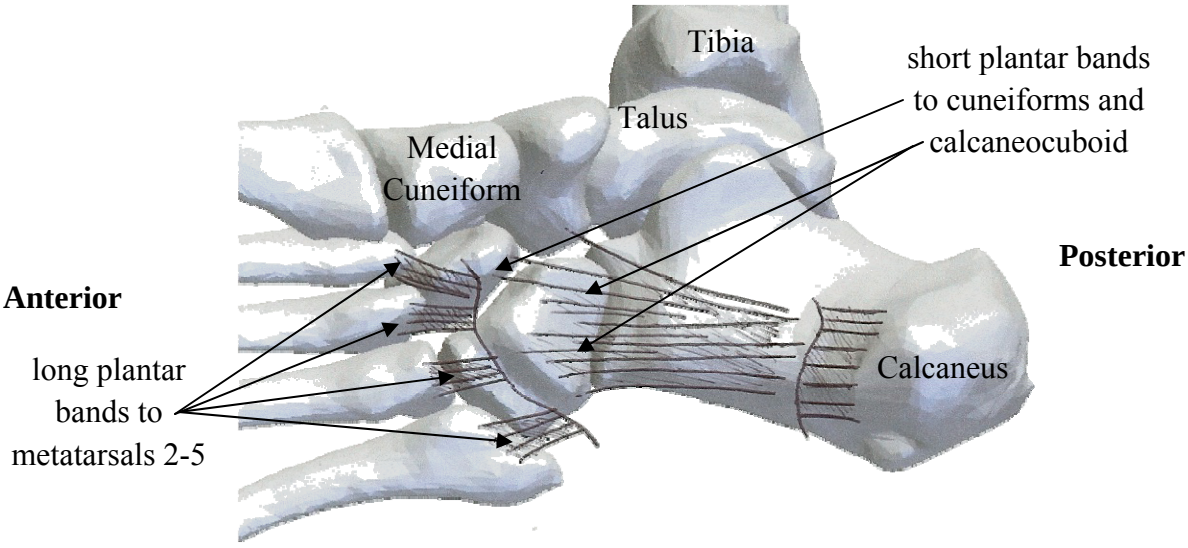

Figure 2.9: The Long and Short Plantar Ligaments. Both short and long (cut to see short) portions of the plantar ligament (shown in an inferior perspective). This is a very 3 dimensional structure with both proximal and distal midfoot insertions including attachment to metatarsal bases. Shape and placement represented from dissection, anatomy text[29,30], and literature[31-34].

The plantar fascia is a broad sheet that is very superficial, inferiorly, in the foot. This tissue is found integrated onto the deepest layers of skin of the sole of the foot. The plantar fascia has its origin inferior on the calcaneus and very posterior, tending to seat just under the lip

of the posterior calcaneal tuberosity – the Achilles insertion. This band of tissue flows across the whole of the arch of the foot, passing the insertions of the long and short plantar ligament, around the metatarsal heads, to finally insert at the base of the proximal phalanges (Figure 2.10). By wrapping around the forefoot geometry this way, the fascia can be tightened by merely extending the toes with no other changes to foot position. This extensive wrapping and toe tightening has been referred to as the "windlass mechanism" of the foot. There are numerous other ligaments of note in the foot and ankle; however the abovementioned are not only the largest and most robust of the structures of the foot, but also play key roles both in the development of this model as well as in the injury and disease states simulated to validate it.

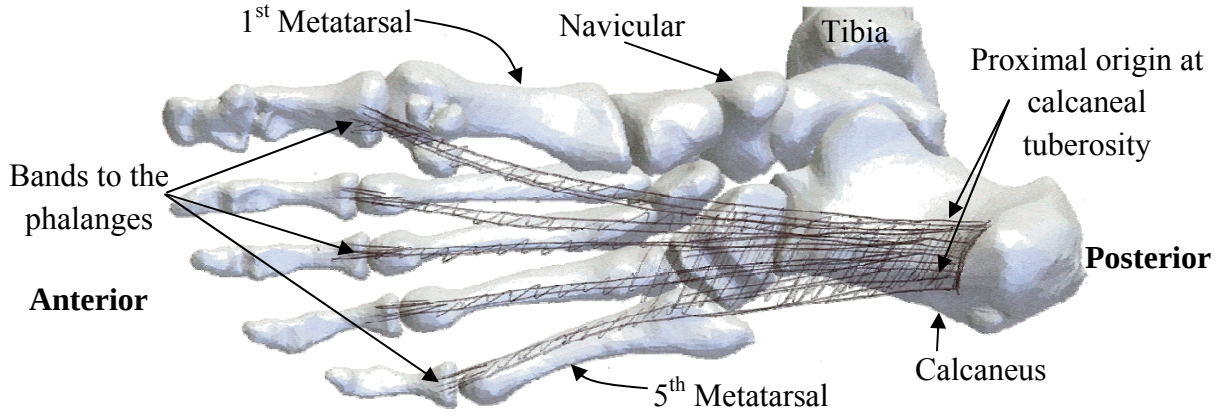

Figure 2.10: The Plantar Fascia. The structure of the plantar fascia shown in an inferior perspective. This includes its common origin at the posterior tuberosity to its distal insertions around the metatarsal heads to the phalanges. Note the splaying of the fibers at the midfoot / forefoot level. Ligament shape and placement represented from dissection, anatomy text[29,30], and literature[31-34].

Musculature

A variety of musculature acts on the foot to provide arch support, balance, and locomotive power. Mentioned previously were the gastrocnemius and soleus muscles which

together form the Achilles tendon. Also of particular note to this work is the tibialis posterior muscle. The tibialis posterior originates in the deep posterior compartment of the leg, its tendon runs medial, coursing around the medial malleolus of the tibia. The tendon passes the talus to find insertion on the posteromedial border of the navicular (Figure 2.11). This insertion is shared with elements of the spring ligament. The location and line of action of this tendon allows the tibialis posterior to both stabilize the talonavicular joint, as well as the apex of the arch of the foot. There are numerous other muscles in the below knee lower extremity but their involvement in passive supportive stance is minimal and for this reason and others, their function was not incorporated.

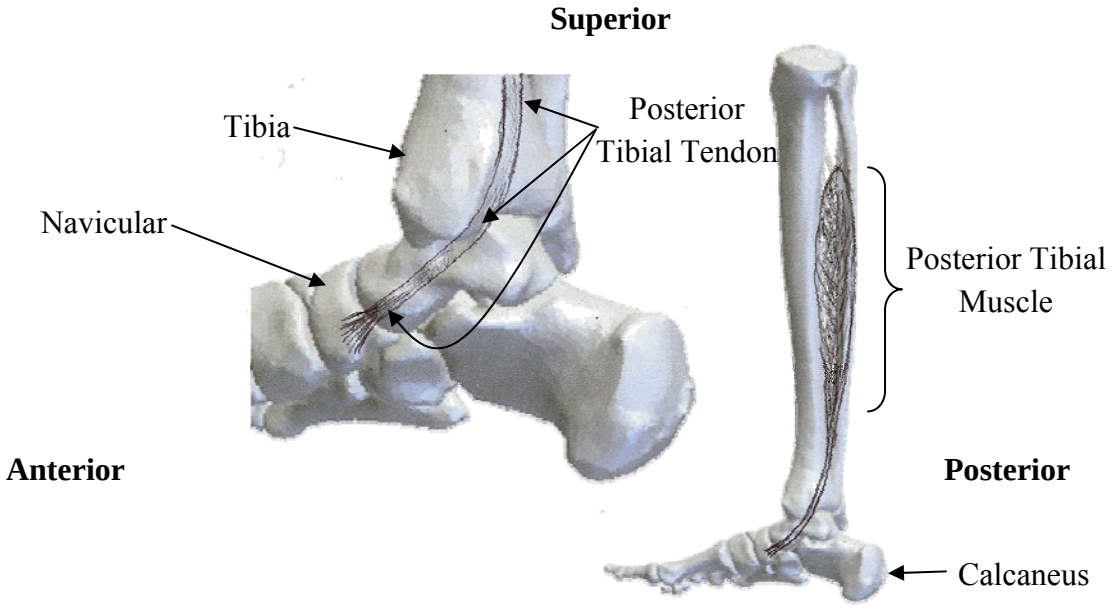

Figure 2.11: The Posterior Tibial Muscle & Tendon. The anatomy of the posterior tibial muscle and tendon. Path of the tendon to the navicular around the medial Malleolus and astride the talar body (restrained by retinaculum, not shown), left. Muscle body located posterior between the tibia and fibula in the deepest muscle level, right. Shape and placement represented from dissection, anatomy text[29,30], and literature[31-34]. Additional dissection images are provided (Appendix I).

Various biomechanical studies have been performed on aspects of the foot as a whole and with respect to individual tissues. Several of these studies have played key roles in this work by defining the presentation and behavior of tissues to be modeled.

2.3 Studies of the Intact Foot

It is well established that soft tissues do not display a purely linearly elastic response to loading. Their behavior is often simplified with the suggestion of a toe region and a linear region. In addition to knowing the stiffness of this linear region and estimating a behavior for the toe region, it is equally important to understand where (within the total elongation range of the ligament) the ligament behavior follows these representations. We see then, that not only are stiffness' dependent on material and structure, but any pre-tension or pre-slack in these structures can be variable as well. Soft tissue dampening behavior is also a feature of these tissues, but for the purposes of computationally modeling a semi-static state, its role is related to equilibrium time of the model (discussed later). The following studies explore this in an effort to understand how and when ligaments demonstrate their behavior.

Ankle Ligament Behavior

Siegler et al.[31] performed a study of 120 tensile tests on ligaments of 20 cadaveric ankles. The focus of the study was on collateral ankle ligaments and their mechanical characteristics. The average age (67.8 ± 15.2 years) weight (69.1 ± 15.1 kg) and height (1.71 ± 0.09 meters) of the population was recorded along with the results of mechanical tests on the lateral collateral ligaments: posterior fibulotalar (PFTL), fibulocalcaneal (FCL), and anterior fibulotalar (AFTL);

as well as on medial collateral ligaments: tibiocalacneal (TCL), tibiospring (TSL), posterior tibiotalar (PTTL), and the tibionavicular (TNL). These ligaments were dissected from surrounding anatomy and care was made to leave their full bony origins and insertions intact. These bony insertions were separated such that each ligament structure (even those sharing a bone of attachment) could be tested individually. Specimens were kept hydrated in a saline solution during testing. For testing a low elongation rate of 0.32 cm/min which corresponded to a strain range of 7.8%/min to 27%/min was specifically chosen to negate the effect of viscous behavior and capture elastic behavior. The specimens were preconditioned with 15 cycles then gradually cycled to higher load endpoints until failure. This was done to ensure the repeatability of the force-elongation curve and to obtain full sub-failure behavior. Extensive information was recorded during these tests including physical appearance and dimension, as well as a full spectrum of tensile properties such as ultimate load/elongation, yield stress/strain, and failure modes (ligament avulsions from bone vs. midsubstance tears). Along with this information was a stiffness constant of the linear region (Table 2.1).

Structure	Stiffness (N/mm)
posterior fibulotalar	164.3 ± 55.5
fibulocalcaneal	126.6 ± 42.9
anterior fibulotalar	141.8 ± 79.3
tibiospring	122.6 ± 66.9
posteror tibitalar	234.3 ± 77.6
tibionavicular	39.1 ± 16.6

Table 2.1: Reported Linear Stiffness Values. Stiffness and standard deviations reported for tested structures[31]. Early talocalcaneal ligament failure loads were <44.5N and thus this ligament was excluded from further study as it was deemed not a significant contributor.

A study by Nigg, et al.[35] documented the elongation and load behavior of intact cadaveric ligaments at different ankle positions. This study utilized three cadaveric ankles (age range 34-73 years). Ankles were dissected free of skin overlying the malleolar surfaces, the peroneal tendons, and surrounding retinaculum to give unrestricted visualization of the ankle ligaments. These ligaments were: lateral, the anterior talofibular ligament and calcaneofibular ligament; medial, the deltoid ligament. The mounting system for these ankles allowed full dorsi- and plantarflexion, internal and external tibial rotation, as well as inversion and eversion. Ligaments were kept moist by a phosphate buffered saline solution. Syringe needles were inserted into bones at the centroid of the insertions for ligaments to mark locations and ensure a repeatable measurement site on bone. Measurements were taken in a variety of 3D rotational combinations (36 in total). At each rotation the origin to insertion distance was measured. The study defined the shortest length found for a ligament as "anatomical zero distance" and the longest length as "maximum distance". The elongation was normalized between these *in situ* extremes. As with the previous study these ligaments were dissected free and a bone-ligament-bone specimen was prepared for each for mechanical testing. Each construct was elongated at a rate of 100mm/min until a load of 2N was reached. Loading was first removed, and then slowly reapplied to find the distance at which the ligament experienced 0.1N of load. The elongation of the ligament at this low load point was labeled "force-zero distance". This data identified the beginning of the toe region. The normalized elongation point of the toe region was compared to the normalized elongation of the ankle joint at the neutral position (Table 2.2). These values indicate that the anterior talofibular and deloid ligaments are either within or beyond the toe region with the ankle in the neutral position. The calcaneofibular ligament is indicated as being slack in this position. Note however the large standard deviations, especially in functional laxity.

Structure	Functional Laxity	Neutral Position
anterior talofibular	0.33 ± 0.27	0.47 ± 0.09
calcaneofibular	0.54 ± 0.27	0.46 ± 0.07
deltoid ligament	0.46 ± 0.12	0.57 ± 0.07

Table 2.2: Functional Laxity Values. Functional laxity (toe normalized elongation) and neutral position (also normalized elongation). With a sample size of n = 3 these values indicate whether a structure has not yet entered the toe region, or is in/beyond it[35].

Further *in situ* strain characterization was sought. A study performed by Butler et al.[36] investigated ligament properties from bone-ligament-bone constructs taken about the knee. Three knees from donors (range 21-30 years) of both sexes were studied. Dissection of the anterior and posterior cruciate, as well as the lateral collateral ligament was performed (as was the patellar tendon). These dissections were done under magnification to preserve fiber bundles and cleanly separate them from surrounding tissue to leave all but their origins and insertions intact. These specimens were potted at their bony ends, and placed in a warmed, saline buffered testing bath. The specimens were then failure tested, with no mentioned preconditioning, at 100% strain/second. Various data was analyzed from these tests, of note were a stress/strain curve of the specimens and the yield strain.

From the data in Butler et al. as well as earlier data from Danylchuk et al., a study by Blankevoort et al.[37] expanded on the analysis and identified a non-linear toe region and a linear, post toe, response of these knee ligaments. In their study, which was a mathematical model of articular knee contact, they derived a two phase behavior for their ligaments. A non-linear equation to establish ligament tension based on strain in the toe region, and a linear relationship upon leaving the toe region. By referring back to previous experimental study[38], Blankevoort et al. was able to match internal and external rotations between the mathematical model and

experimental findings by adjusting the initial ligament strain values. For those knee ligaments, the linear region *in situ* pre-strain was determined by this method and listed as follows (Table 2.3). The posterior cruciate ligament as well as portions of the lateral collateral ligament were found to be slack and are not listed below [their initial strain range (-0.04 to -0.25)].

Ligament	Linear Region Initial Strain
Anterior Cruciate	
anterior bundle	0.06
posterior bundle	0.1
Lateral Collateral Ligament	
lateral bundle	0.08
Medial Collateral Ligament	
anterior bundle	0.04
intermediate bundle	0.04
posterior bundle	0.03

Table 2.3: Initial Ligament Strains. Strain values for knee ligaments in tension. Values shown all indicate a stretch in ligaments just leaving the toe region[37].

Li et al.[39] considered similar behavior as part of a 3D MR driven knee model. The three phase scheme developed by Blankevoort et al.[37] (slack, toe, linear regions) was used here. Further classification of the transfer from toe into linear region was made by defining the end of the toe region to be 0.06 or 6% strain. Here again the selection of initial strain lengths was done by matching model behavior to experimental.

Song et al.[40] followed these works by summarizing them with "Typical residual strains are approximately 3-5% in the ligament of diarthrodial joints (Blankevoort et al., 1991; Li et al., 1999)." The study then proceeded to model neutral knee ligaments under an initial 3% *in situ* strain.

Following a separate line of research on a different joint, Savelberg et al.[41] performed a study on the wrist ligaments. This study's purpose was to determine strains and forces in carpal

ligaments during various flexion and deviation movements. Seven specimens were used for this study from a population of age range 63-78 years. The joints were inspected for normalcy prior to testing. Easily accessible ligaments including the palmar radiocapitate, palmar radiolunate, dorsal radiotriquetrum, and dorsal triquetrotrapezium ligaments were studied here. Radioopaque beads were attached along the lengths of these ligaments from origin to insertion. During manual movement of the specimens, several radiographs were taken to measure the 3D position of the beads at each angle. Bone-ligament-bone specimens were then isolated and tested to determine both zero-force length and the force-elongation relationship of the ligament. The *in situ* strains of these ligaments were reported for all positions. For neutral position, the strains varied between approximately: -2% to 11% strain for the dorsal radiotriquetrum ligament, -4% to -12% for the palmar radiocapitate ligament, 5% to 6% for the palmar radiolunate ligament, and -3% to 10% for the dorsal triquetrotrapezium ligament[41].

Perfect representation of the ankle ligaments would require studying each of them in turn across a large population of specimens. In the absence of this, the data presented from studies of the knee ligaments suggest that the linear region starts at approximately 3-5% *in situ* strain[36-39]. The study of both the knee and the wrist suggest that many of the ligament structures present in either joint exist with a neutral pre-strain at or above that level[36-41]. The study of the ankle suggested that most (two out of three) of the ligament structures studies are in or beyond the toe region and thus also under some pre-strain[35].

Without a full datasheet of ankle ligament behavior available, and for simplicity in agreement with literature, the range of approximately 2% to 6% *in situ* pre-strain was considered when formulating the models presented in this work.

Plantar Fascia Behavior

The plantar fascia, the major ligament structure of the sole of the foot, was studied in detail by Kitaoka et al.[42] In their study 12 cadaver feet with an average age of 75 years (range 56-81 years) were prepared for mechanical testing with extensive dissection of the foot. The origins and insertions of the plantar fascia were separated from the remainder of the foot by disarticulating the hindfoot at the transverse tarsal joint, and separating the forefoot with osteotomies of the metatarsal bases. The bony portions of the specimen were affixed to a materials testing system, and visual markers were applied to the tissue. These markers were placed in the medial, central and lateral portions of the fascia. A variety of loading rates (11.1, 111.2, 1112.0 N/sec) were used to axially load the specimen to 445N of tension. With slight variation the stiffness of each zone was unchanged due to loading rate, further, no significant difference in zonal stiffness was found. The concluded average stiffness of the intact fascia was 203.7 ± 50.5 N/mm.

Interosseous Ligament Behavior

The interosseous membrane between the tibia and fibula has not, from a search of the literature, been experimentally tested to yield stiffness characteristics. Such a study has however been performed on the forearm interosseous membrane. Pfaeffle et al.[43] dissected 18 fresh frozen cadavers (45-70 years old) to obtain forearms. The forearm membrane further dissected to yield the "central band", a distinct band of interosseous ligament approximately 3-5mm in width. These band it its attached bone segments were mechanically tested in an axial load frame. Specimens were preloaded to 0.5N then loaded to failure at 30mm/min to obtain a load elongation curve. The linear region stiffness of these specimens was calculated at 13.1 ± 3.0 N/mm per millimeter of specimen width[43].

Goals

Appreciating the final successes and limitations of the previous ankle simulator and with perspective on how to formulate a full foot model, a plan for the simulation presented here is formed. The development of this forward kinematic approach, which uses patient specific geometry and constrains joint motion by anatomy and soft tissue behavior, was created around the following criteria. These goals are,

1) Development of a simulation method for investigation of the entire foot and ankle
2) Determination of the means to rapidly generate such a model
3) Improvement of these means to further reduce the potential for user error
4) To validate the model in comparison to clinical and experimental findings
5) Demonstrate the capability to model a variety of orthopaedic injuries and treatments

Chapter 3 - Methods

The final technique presented here for creating a 3D anatomical model of the foot and leg represents the development of methods to capture, process and transfer geometry from scan data to motion simulation. The motion simulation model evolved through multiple iterations which were explored for days, weeks, and months at a time. At each model iteration, significant changes were made that reflected an increasing awareness in modeling efficiently using the various software programs to develop and run these simulations. The initial conceptualization of much of this work includes extensive educated trial and error to create stable simulations. In the course of this work there were forays into related areas of research (significant ones are documented in the appendices). While presenting the successful stages of these models in a purely chronologically manner would be the simplest, attempts have been made to consolidate the progression of the model for the readers ease in following salient improvements at major steps. Major sources of error or model failure are identified and presented with the solution devised to count them. The "initial models", which are presented first, were used as proof of concept and to obtain realistic behavior and model stability. The "final refinements" methodology incorporates all of the refinements, learned from both the end product of initial models and adjustments to latter ones, which allow for the rapid simulation of model states with much improved stability. These final refinements improved various aspects of model response and stability to bring the resultant behavior closer to that of live tissue, these are discussed.

3.1 Initial Models: Scan Geometry

The previous model developed by Peter Liacouras[44] was built from CT scan data from the National Library of Medicine's Visible Human Project. The male CT dataset was performed with 1mm x 0.33mm x 0.33mm scan resolution[45]. This was unfortunate as it lead to a dimensional non-uniformity when brought into 3D scan space, which results in rectangular voxels that have a lower axial scan resolution. [**NOTE**: Voxels are the 3D version of pixels, the digitized 2D resolution of a scan. When these 2D pixel views are layered and computed into 3D the axial scan resolution gives these pixels their 3D dimension, converting them to voxels.] Further, the scan data contains some registration errors whereby the tibia and fibula approximately 2 inches above the ankle are translated away from the rest of the leg (Figure 3.1). Lastly, the foot was positioned in a moderately plantarflexed position and the forefoot was curled in on itself slightly.

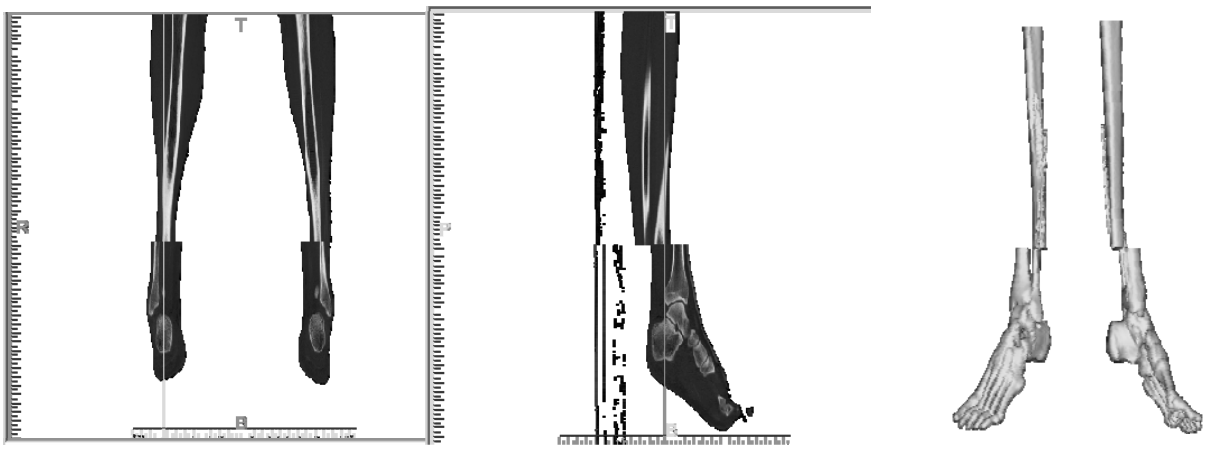

Figure 3.1: NLM-VHP Male Dataset. Digital images and 3D reconstructions of the male dataset. The AP view of the male dataset, left, note the drawn appearance of the proximal tibia and fibula, the discontinuity above the ankle joint, and the inverted ankle joint. The lateral view of the same scan, middle, also showing the scan discontinuity as well as excessive plantarflexion

of the ankle. Rapid, low quality 3D rendering of this anatomy further shows the error associated with bony capture from this scan data, right images.

In an effort to avoid some of the problems associated with manually resizing, aligning multiple bones and repositioning the ankle and toes, the female dataset was considered. The female CT data was taken at 0.33mm axial resolution[45] to yield cubic voxels which solved the proportions problem and improved axial resolution. The female dataset also suffered from similar mis-matching of scan data, but in this scan the mismatch was higher in the leg, just below the tibial plateau. Again the foot was plantar flexed, but to a lesser degree and with lesser curling of the toes (Figure 3.2). Formulation of the early models proceeded with this dataset.

Figure 3.2: NLM-VHP Female Dataset. Improvements over the male data set both in resolution, distortion and position of the foot. There is still some plantarflexion and inversion in this dataset, but forefoot position is better and more of the tibia is available.

3.2 Initial Models: Scan Processing

To view and ultimately capture anatomy from the scan data, the program MIMICS (Materialise's Interactive Medical Imaging Control System, Materialise, Ann Arbor MI) was

used. MIMICS is a fairly complex program which incorporates various thresholding, geometry recognition, pixel mapping and boundary algorithms to allow the user to isolate various shapes (especially organic) in 3D space from sources such as computed tomography or magnetic resonance imaging. Importing the NLM-VHP female CT dataset was done manually. The dataset for the entire body was available in quarters from superior to inferior and taken in the transverse plane. Manual importing allowed for the isolation of slices only pertaining to the below knee lower extremity. Manual isolation of the region of interest created a smaller virtual workspace which was easier to navigate and saved computation time throughout MIMICS processing. The CT scans are a grayscale field, which can be navigated in a user assigned orientation of top/bottom, left/right and front/back. Upon importing the scan field, MIMICS prompts the user to orient the model to these directions. [**NOTE**: while MIMICS allows you to assign this orientation to your dataset, there are no translational or rotational positioning functions to allow you to align the model in any way – thus scan orientation becomes somewhat important.] Once directions are assigned, the default MIMICS workspace appears and MIMICS compiles 2D views for all orientations (Figure 3.3).

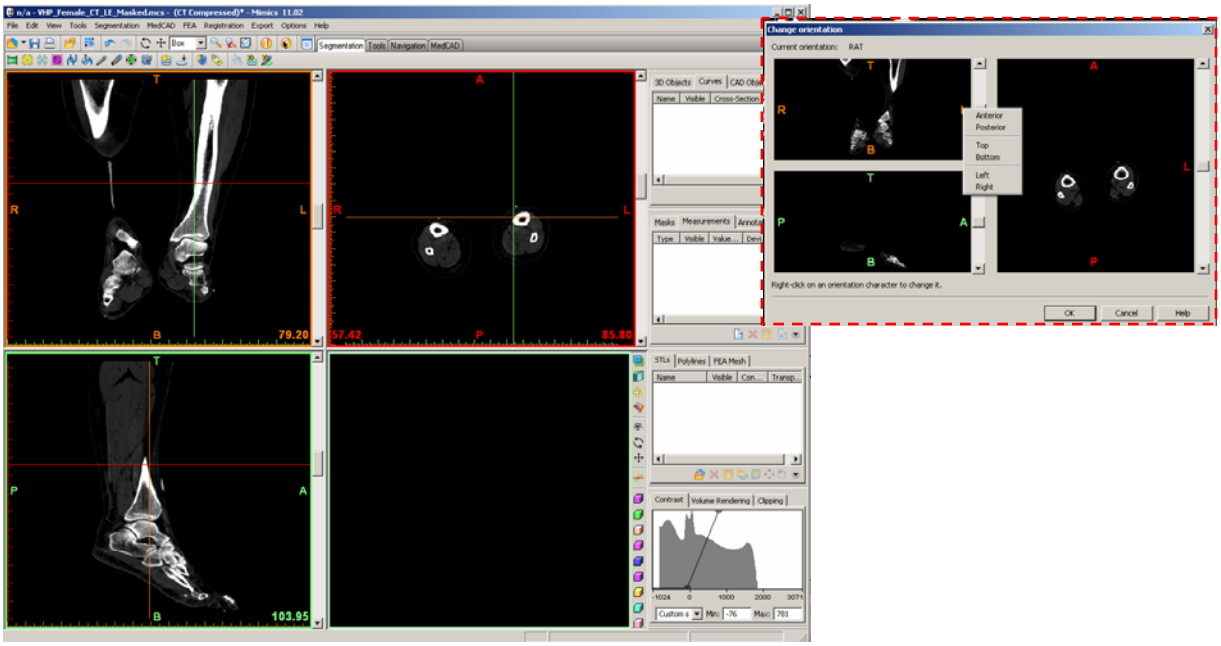

Figure 3.3: MIMICS Workspace. Basic 4 pane workspace for processing scan data in MIMICS. Upper right and left, and lower left panes are 2D views, lower right is reserved for 3D objects. Stacked windows, far right, display various measurements, masks, threshold histogram, and 3D objects. Prompt window for orientation of the scan allows orientation to be viewed and altered in any 2D view preview of the workspace (right callout).

Step 1, Threshold

The first step was to isolate cortical bone in the scan. The profile line tool allowed the user to drag a line across a portion of the scan. Typically a bicortical bone region was so lined to provide intensities for air, soft tissue, cortical bone, cancellous, then back through cortical and soft tissue – giving a thorough spread of tissue. The grayscale intensity histogram across the length of the line was displayed, with the brighter cortical bone appearing as peaks in the background soft tissue and noise (Figure 3.4). These tools allow the user to select upper and lower limits to threshold the entire dataset to select tissues of their choosing. Cortical bone

shells were of interest for this scan. The threshold tools often yielded clear bone edges and separated large bones from one another at their joints.

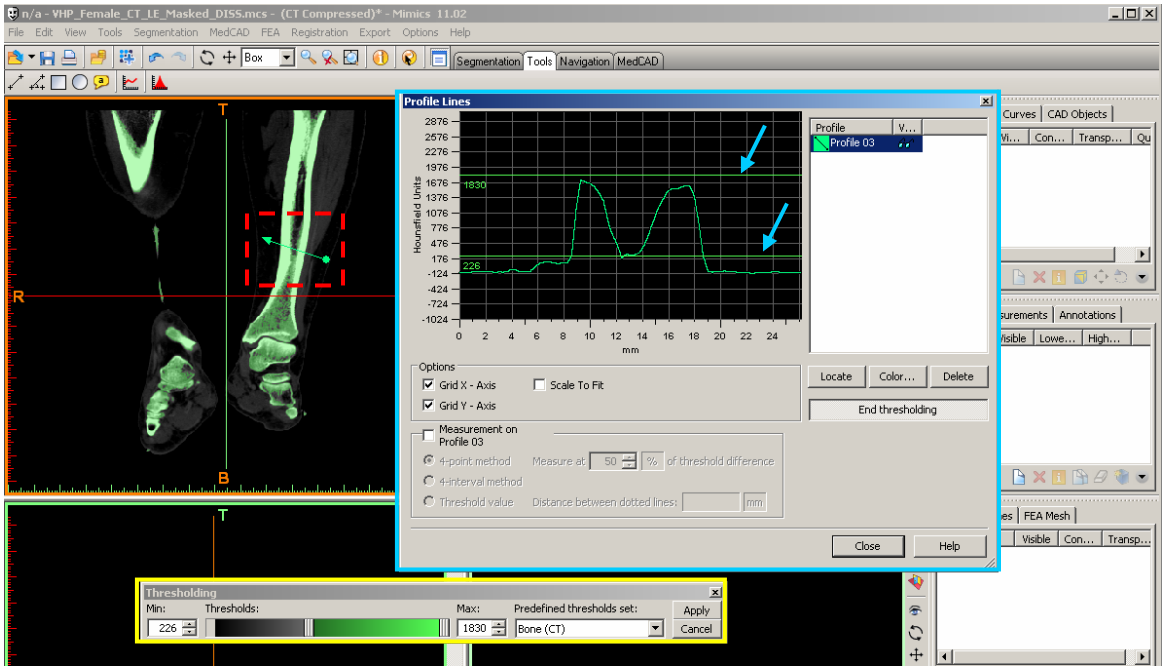

Figure 3.4: Threshold Windows. Workspace pane, in rear, showing the AP 2D view with a green profile line sketched across the cross section of the leg (red dashed box). Plot of scan intensity across the length of the profile line (boxed in blue, center foreground). This chart allows the user to adjust threshold levels (blue arrows) while viewing relation to scan data. Separate threshold box allows additional control with or without profile lines being used (boxed in yellow, lower foreground). [**NOTE**: Cartilage is not captured/seen from this CT scan technique.]

There were some problem areas when using this technique. Small bones or certain areas of larger ones (such as cancellous articular ends) which have thinner or less dense cortical bone can, from a thresholding perspective, merge into the bone they articulate with. By varying the threshold to one end of the spectrum (brightest pixels), *only* cortical bone can be isolated; but in

doing this much of the articular ends of large bones and very large regions of the smaller bones of the foot are not captured (Figure 3.5).

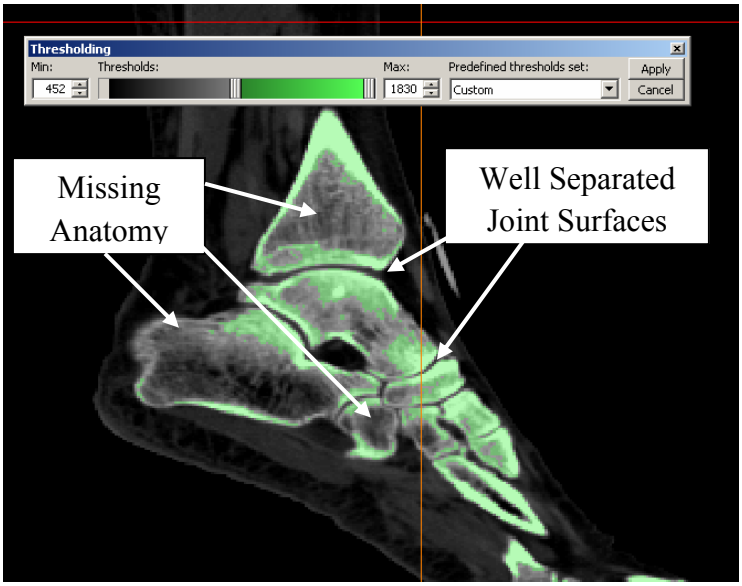

Figure 3.5: Threshold Effect with Large and Small Bones. Threshold applied to foot, shown here in the medial view. The foot contains both small bones and bones that experience a great deal of load in daily activity, there are numerous areas where dense cortical bones quickly yields to porous cancellous. Selecting a single threshold value to isolate joints *and* preserve bony anatomy is problematic in the foot.

By varying the lower threshold limit to the opposite end of the spectrum (dimmer pixels) most of the articular surfaces are captured, but they merge almost seamlessly with one another – so much so that manually separating them would entail unacceptable error (Figure 3.6).

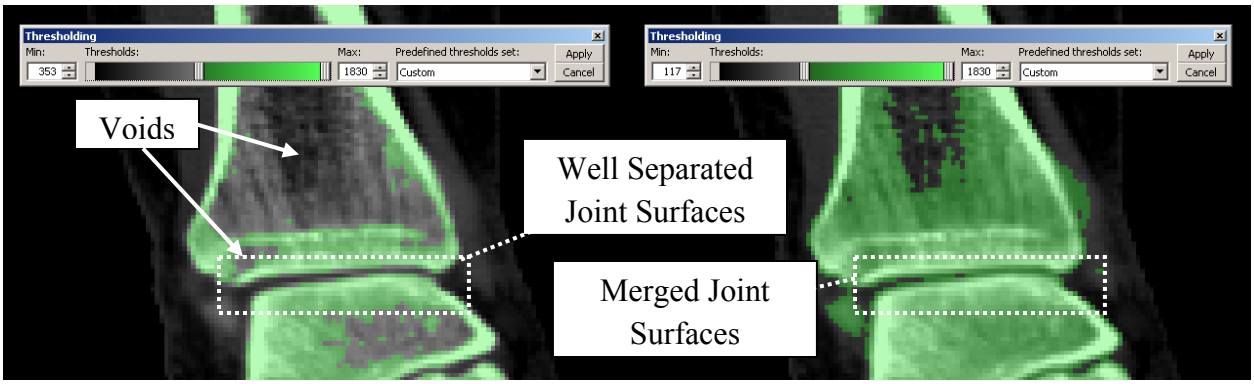

Figure 3.6: Threshold Effect at the TibioTalar Joint. Different threshold values applied to the foot, shown in the medial view. More manual filling of voids is required in bone as epiphyseal data was lost with a narrower threshold. However, more manual separation joints was also required with broader a threshold.

Additionally, the dimmer threshold may capture portions of ligament and tendon entheses or slightly calcified soft tissues which render the diaphysis with a much rougher surface, and further occlude the epiphysis. A middle ground must be chosen which defines most of the epiphyseal surfaces while separating them enough for accurate manual partition. When choosing a middle ground for threshold several bony sites should be considered. [**NOTE**: multiple thresholds can be done in isolation to parse large bones and small bones. This requires additional work to add up the discrete scan thresholds to obtain complete bones. For these scans and this region of the body, this method was briefly explored but was not found to save time or simplify further capture.]

The highlighted 3D overlay of the grayscale intensity is called a "mask" in MIMICS. This mask can be viewed in each of the 2D perspectives overlaid on the pixel background of the scan, but exists in the 3D volumetric pixel, or voxel, scan space. Post-threshold, much of these further stages are functions performed on the initial mask. While the scan itself is referenced for

refinement of joint surfaces and for accuracy checks, the accuracy of the initial mask is very important for final model realism, as well as reducing manual manipulation time.

Step 2, Region Growing

The first (primary) mask captures the cortical bone of the entire extremity segment. The "region growing" tool will isolate bones from each other and any artifacts in the scan space (hardware, or anything radio opaque enough to threshold with the bone). The tool creates a new mask by selecting portions of the first mask that are connected by a voxel side in 3D space, essentially growing a new region out of connected mask portions. For large bones this was straightforward and separation is automatic, for small bones there may (and will) be voxels connecting articular surfaces (Figure 3.7).

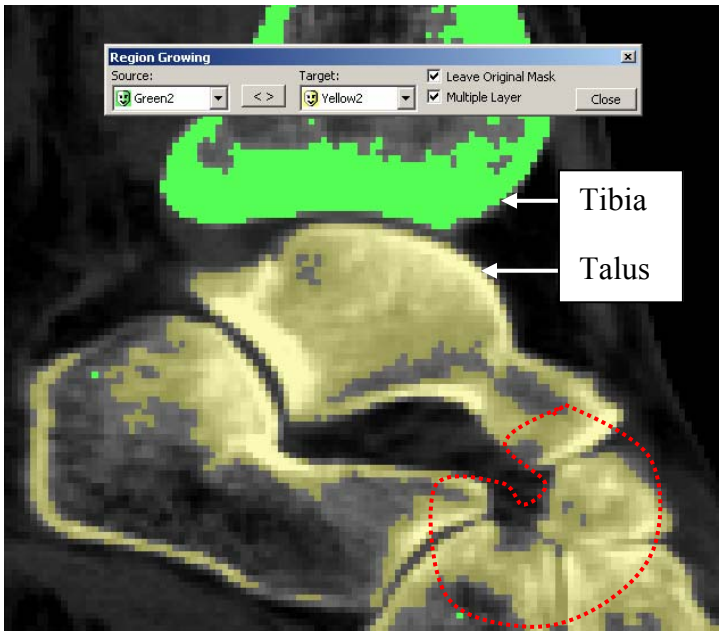

Figure 3.7: Region Growing. Separation of large bones readily done as seen with the tibia (green mask) and talus (yellow mask). Even with good threshold choice, connecting voxels will cause region growing to extend to more than one bone (red dotted region shows several instances of joints merging in the mask. Note the clear division of subtalar joint surfaces.

To separate smaller bones for region growing, manual deletion of connecting voxels was necessary. At least two of the three 2D perspectives were checked by necessity, frame by frame, for any connectivity. If a connecting voxel was found it was erased from the first mask. [**NOTE**: It is useful to try region growing early, this can illuminate where such connecting voxels are before extra time is spent editing needlessly.] Forming the primary mask, and then separating it at articular ends followed by region growing yield a set of secondary masks, one for each bone.

NOTE: It is approximately at this stage that this method begins to differ from the previous capture method. The previous method used features of MIMICS to create profile curves for the bones which were then exported as .iges files. The implications of this branching will be discussed further in the SolidWorks section of the methods. For more information on the previous method refer to Liacouras, 2006[44]

Step 3, Surface Closure

The secondary masks are separated bones but with varying porosity. As mentioned in the thresholding section, a middle ground was found between articular detail and articular blurring. Thus the secondary masks are populated with voids located in the center of long bones and at epiphyseal ends (Figure 3.8). These voids breach the external surface of the secondary masks and must be filled. If proper thresholding is selected earlier then sealing these surfaces can be done rapidly with little error. [**NOTE**: Even in the presence of the original scan and MIMICS tools the precise determination of sub millimeter shape from one pixel to the next may be left to user judgment and exhibits digitization error based on both user factors and scan resolution.]

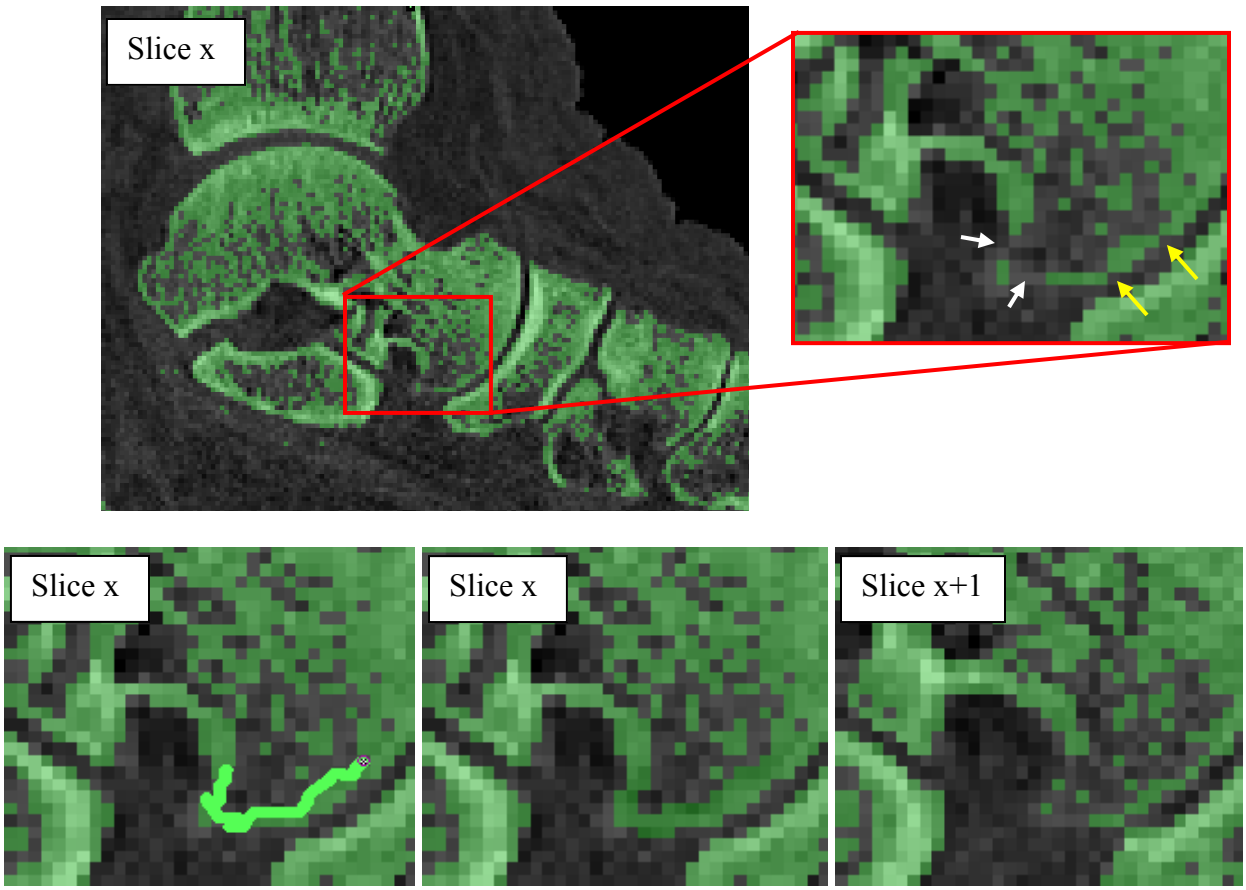

Figure 3.8: Surface Breaching Voids. Example image of the primary mask of the leg in the lateral view of the talus (upper left). Surface voids (white arrow, callout) require manual closure through all slices to seal the external surface of the bone before the filling step is performed. The bony borders from the underlying scan assists in the manual determination of where these edges lie. The "edit masks" tool is employed here, and can be scaled in size to one pixel if necessary, example shown with a 2 pixel wide circular edit to fill voids (bottom left). Diagonally connected pixels are also addressed while using the mask edit as they likely yield voids in other 2D views (yellow arrows, callout). After editing the mask appears for inspection to determine if surface is sufficiently sealed (bottom middle). This step is repeated for each scan layer as changing cross section anatomy prohibits propagation of the mask edit to multiple slices (bottom right).

NOTE: Formation of secondary masks can be done before or after surface closure. For large bones with separated articular limits, closure is secondary to region growing to form secondary masks. For smaller bones with extensive articular merging, closure of the surface may be incidental during the editing to separate bones. In essence it may be more efficient to perform these functions in different orders depending on bone size, scan/bone quality.

Step 4, Mask Filling

Once a secondary mask has been completely sealed, the internal voids may be filled. The "cavity fill" tool in MIMICS works the same way as the region growing tool but with un-masked scan areas. [**NOTE**: If a mask has not been fully sealed, the entire workspace will "fill" when the fill tool spills out of a missed breach.] Due to the porous nature of trabecular bone, the voids will not always be connected, and there may be many more voids than just one large and clearly defined hole. In fact, it is almost always the case that there will be numerous one to three voxel "holes" in the masks after sealing and filling (refer back to Figure 3.8). These holes are problematic later on when 3D solids are rendered from the masks. At that stage, the holes create additional internal geometric complexity which ultimately translates to greater computation time and may limit the resolution of the final 3D solid by splitting software resources between useful external detail and useless (for these purposes) internal architecture. MIMICS contains features specifically designed for situations such as this. The "open" and "close" features perform a sequence of "dilate" and "erode" sub-features. The sub-features either at a void/mask interface remove a set number of pixels (erode), or add a set number of pixels (dilate). The mechanism for the subtraction or addition can be performed under a variety of connectivity settings which essentially let the user choose if the operations are performed for edge only connectivity or edge and vertex connectivity. "Open" is erosion followed by dilation, "close" is a dilation followed

by erosion. For the purposes of mask filling, the close feature was used. The 2D edge only closure was used for the secondary masks set at a depth of 1 pixel. This was the least aggressive closure yet was completely effective for these masks. The dilate step closed any imbedded voxel holes as well as expanded the surface of the bone by 1 pixel. When the erode subroutine was performed, the surface shrank by 1 pixel, and the inner holes, which were now filled and thus had no void/voxel boundary, were unaffected (Figure 3.9). The net result to the surface was a smoothing where small pits were filled. By restricting the close feature to 1 pixel, the changes in the surface geometry were minute and did not alter articular surface shape.

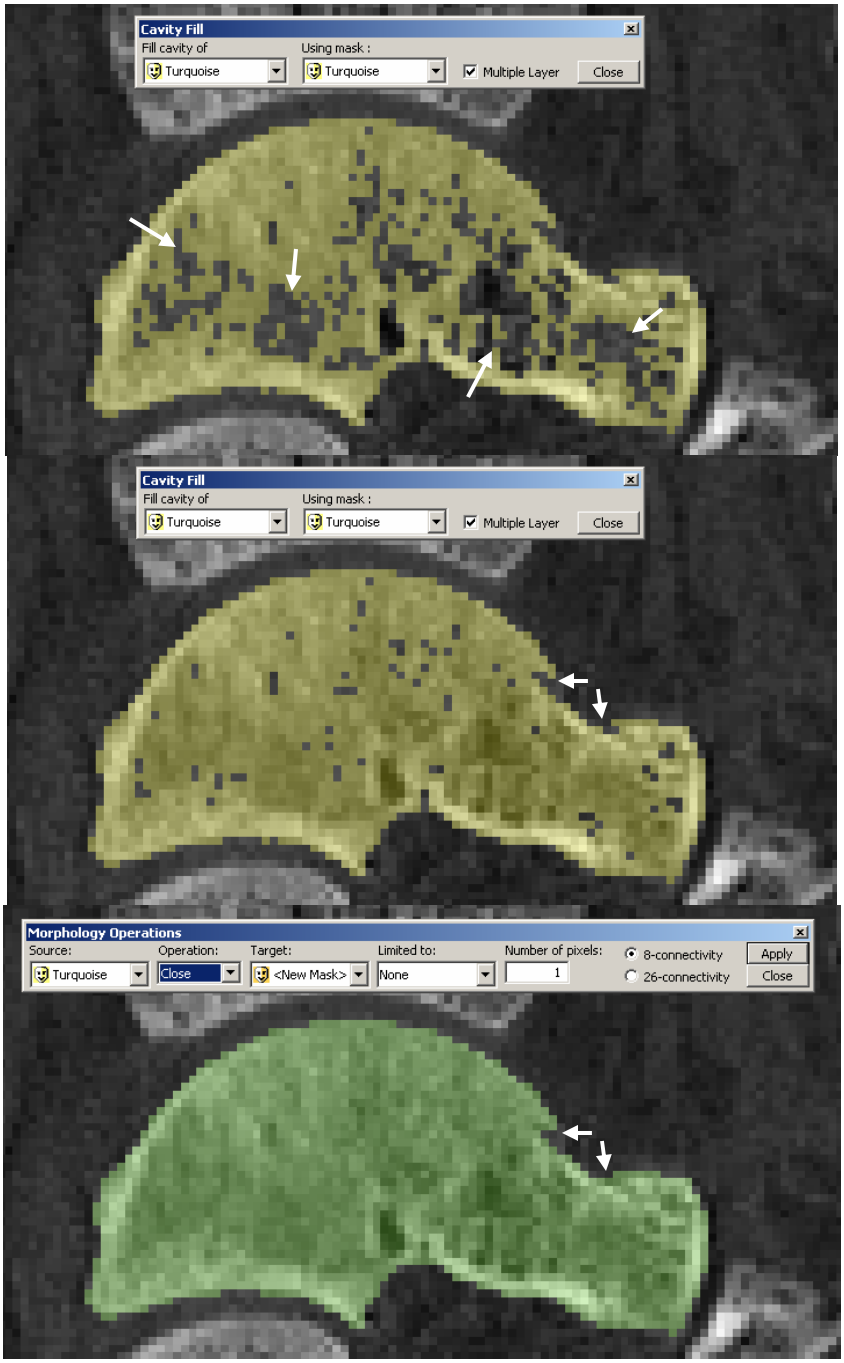

Figure 3.9: Cavity Fill and Close Feature. Final processing to yield complete masks. The surface closed mask contained large voids (arrows, top) filled by the "fill cavity" feature (middle). Remaining voxel voids closed with "close" morphology operation. Note external surface change at very small features (arrows, middle and bottom image).

Step 5, 3D Preview

There is a 3D object rendering preview in MIMICS which builds an object from a mask. This feature has very basic crude/medium/fine build options. The feature is useful for rapidly building all the secondary bone masks and viewing them in 3D space. This can draw attention to any large errors from the capture methods that were missed or unrecognized in the 2D views of the mask (Figure 3.10).

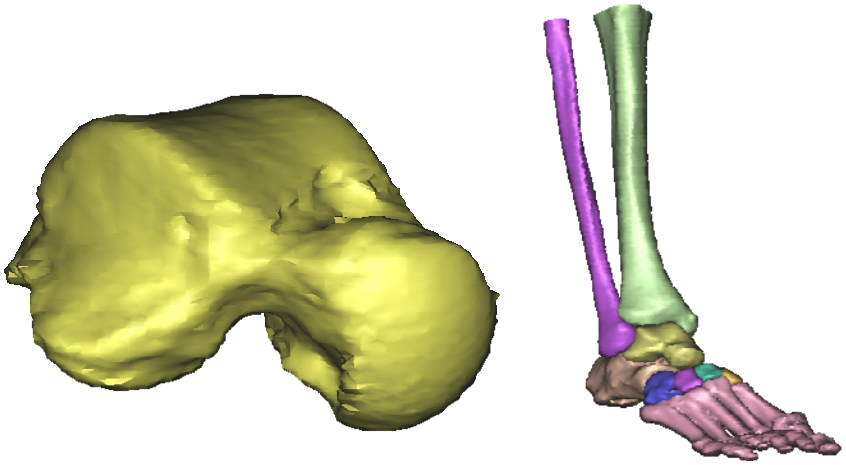

Figure 3.10: 3D Preview of Geometry. A high resolution preview of the talus in an oblique view shows surface contour and detail which distinguishes articular surfaces. Additionally these surfaces are free of any large apparent artifact from processing (left). Entire foot rendered in this manner with bones isolated (forefoot not yet separated). No gross defects in the mask processing are seen in these images (right).

Step 6, 3D Rendering

MIMICS can render exportable geometry from either mask or 3D objects by using the STL+ module. The masks were used as the template for this rendering to reduce compounded smoothing error from using the 3D objects (potential for "hidden" smoothing on top of smoothing). These bone masks were rendered into stereolithographic file format for exporting.

The .stl format is a standard 3D mesh used in various manufacturing venues. The mesh is a surface defined by triangles. There are numerous options for rendering the output .stl from the mask (Figure 3.11).

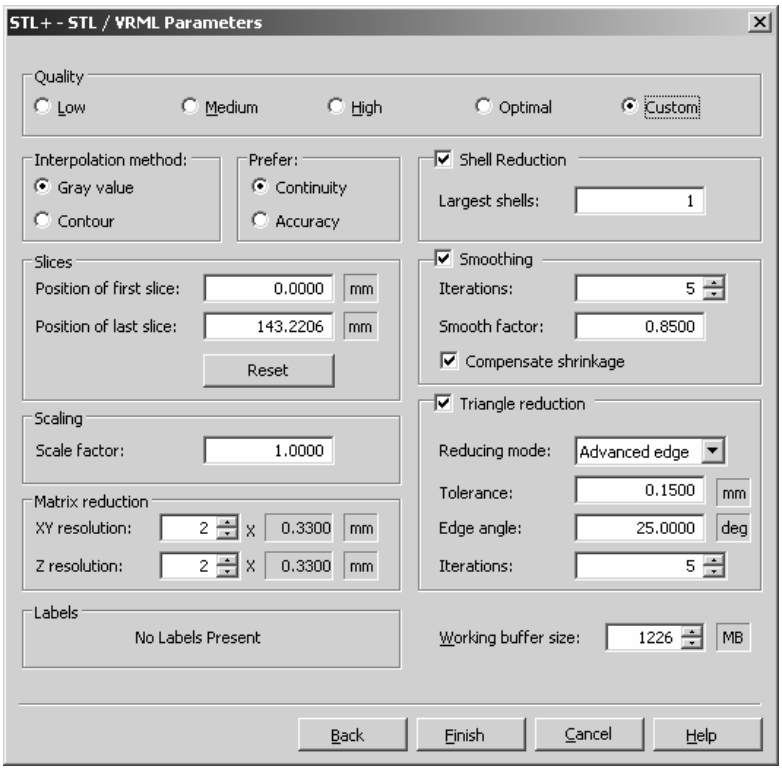

Figure 3.11: STL+ Option Window. The options include preset quality templates, as well as a custom option. Additional factors such as scaling, matrix reduction, smoothing, and triangle reduction allow for further choice in created the .stl mesh file.

The majority of these options pertain to simplification features such as smoothing and triangle reduction. There are software constrains such as memory allocation that may (and here did) limit the final complexity of the .stl files when opening them in another program. As the tibia and fibula were so vastly larger than any of the bones of the foot (the unreduced tibia contained 29,000+ triangulated surfaces, an order of magnitude above the cuboid which contained 3,700+ number of triangulated surfaces (Figure 3.12), two sets of parameters were

created to scale the simplification features to bone size. A separate scheme was developed for the long bones and a second scheme for the smaller bones of the foot (Table 3.1, Table 3.2).

The interpolation method is an expanded 2D to 3D interpolation of images. It was chosen over grey value interpolation initially over concerns about axial slice distance (which cause poor grey value rendering) and later kept with the cubic voxel masks as little to no difference was seen between methods. Smoothing is a filter for noise reduction of the rough surfaces. The smoothing factor used was 0.5, midway between the minimum (0) and maximum (1) values assign importance to determine how much smoothing to apply based on local geometry. Smoothing of the surface reduces roughened geometry. This smoothing may lead to a loss in total part volume. The "compensate for shrinkage" selection maintains object volume if smoothing reduces it appreciably. Triangle reduction reduces file size (vital for large high resolution bones) by considering two kinds of values: tolerance, which is how far out of plane two nearby triangles may be in millimeters (suggested to be ½ or ¼ pixel size, thus 0.15mm was chosen); and edge angle, which considers if two triangles are near the same plane using degrees. By considering both the distance and degree of deviation between two or more triangles, the reducer may find several that, under these parameters, several triangles lie in the same plane. If this is the case, then the plane is remeshed with fewer triangles. [**NOTE**: The use of the smoothing and reduction feature was initially determined and modified as other scans were processed to achieve a user selected middle ground between highest resolution of final geometry and reasonable model processing times. These parameters can be improved by increased processing power which affects all stages of modeling and simulation.]

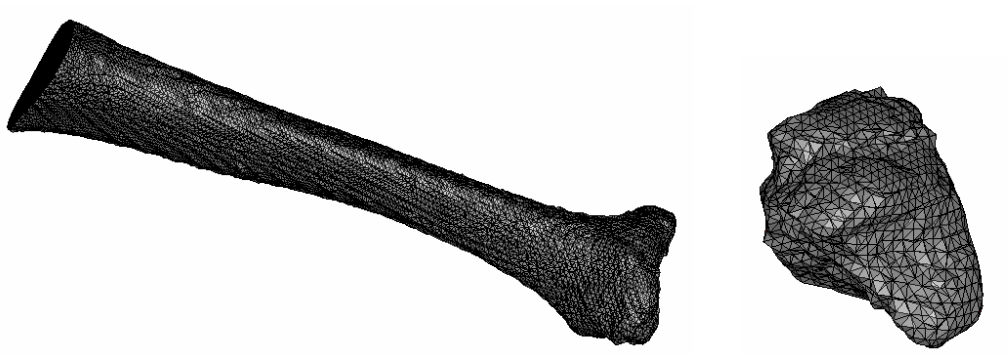

Figure 3.12: Raw .stl Mesh of Tibia and Cuboid. The tibia (29,000+ surfaces) with no triangle reduction or smoothing applied, left. Cuboid (3,700+ surfaces), also with no reduction or smoothing, coarse surface appearance is very visible here, right.

Long Bones (Tibia, Fibula, Metatarsals, Phalanges)	
Custom Parameter	Value
Interpolation Method:	Contour
Prefer:	Accuracy
Shell Reduction:	1 Shell
Smoothing:	5 Iterations 0.5 Smoothing Factor Compensate Shrinkage (yes)
Triangle Reduction:	Reduction Mode: Advanced Edge Default (0.15mm) Tolerance 15 Degree Edge Angle 10 Iterations

Table 3.1: Long Bone Rendering Parameters. Scheme performed on the long bones and, in early models, on the rays. Reduction choices were chosen to have greatest effect on simplifying the diaphysis and retaining detail at the epiphysis (limited reduction angle).

Small Bones (Calcaneus, Talus, Cuboid, Navicular, Cuneiforms)	
Custom Parameter	Value
Interpolation Method:	Contour
Prefer:	Accuracy
Shell Reduction:	1 Shell
Smoothing:	5 Iterations 0.5 Smoothing Factor Compensate Shrinkage (yes)
Triangle Reduction:	None

Table 3.2: Small Bone Rendering Parameters. Scheme performed on the small bones of the early model. Reduction was not performed due to small default mesh size of these bones. Smoothing eliminated .stl mesh surface roughness.

An add-on feature in MIMICS allows the user to open the .stl files in a remesher to perform further smoothing, reduction, or a host of other features to edit the mesh at a fine level (manipulation of individual triangles, triangulated regions, and several other powerful mesh manipulation tools). [**NOTE**: while future work in these models may benefit from performing bony manipulation at the remesher level, SolidWorks remains the more powerful tool in this domain.] Through this remesher, the large and small bones schemes were initially designed (Figure 3.12 images are from the remesher). The amount and extent of triangle reduction and smoothing were manually, iteratively adjusted to achieve a high degree of file reduction while maintaining articular contact surface detail for identifying prominences for soft tissue attachment (Figure 3.13).

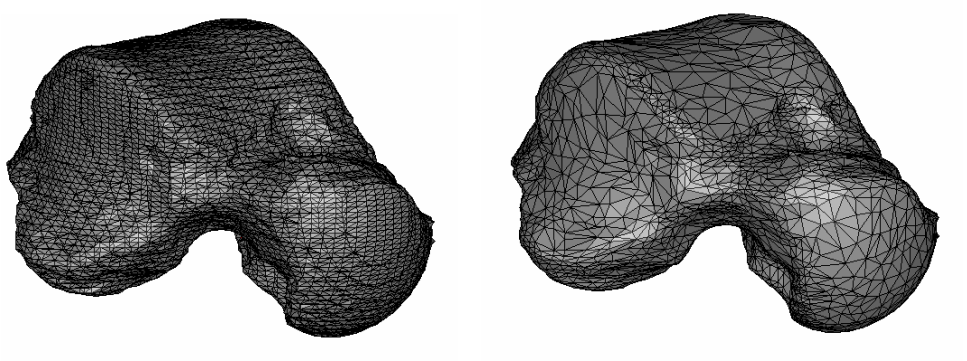

Figure 3.13: Mesh Reduction and Smoothing Effects. Several reduction and smoothing schemes were explored in the MIMICS remesher module. Examples are shown here of applying the two reduction and smoothing schemes to the talus (small bone, left; long bone, right). Later models incorporated triangle reduction used early just for long bones. Geometry was deemed unaffected as surfaces and volume were preserved.

3.3 Initial Models: SolidWorks Assembly

The exported .stl files from MIMICS were imported to SolidWorks (SolidWorks Corporation, Concord MA) manually. SolidWorks recognized .stl files and gave several options for opening these files and converting them. These options are solid body, surface, and graphics. [**NOTE**: If the mesh is completely sealed and does not contain extensive internal voids/surfaces, the solid body load can be used without difficulty – else it will fail with a warning to use a graphics or surface open. A separate warning is given if the file size is too large (too many triangulated surfaces) which varies depending on factors such as memory allocation.] SolidWorks loaded each mesh and converted it automatically into a solid body. This body was directly saved as a part file in SolidWorks file format. All the bones were opened and saved in this manner. After conversion, a new assembly was created and each bone was loaded in as a new part. The origins of each new part were carried over from the scan coordinate system and

thus allowed registration of the bones in their scan orientation. This was accomplished by using SolidWorks mate feature, and selecting "for positioning only" to move the part into position without adding constrains at this stage (Figure 3.14).

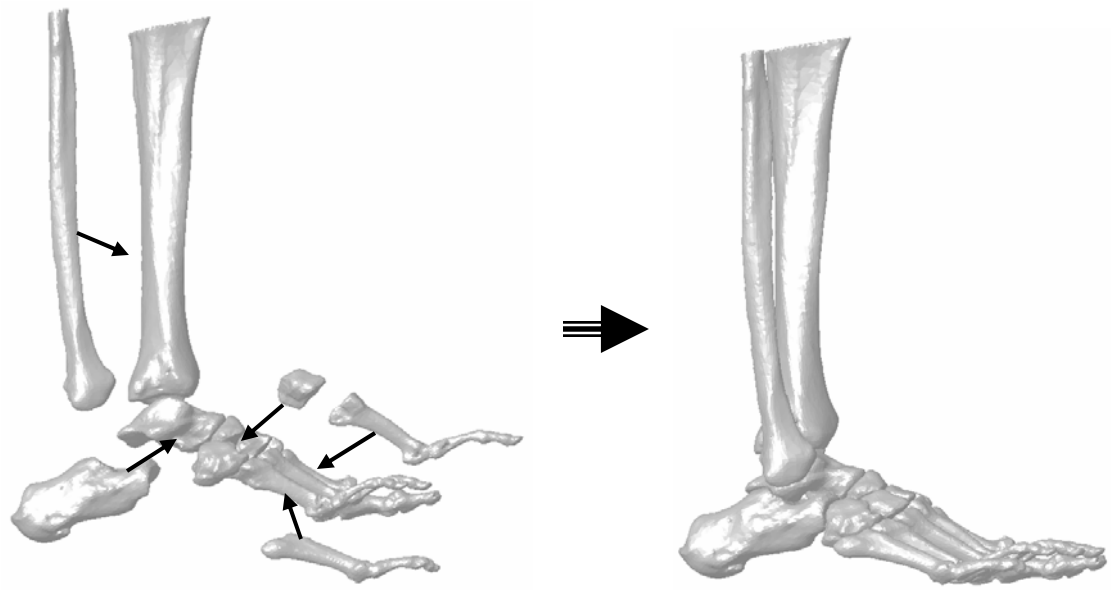

Figure 3.14: Assembly of Bones into Foot and Leg. Individual bone part files and final assembly. The bones were brought into an assembly and their origins were mated which maintained their scan orientation. [**NOTE**: As mentioned previously, the female dataset from the NLM-VHP was in slight plantarflexion. To move the tibia and fibula into an anatomical neutral, they were first rigidly mated with one another and the assembly of leg bones was rotated in the sagittal plane about the ankle to a vertical position and translated into place based on anatomical text reference.]

To ensure good articular coverage, the "Move Component" feature, a tool in SolidWorks' arsenal "interference detection", was used. This feature has a collision detection algorithm that allowed for very close positioning of the tibia and fibula to the talus without contact. The toe curling was also addressed in a similar manner. In the neutral position, the phalanges of all five

rays were curled down into the floor plate. It was desired for the metatarsals to, as they do in stance, be the strongest distal point of contact for the foot. The phalanges were rotated into dorsiflexion just enough to clear them of floor plate contact, clearance visible in Figure 3.14.

NOTE: .stl choice: the previous foot model was created from .iges profile lines[44]. These lines served as guide profiles to define a lofted surface. This method had two potential drawbacks that were mentioned in the previous work. The first is that while the profiles guided the creation of smooth lofted bone, at 1mm resolution there is the likelihood that some surface detail could be lost, particularly at articular ends. Of even greater importance was the second drawback. The guide curves were created only in the axial direction, thus the articular surfaces themselves (most at the ankle located superior or inferior) were missing. The lofted surfaces required a manual "capping" that was a user created geometry and thus derived indirectly from the scanned anatomy. Details of this process are available[44]. The largest benefit of using the .stl method is that a 3D mesh of the entire surface of the bone, not just an axially wrapped surface description, is created. No capping or individual attention is required at all to bony ends or articular surfaces. All procedures performed on the bones are smoothing and simplification algorithms - no manual editing of geometry on the gross scale to fill large missing geometry is required.

Modeled Hardware

Two mechanisms were created in SolidWorks to act as external boundary conditions. The first was a simple plate for the foot to rest on and be loaded against during simulation. To position this plate in near contact with the bottom of the foot, bones were briefly fixed immovable in space. The plate's upper surface was coincident mated with the most inferior points of the 1st metatarsal and calcaneus, then manually rotated against these two points to bring

it just into contact with the 5th metatarsal. The mates were then deleted and the plate was manually backed off the foot approximately ¼ of a millimeter. The importance of this is more clear in the COSMOSMotion section, but it removes a time zero contact force which can (and often did) cause simulation failure.

The second mechanism was a device to limit rotation and translation of the tibia and serve as a simulated load fixture, referred to here as a load indenter. This fixture mimics the function of loading devices used experimentally in the literature[46]. This device is a simple peg and collar that prevents translation of the tibia in all but the transverse plane and prevents all rotations (Figure 3.15). [**NOTE**: the initial load indenter was a concentric mate that did allow rotation about the z axis. As friction (discussed later) was not applied to the model, this would allow the foot to rotate or spin without warning during simulation. This was corrected by fixing the indenter to the tibia in COSMOSMotion.]

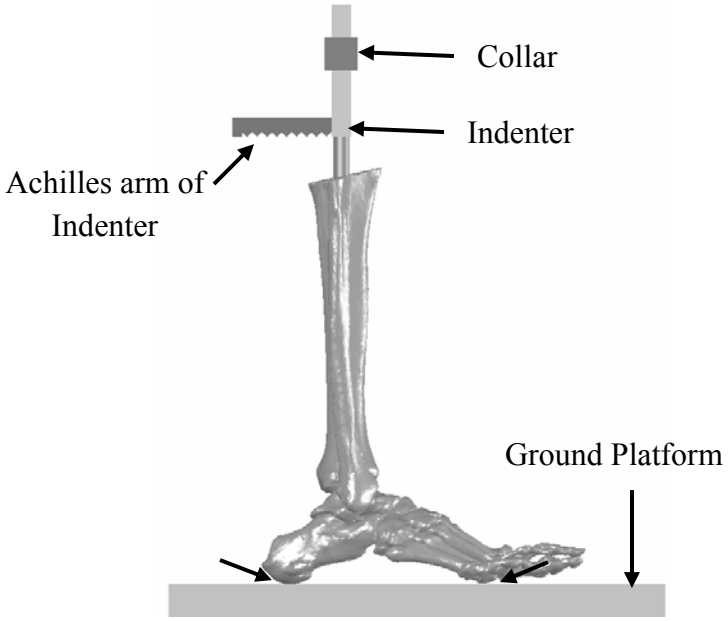

Figure 3.15: Foot and Leg with Indenter and Ground Plate. Assembly finished in SolidWorks space and ready for COSMOSMotion. Floor contact manually positioned for near-touching contact (arrows). Indenter in collar has a serrated arm for future origin of Achilles

tendon element location (next section). Collar is distance mated to ground plate to be vertical and immobile.

3.4 Initial Models: COSMOSMotion Parameters

COSMOSMotion is a rigid body motion simulation add-on to SolidWorks. It is capable of transferring and converting mates and relations from SolidWorks assemblies into pre-defined joint types and joint primitives. It allows the user to specify things such as contact between objects, gravity and other external perturbations (such as a load, torque, motion, etc…), internal relationships and boundary conditions with springs, dampeners, bushings and action-reaction forces and constraints in the model (i.e. a part that is fixed or "grounded" and parts that are moving). Once a scenario is created, the interaction of the various internal and external conditions can be set into motion over a user specified time course. Results from a simulation include such things as position, velocity, and acceleration of solid bodies, contact forces, and loads in spring elements or action reaction forces. The following sections describe the basic parameters of model formulation in COSMOSMotion including ligament elements, 3D contacts and solver parameters.

Soft Tissue Modeling

The network of ligament structures were added to the bony anatomy through COSMOSMotion using, over time, a variety of methods which are presented here. The recreated soft tissue anatomy of these structures was developed with study of the aforementioned myriad of sources: illustrated anatomy text, text with both illustrated and pictured dissections, peer reviewed literature, and in house dissection of specimens – more significant structures were described in Chapter 2.

Spring Elements

These ligaments, as modeled in previous work, were created with spring elements in COSMOSMotion that resisted both tension and compression as a function of displacement. They were defined on the anatomy by selecting a single vertex on the originating bone and a single vertex on the inserting bone. For models that used a single spring to describe a ligament structure, the origin and insertion of the element was determined by the rough center of that ligament's anatomy. The spring elements operate based on typical linear spring behavior and some defining parameters (Figure 3.16).

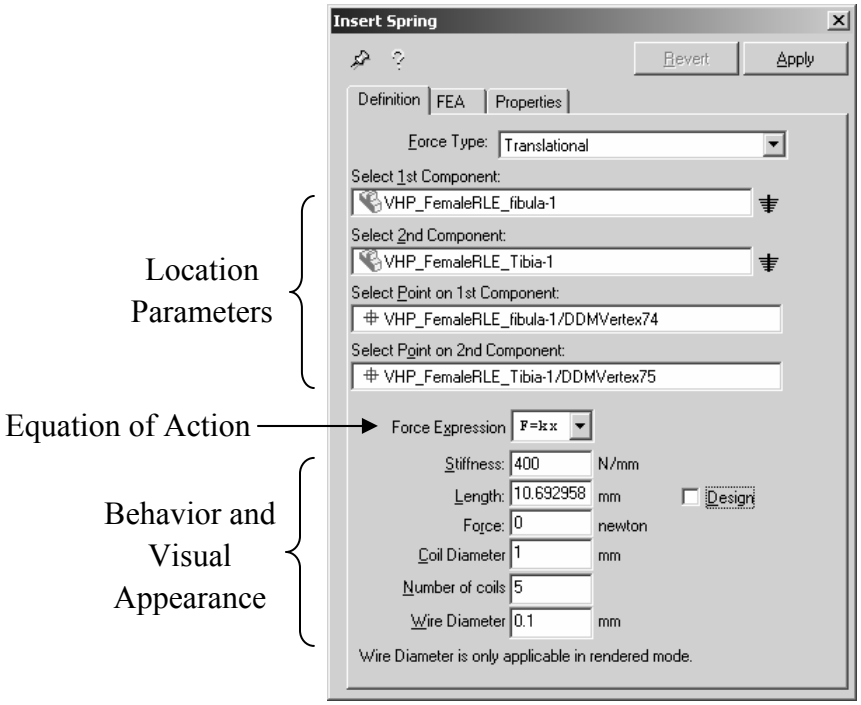

Figure 3.16: Spring Element Definition Pane. Element placement selection boxes and spring behavior parameter inputs. Spring elements are defined based on part and vertex parameters, a simple linear spring expression described the action of the element, where "F" is the force the spring applies in Newton's, "k" is the spring constant (defined in the next entry block), and "x" is the displacement of the spring from its starting point. User can also define the starting length

of the spring as well as a starting force. Other options are purely for appearance of the element in the simulation window.

Tension Only Elements

Action reaction force elements are a class of objects in COSMOSMotion that can be applied to simulations in the same way as spring elements. These elements furthermore are very versatile and powerful with respect to how they can be defined (Figure 3.17)

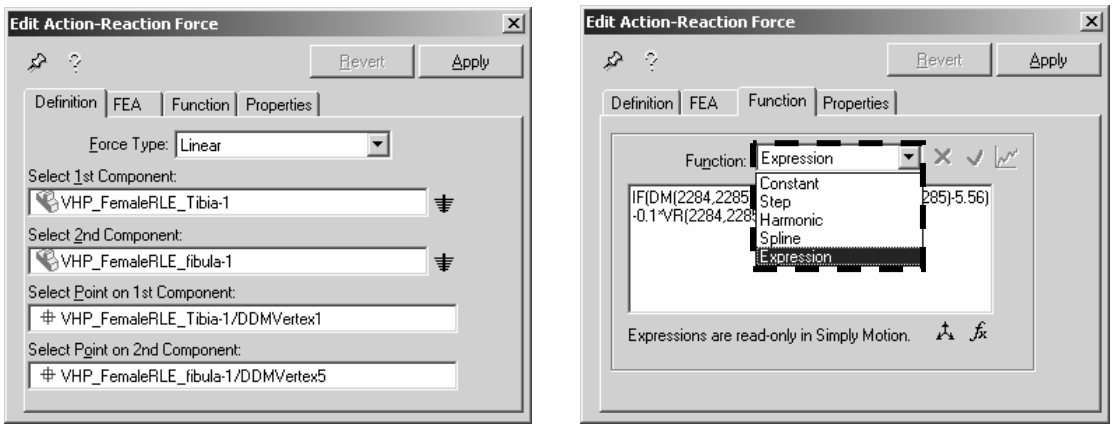

Figure 3.17: Tension Only Element Design Panes. These element's locations are defined the same way a spring element is. The function expression however is much more powerful. These elements can be defined by a constant, step, harmonic, spline, and expression. The expression option allows you to formulate more complex expressions of function based on more customizable real-time simulation parameters (function callout).

The action of these elements, when described by an equation, can be programmed to respond in tension only past a certain length. Using markers, which are computational placeholder values that identify the origin and insertion of such an element, and a C or FORTRAN like expression was used to create more complex functions. Programmable function

variables, such as “DM” which is the real-time distance between two markers, and “VR” which is the relative velocity between the two markers, were used to create a ligament expression (Figure 3.18)

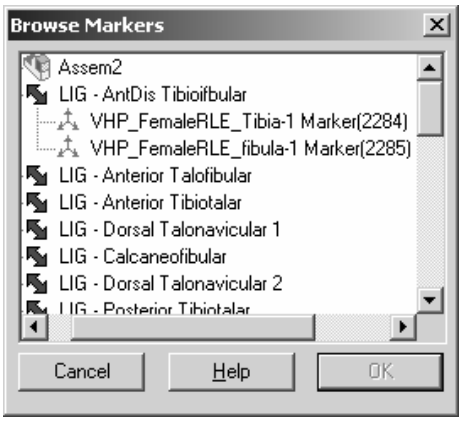

Figure 3.18: Marker Window. Marker selection window with a tibiofibular ligament expanded to show marker numbers. The marker window is a browser to find and select the vertices corresponding to the element being modeled.

Tension Only Action Reaction Expression

The following statement is the expression for the action reaction element’s to acting in tension only, defined by bony location, ligament stiffness, and a dampening expression (Equation 3.1)

IF(DM(2284,2285)-5.56:0,0,-70*(DM(2284,2285)-5.56)-0.1*VR(2284,2285))

Equation 3.1: Full Action Reaction Expression.

In the conditional expression, the “IF” statement is only ever equal to a non-zero number if the distance between markers 2284 and 2285 become greater than 5.56mm (measured length

between vertices of the element) during the course of the simulation. For all other lengths where the ligament is "slack" or "just slack" when the distance is less than or equal to 5.56mm, the tension in the element is 0 N (first and second term past the colon). Once passed 5.56mm of stretch, the force in the element is equal to some tension "X" (third term past the colon) (Equation 3.2).

IF(DM(2284,2285)-5.56: 0, 0, X…

Equation 3.2: Conditional Portion of Action Reaction Expression.

This portion of the expression determines the force response of the element after it passes its slack length. The tension in the element (tension denoted by the minus sign), is equal to the stiffness constant (70N/mm) multiplied by the distance the ligament is elongated past the designed slack length of 5.56mm (Equation 3.3).

…-70*(DM(2284,2285)-5.56)…

Equation 3.3: Force Determining Expression.

This tension value is further influenced by a dampening function. The dampening function increases the tension of the ligament by 10% of the velocity between the two markers (adding a negative to a negative).

…-0.1*VR(2284,2285))

Equation 3.4: Dampening Expression.

As the solid bodies joined by the element move past the elements slack length, tension increases to resist further displacement, effectively countering their movement as natural ligaments would. This tension prevents such things as subluxation of joints, etc. To increase the rapidity of this action, the dampening feature increases tension, and only allows it to relax as the bones are slowed in their displacement from one another. The value of 10% was chosen (from trial and error) to be effective in reducing simulation instability while not greatly increasing the simulation time required to reach equilibrium.

3D Bony Contact

COSMOSMotion requires the user to define a relationship between interacting objects in motion simulation. This relationship can be a joint which is created either in COSMOSMotion by directly defining joint geometry, as well as from a series of mates in SolidWorks that can and will be automatically grouped into a joint (such as defining several mates to create the action of a hinge. COSMOSMotion will realize that these mates describe a hinge, and substitute it upon first activating the add-on for that assembly). Additionally, there is a second form of contact possible through 3D contact. 3D contact calculates contact based on solid body interaction that is completely free of any joint or joint primitive motion restrictions. The intent of this model was for bony contact to be primarily stabilized by ligament constraint and bony articular anatomy. To this end 3D contacts were used extensively, all bones which articulated were defined in a 3D contact "container" (Figure 3.19, left). This means that COSMOSMotion looks for potential contact between any of these bones, against any other bone in the container, at each time step. If contact is determined, there are a variety of simulation parameters which dictate how the contact is handled (Figure 3.19, right).

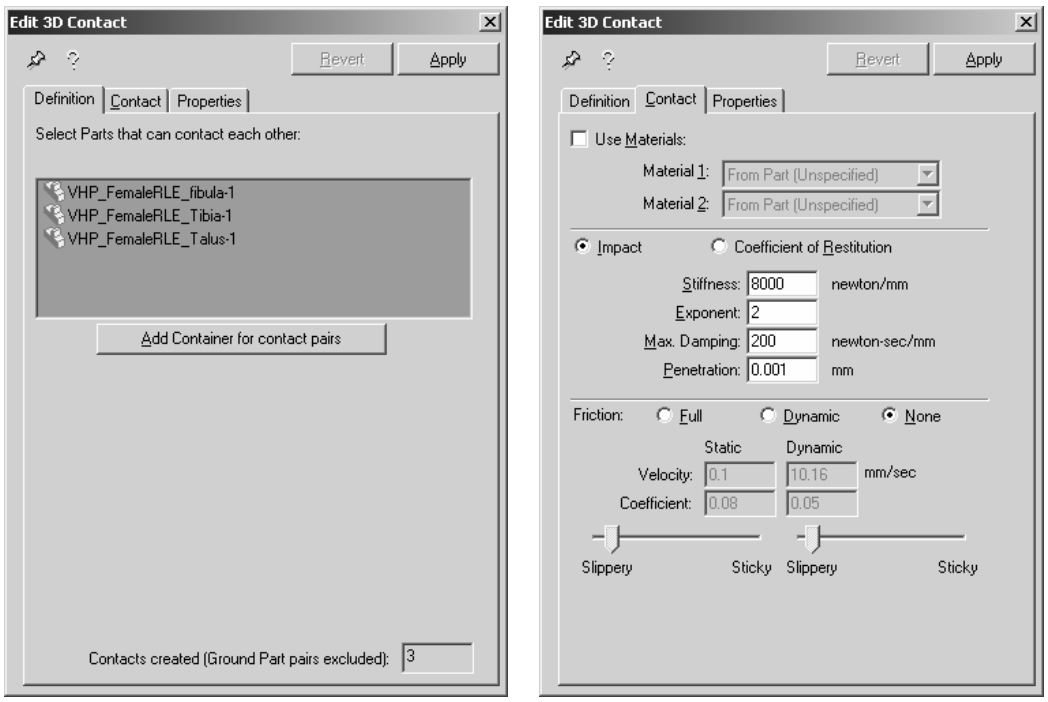

Figure 3.19: 3D Contact Parameters. 3D contact bin as well as behavior options and parameters. The contact container is a list of all solid bodies which will be checked for interference (contact) during simulation for the simple ankle model, left pane. The contact parameters are entered into the second tab of the property manager. As contact was manually defined, the "Use Materials" was never employed. The second area of the pane listed "Impact" properties allows the user to define how contact is handled during simulation. As articular surfaces have a very low coefficient of friction, and in the interest of time (simple models with friction ran 10x longer, if ever), the contacts were assumed frictionless. Note that simulating frictional behavior was prohibitive (does not complete) with respect to computational time.

The impact properties are "stiffness", which generates a compressive, repelling force centered at the volume of 3D contact between 2 parts, given in N/mm. The "exponent" determines the characteristics of the exponential force function for the collision. "Max dampening" is the greatest dampening value that interacting parts will experience, and

"penetration" is the distance these parts will have to move through each other to reach the max value. Selected values for these properties are given in later sections.

Simulation Parameters

The final step after bony geometry modeling, ligament modeling and contact definition, is to set global commands and parameters for running the simulation. These parameters are grouped in several tabs to allow the user to control the duration and quality of the simulation (Figure 3.20, Figure 3.21).

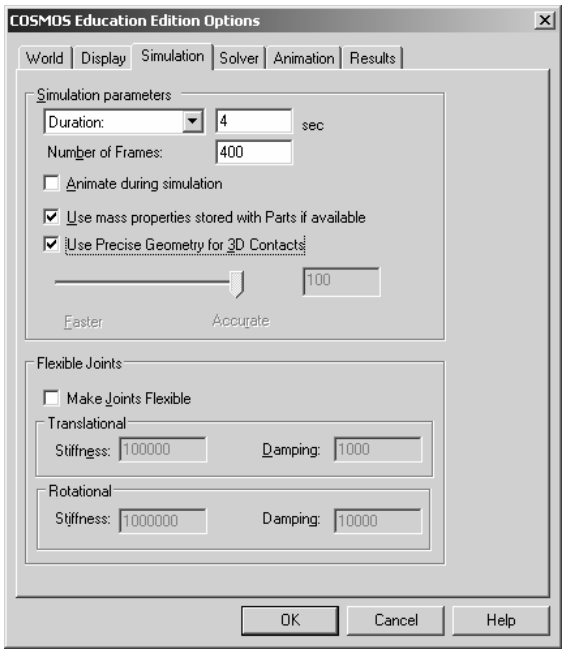

Figure 3.20: Simulation Parameters, Simulation. User adjustable parameters tab with typical simulation values entered. This tab allows the user to specify information about simulation duration, and basic part interaction with the motion environment.

The upper portion of this tab allows the user to dictate how long the simulation should allow motion (in simulation time) such that parts moving at 4m/s will travel 16m during a 4s simulation. The number of simulation "frames" can be set, but this value can be increased by the

solver if further time steps are needed to resolve the simulation. The "Use mass properties" checkbox prevents COSMOSMotion from taking additional time to re-calculate properties such as center of mass and moment of inertia. As all these parameters were present in the part files, this was unnecessary and significantly reduced computation time (~5-10min). "Use precise 3D geometry" and the slider bar associated with it allow the user to adjust the facet tolerance when the motion simulator determines how parts interact with each other. Further details of the use of these parameters are found in the results of these models in the following sections.

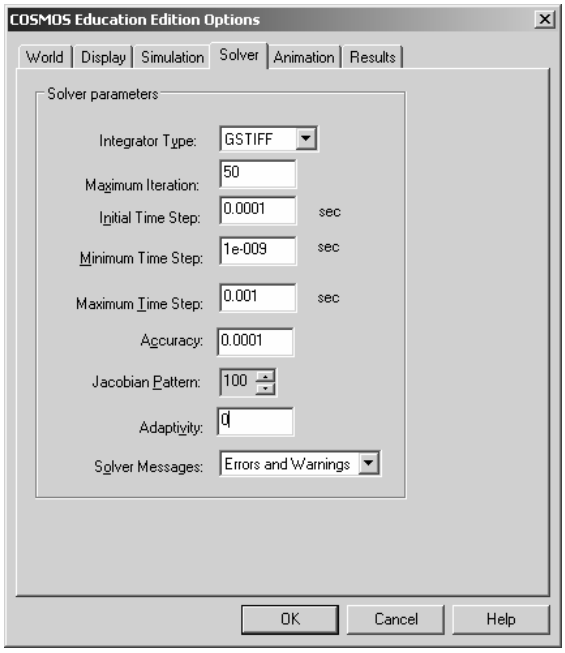

Figure 3.21: Simulation Parameters, Solver. Solver control tab with common simulation values entered. The solver tab allows the user to modify a multitude of parameters such as how the integrator attempts to solve the simulation and under what conditions it should seek a smaller time step or move to the next one.

The "integrator type" is based on what behavior the user expects and how much computation power is available for modeling. The options are GSTIFF, WSTIFF, and SI2

GSTIFF. GSTIFF is the default and is most kind to computation time, WSTIFF has some strength in calculating oscillating systems, and SI2 GSTIFF is tailored slightly for small step size accuracy. GSTIFF was used for these simulations. "Maximum iteration" and the various time step parameters specify under which conditions and to what levels the simulator can modify step size in an attempt to find a solution for that particular simulation frame. "Accuracy" is a scale between convergence speed and accuracy of results. The remaining conditions refer to how failed simulations are reported and adjustments to the deeper mathematics of the solver which are not publicly available.

3.5 Initial Models: Variants and Basic Performance

The initial models are briefly discussed; depth is spared only in discussing significant improvements or difficulties. In total, there were approximately 14 full models created from the female NLM-VHP scan data, many of which were tests of small changes, improvements in simulation stability, and explorations. The bulk of their usefulness was in discovering the initial and final methods of model creation reported previously and in the "Final Refinements" sections.

Initial Ankle Model

The earliest model was an ankle recreation of the prior model by Liacouras[44]. This model contained only 3 moving bones, the tibia, fibula, and talus (Figure 3.22). It served as a test platform for tension only ligament elements. An averaged stiffness was applied to all ligaments with the exception of the interosseous membrane which was modeled very stiff (Table 3.3). This stiffness was chosen to reduce the oscillating movement between the tibia and fibula due to the lack of a proximal articulation for these bones. Some variations of this model were created with 2% *in situ* ligament strain.

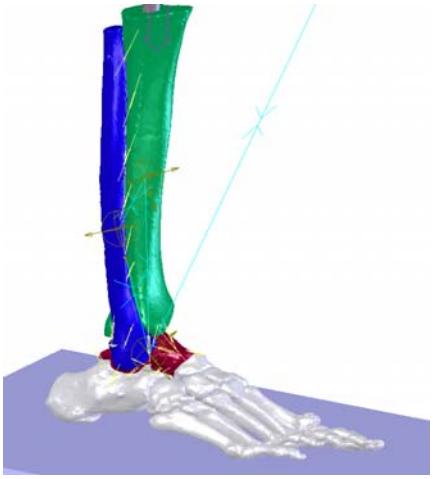

Figure 3.22: Tension Only Ankle Model. Tibia, green; fibula, blue; and talus, red, were the only bones allowed movement. Most ligaments described with a single element.

Ankle Only Model	Stiffness
Anterior Tibiofibular	70
Anterior Talofibular	70
Anterior Tibiotalar	70
Calcaneofibular	70
Dorsal Talonavicular 1	70
Dorsal Talonavicular 2	70
Interosseus 1	400
Interosseus 2	400
Interosseus 3	400
Interosseus 4	400
Interosseus 5	400
Interosseus 6	400
Interosseus Talocalcaneal 1	70
Interosseus Talocalcaneal 2	70
Lateral Talocalcaneal	70
Medial Talocalcaneal	70
Posterior Tibiofibular	70
Posterior Talocalcaneal	70
Posterior Talofibular	70
Posterior Tibofibular	70
Tibiocalcaneal	70
Tibionaviuclar	70

3D Contact Parameters	
Bones / Solids	tibia, talus, fibula, calcaneus, navicular
Stiffness	8000
Exponent	2
Max Dampening	200
Penetration	0.001

Table 3.3: Initial Models: Ankle Model Ligament Parameters. Modeled ligaments listed along with stiffness values, left. 3D contact parameters and which bones were applied to the contact, right.

The main purpose of this model was a starting point that had been reached previously. This model was used for a variety of small adjustments in solver, contact, and ligament parameters and helped explore the computational capability of a newer version of SolidWorks, COSMOSMotion, and upgraded hardware.

Initial Full Foot Model: Spring Elements

Briefly setting aside tension only elements, springs were employed in the first several iterations of the full foot model. This model permitted movement of all bones with the exception of the phalanges which were fused to their respective metatarsal. Additional anatomy was added around the ankle, hindfoot, midfoot, and forefoot to account for the increase in bony mobility (Figure 3.23). Increased anatomical detail, and thus added stability through ligament stiffness' in more accurate 3D depiction, as reported in literature were applied to portions of the medial arch to bolster the spring ligament and short plantar ligament. This model incorporated 84 spring elements to describe 33 structures of the foot (Table 3.4). Extensive bundles were created to describe the small capsule / ligament network of the dorsal and plantar midfoot. Major portions of the long and short plantar ligaments appear in this model, but the plantar fascia is absent. The spring ligament was bolstered to include what will become the final description of its superior, medial, and inferior bands. Many structures of the ankle were still described by a single ligament. This model was explored with 2% *in situ* strain as well. Use of spring elements gave difficulty in determining what effect, if any, the pre-strain caused. These models continued to use generic 70N/mm stiffness for most tissues. Early changes to these values were based on the size of structures as found in dissection and literature text[29-34]. Final models employed the full range of values found in later literature[31,42,43].

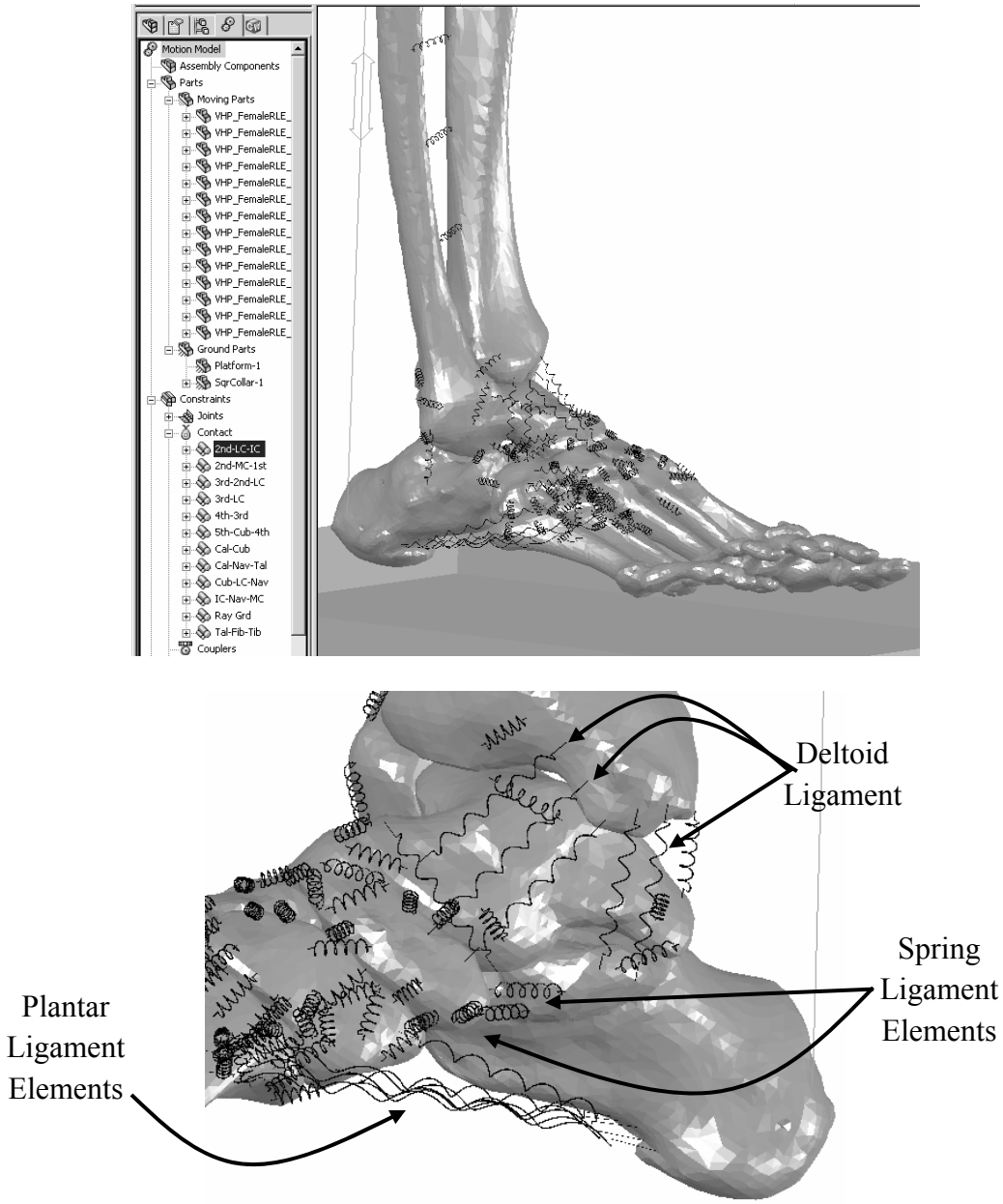

Figure 3.23: Initial Models: Full Foot Model. Foot on ground plate, ligament spring elements in black (visible through bony anatomy). Note 3D contact groups (top). Plantar structures were simplified in these models, plantar fascia was not yet incorporated (bottom).

Foot Model with Spring Elements			
Ligament	**Stiffness**	**Ligament**	**Stiffness**
Anterior Talofibular	70	Interosseus Talocalcaneal 2	70
Anterior Tibiofibular	70	Lateral Talocalcaneal	70
Anterior Tibiotalar	70	Long Plantar 1	70
Calcaneal Cubiod	70	Long Plantar 2	70
Calcaneofibular	70	Long Plantar 3	70
Calcaneonavicular	70	Long Plantar 4	70
Dorsal Calcanealcuboid	70	Medial Talocalcaneal	70
Dorsal Cuboidenavicular	70	Plantar Calcaneocuboid 1	210
Dorsal Cuneocuboid 1	70	Plantar Calcaneocuboid 2	210
Dorsal Cuneocuboid 2	70	Plantar Calcaneonavicular (Spring) 1	140
Dorsal Cuneonavicular 1	70	Plantar Calcaneonavicular (Spring) 2	140
Dorsal Cuneonavicular 2	70	Plantar Calcaneonavicular (Spring) 3	140
Dorsal Cuneonavicular 3	70	Plantar Cubiocuneiform	70
Dorsal Cuneonavicular 4	70	Plantar Cuboideonavicular 1	70
Dorsal Intercuneiform 1	70	Plantar Cuboideonavicular 2	70
Dorsal Intercuneiform 2	70	Plantar Cuneonavicular 1	70
Dorsal Metatarsal 1	70	Plantar Cuneonavicular 2	70
Dorsal Metatarsal 2	70	Plantar Cuneonavicular 3	70
Dorsal Metatarsal 3	70	Plantar Cuneonavicular 4	70
Dorsal Metatarsal 4	70	Plantar Intercuneio 1	70
Dorsal Talonavicular 1	70	Plantar Intercuneio 2	70
Dorsal Talonavicular 2	70	Plantar Intermetatarsal 1	70
Dorsal Tarsometatarsal 1	70	Plantar Intermetatarsal 2	70
Dorsal Tarsometatarsal 10	70	Plantar Intermetatarsal 3	70
Dorsal Tarsometatarsal 11	70	Plantar Intermetatarsal 4	70
Dorsal Tarsometatarsal 12	70	Plantar Tarsometatarsal 1	70
Dorsal Tarsometatarsal 13	70	Plantar Tarsometatarsal 2	70
Dorsal Tarsometatarsal 14	70	Plantar Tarsometatarsal 3	70
Dorsal Tarsometatarsal 2	70	Plantar Tarsometatarsal 4	70
Dorsal Tarsometatarsal 3	70	Plantar Tarsometatarsal 5	70
Dorsal Tarsometatarsal 4	70	Plantar Tarsometatarsal 6	70
Dorsal Tarsometatarsal 5	70	Plantar Tarsometatarsal 7	70
Dorsal Tarsometatarsal 6	70	Plantar Tarsometatarsal 8	70
Dorsal Tarsometatarsal 7	70	Plantar Tarsometatarsal 9	70
Dorsal Tarsometatarsal 8	70	Posterior Talocalcaneal	70
Dorsal Tarsometatarsal 9	70	Posterior Talofibular	70
IOM 1	70	Posterior Tibiofibular	70
IOM 2	70	Posterior Tibiotalar	70
IOM 3	70	Tibiocalcaneal Part 1	70
IOM 4	70	Tibiocalcaneal Part 2	70
IOM 5	70	Tibionavicular Part 1	70
Interosseus Talocalcaneal 1	70	Tibionavicular Part 2	70

Table 3.4: Initial Models: Full Foot Ligament Parameters. List of ligaments and elements describing them. Early elements constrained bony motion with 1 element per ligament, here arrays being to substitute ligament structures over single elements.

3.6 Initial Models: Failure Modes

Before describing the performance of these early models, the common failure modes must be defined. These failures were common and quite similar, persisting throughout even the latest generation of model. Over the course of the evolution of the foot model presented here, many of the reasons for these rather ambiguous failures have been gleaned through trial and error. Failures and their known or suspected causes are listed here for reference when considering model performance in future sections.

Failed simulation runs typically expressed a short list of failed messages / model breakdown. These failures include sudden loss of 3D contact, violent model expansion, unbounded oscillation of one or more parts, as well as a cryptic failure window that would cite several possible failures with reference to hidden COSMOSMotion solver equations.

Loss of 3D Contact: This was visible when the model "fell" through the floor plate, or when bones of the model – which were in solid contact for several frames - suddenly passed through one another and crashed the simulation.

Violent model expansion: A variation on oscillation whereby sudden increases in contact forces or ligament tensions tore the model apart by displacing all the components. This was rarely a gradual process, commonly one frame of simulation would be "normal" and the next would have bones displacing over several hundreds of meters.

Unbound Oscillation: If a solid object was poorly restrained, or a 3D contact partially failed and allowed a bone to dislocate past its ligaments ability to restrain, the part would "rattle" for the duration of simulation, with a significant increase in solver time (~5x) and poor model results.

3.7 Initial Models: Overall Performance

These early models were not intended to generate clinical and experimentally relevant data. These models were early proofs of concept and explorations into how and the extent by which these programs could be used to represent and model physical tissue behavior. Just as MIMICS techniques were explored to obtain complete bony geometry and minimizing user error in reconstructing lost geometry, these models explored issues of developing a complete foot model with increasingly realistic soft tissue constraint.

Anatomy Capture Findings: The exploration into using .stl derived geometry showed the concept was successful and very hands off with respect to the 3D geometry. The use of the triangulated mesh did not impart any noticeable oscillation of bone contact or simulation failure due to geometric binding or problems with bone inter-digitations. The ankle model proved very stable, and most of the full foot spring element models did not exhibit unusual binding.

SolidWorks Assembly: The assembly of the foot and modeling of the associated hardware was done without significant difficulty.

COSMOSMotion Simulation: The ankle simulation with tension only elements excitingly demonstrated that this method could be used to define ligaments. The 2% *in situ* strain however, was seemingly lost in bone gap closure because the articular cartilage is not visible on CT scans. Additionally the performance of the model using the "100% accurate geometry" slider-bar option improved simulation time. No noticeable difference in model equilibrium position was found when "use precise geometry" checkbox was selected (the geometry can be slightly simplified based on a curvature tolerance setting which is adjusted by that slider). The ankle model simulation with these parameters had a computation time of approximately 1 hour. While

tension-only elements stabilized the ankle only model enough for simulation, conversion to the full foot was done with spring elements in a gradual approach.

Though ligaments do not resist load to significant levels in compression, the spring elements were very helpful in stabilizing the model (preventing bony movement both in tension and compression) as the greatly increased mobility of the foot was explored. This increasing mobility required extensive further description and modeling of ligaments in terms of the number of spring elements, to properly constrain the foot. In the third model, even incorporating the early improvement of ligament arrays that would dominate final models, the entire structure of the foot was less stable during simulation and prone to various failures. Furthermore, runtime was increased to approximately 2.5 hours.

Problematic to both simulations was the missing proximal tibial and fibular geometry. The two bones abruptly ended in space and were only tied together with the half portion of the interosseus ligament, which was modified for greater stiffness in an attempt to compensate for the lack of bony rigidity. The absence of a proximal articulation and the associated ligaments binding it was suspected to be a significant source of the instability in the model. In several failed runs, the fibula was seen to move or gyrate in extreme.

As the model creation and simulation problems arose, strategies were developed to overcome them. These significant changes bridge the gap between the early proof of concept models and the final simulation which was fit for validation.

3.8 Final Refinements: Scan Geometry

The NLM-VHP male and female datasets were found to be inadequate for the needs of this simulation. Primarily, the loss of data coherence at the tibial level precluded use of full below-knee anatomy without extensive manual scan processing. Furthermore, the non-neutrally

aligned ankle and distorted position of the forefoot joints in both scans would also require extensive user manipulation to achieve neutral position. And lastly, the foot in both scans was randomly oriented in the scan field. This lead to further difficulty in interpretation of data which is generated with respect to fixed global x,y,z axes. There was no ability to reorient the assembly or assign a local orientation to view data in, further manual movement of the foot was necessary. Ultimately, these problems led to an unacceptable amount of adjustment of the original scan to yield usable results.

Scan Fixture

An in-house CT scan was planned and performed to address all of these problems. In preparation of the scan there was an interest in obtaining both an unloaded scan of the leg and a scan under simulated body weight. To fit these needs as well as to maintain alignment of the specimen with respect to the scan field, a specimen holder was devised (Figure 3.24).

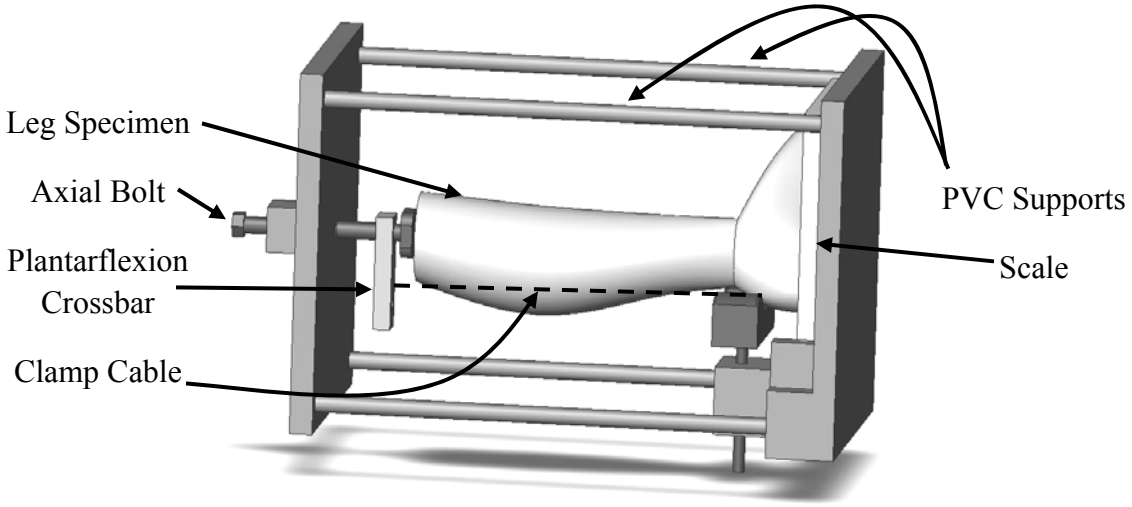

Figure 3.24: Specimen Holder for CT scan. Specimen holder with mounted specimen in place. The holder was build to fit into the CT scanner and impart minimal artifact into the scan. PVC was used to support the sides to reduce this artifact. Some metal components were

necessary, such as the clamp (not shown), cable, bolt fixtures, and scale. Top and bottom plates were made of wood.

The requirements for this holder were to apply 100 lbs of axial load on the specimen through the proximal tibia as well as to apply 100 lbs of pull on the Achilles tendon to simulate a standing plantarflexion. The holder also had to be as radio-transparent as possible to minimize scan artifact. To accomplish these goals a small frame was made of wood and PVC to enclose the leg. This frame held a typical bathroom floor scale to display ground contact force to within 5 lb increments.

Proximally, a heavy screw and collar were built into the frame. The end of the screw was fed through a plate and into a hole in the tibial plateau. When the screw was tightened in the frame, the plate would push against the tibia, exerting an axial force, guided by the screw's placement in the tibia. In this manner, a simulated axial load could be applied proximally and monitored at the foot distally with the scale.

To create a contractile force on the Achilles tendon, an aluminum crossbar was attached to the axial screw, this crossbar housed a second screw. This screw was fed through the center of a stiff spring before passing through the crossbar. The end of this second screw was drilled through with a $3/16^{th}$ inch hole to allow a wire cable to be passed through it. The cable was passed under and through the gasterocnemius / soleus complex and terminated at a steel clamp which was bolted around the distal Achilles tendon. When the second screw was tightened in its crossbar housing, it compressed the spring. By measuring the compression of the spring, and having calibrated the spring previously, ~100 lbs of force could be applied to the Achilles tendon.

Scan and Fixture Performance

Prior to the day of scanning, a cadaveric (61 year, female) fresh frozen right leg with foot, disarticulated at the knee, was thawed overnight. The original intention was to scan an intact leg; however, due to a bookkeeping error on the part of the author-which was not discovered until the day of testing, the abovementioned leg had received a Medializing Calcaneal Osteotomy (MCO, visible in the following figures) for use in an experimental study. The scan proceeded nonetheless and virtual restoration of this osteotomy to the intact state is discussed in the next section.

The CT scanning system was a SOMATOM Sensation 64 helical scanner (Siemens AG, Forchheim, Germany). The frame and specimen fit well onto the patient table and through the scan aperture. The scanner came equipped with a laser axis illuminator that assisted in aligning the specimen with the axis of the scan field.

Prior to scanning, the specimen was loaded by tightening both axial and Achilles tendon screws. The frame ultimately was not rigid enough to maintain the axial and plantarflexion loads at 100lbs. Due to frame deformation and specimen shifting under load, only approximately 75lbs of load were achieved during scan, and the shifting of the specimen placed it off axis in orientation. The unloaded scan proceeded without incident and near perfect alignment was easily achieved with the frame holding the specimen. The helical scanner creates a virtual slice resolution, the finer scan resolution available, 0.6mm, was employed. Several scan post processing options were performed in the scanner software in attempts to visualize the soft tissues. These additional scans brightened the bulk of the soft tissue but demarcation between structures was not improved. For processing, the default bone CT was used.

While an ideal loaded specimen scan was not achieved, the positioning and orientation of the specimen in the holder and in the scan field eliminated all of the problems associated with the earlier NLM-VHP scan data.

3.9 Final Refinements: Scan Processing

The same methods in MIMICS used for earlier models derived from the NLM-VHP were applied to the in house scan. The past experience of processing scan data allowed this process to proceed in a more rapid and organized manner. Each bone was systematically isolated, filled to solid, and converted to .stl for export. The two exceptions to this were the proximal tibia and the calcaneus. The proximal tibia was in contact with the axial load plate and axial screw of the scan frame. This frame was used even in the unloaded scan for alignment of the ankle joint and of the specimen in the scan field. The presence of these steel components caused some scattering and artifact of the scan at this location (Figure 3.25). Manual cleanup of this artifact was required- not in an effort to preserve the proximal tibial joint surface (which was attempted) but to fill unusual voids left by the artifact, and remove artifact spikes extruding from the tibia.

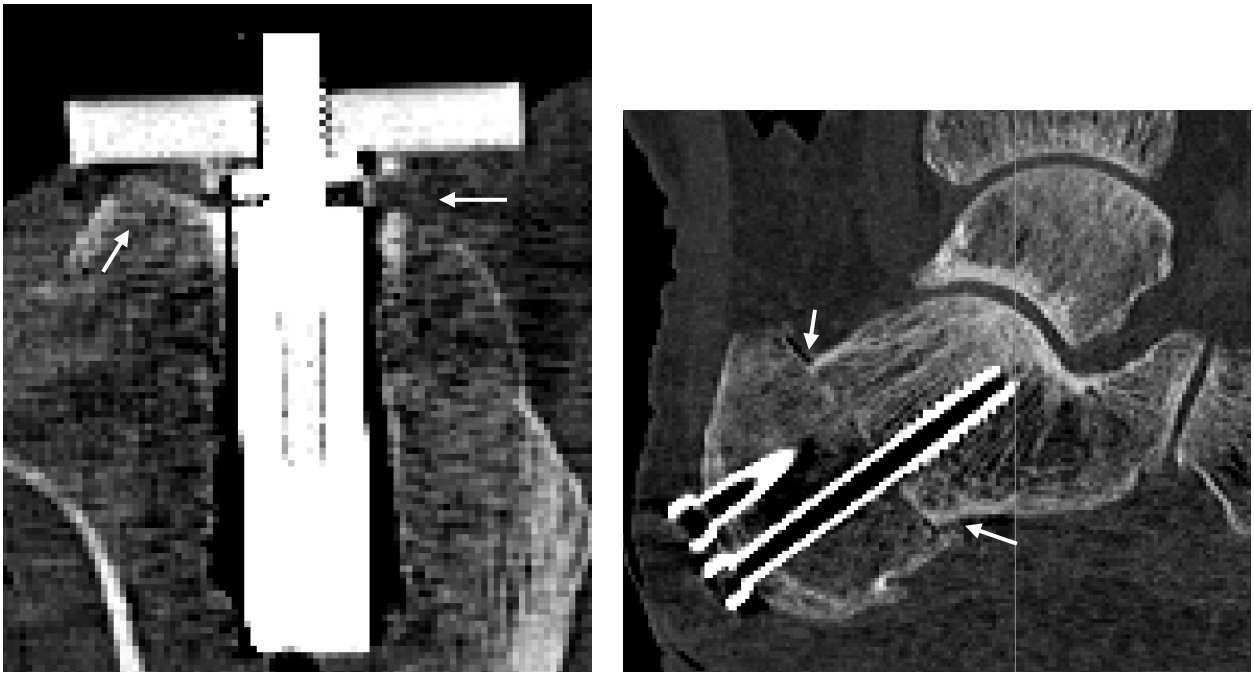

Figure 3.25: Scan Artifact at Metal Components and MCO. Proximal tibia distorted slightly due to the axial loading plate and screw. This distortion was more due to the disruption of the tibial surface than scattering of the x-ray (arrows, left). The MCO and hardware showed up very clearly in the calcaneus where the screw metal did not appear to significantly distort the image (arrows, right).

Calcaneal Restoration

The calcaneus was an interesting challenge. The scanned calcaneus had a standard 1cm MCO applied to it. The first challenge was "cleaning up" the same artifacts as were seen at the tibia, due to the addition of 2 unicortical screws to fix the MCO in place. The second challenge was virtually un-doing the MCO to create an intact calcaneus. It was here that the remeshing subroutine of MIMICS was explored extensively. The triangulated .stl mesh of the rendered calcaneus could be manipulated at the mesh level in this subroutine. The osteotomized interface between the body and fragment could be removed using the remesher, however, the fragment could not be translated back to its original position. Additionally, using the remesher this way to

create smoothed geometry between the fragments would be very much done by eye. The .stl was brought into SolidWorks, opened and converted to a part file.

In SolidWorks, the osteotomy cut plane was built using a reference plane by selecting points around the calcaneus that were on the cut edge. Using this reference plane a zone approximately 0.5mm in depth to either side of the plane was isolated. This zone encompassed all of the rough edges of the MCO as obtained from MIMICS processing. This 1mm zonal segment of the calcaneus was then deleted. The depth of the MCO had been measured at the superior and inferior extends of the cut, and was verified at approximately 1cm. In SolidWorks the move feature was used to translate the calcaneal tuberosity fragment 1cm lateral to re-align it with the body of the calcaneus. On each zonal cut plane a fully enclosed multi-point spline sketch was drawn to create a detailed profile of the surface of the calcaneus. These two sketch profiles were used to describe a loft feature, which smoothly bridged the 1mm gap to join the two fragments again as one solid body (Figure 3.26). This solid was then converted into a new .stl output, and exported from SolidWorks back into MIMICS. In MIMICS a smoothing and triangle reduction feature was applied to create an unblemished, intact calcaneus. This smoothed .stl mesh was then re-opened and converted in SolidWorks back to a part file (Figure 3.27).

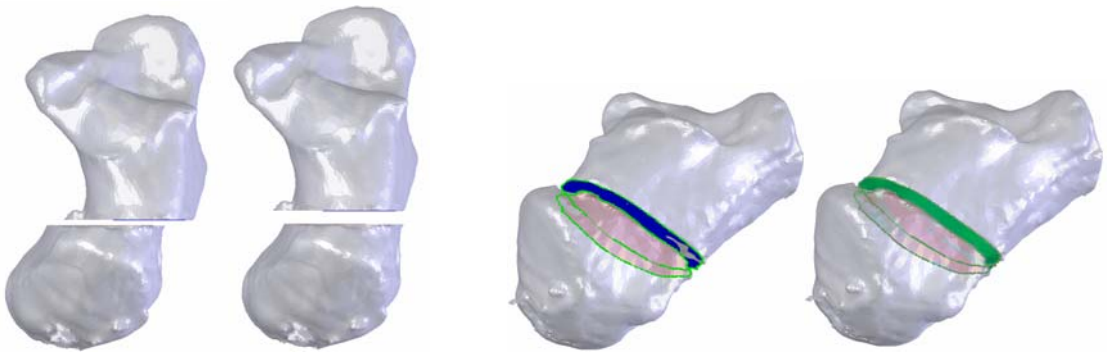

Figure 3.26: Calcaneal Editing To Remove MCO. Osteotomy zone cut and removed, then laterally translated 1cm to realign with the body, left two images – anterior view. Sketches made

on the cut surfaces (sketches highlighted in green, second from the right) yield profile lines for lofting a surface between the fragments (loft highlighted in green, semi-transparent bones for visualization of the full cut and loft fragment, right).

Figure 3.27: Stages of MCO Surface Smoothing and Remeshing. Scanned and meshed calcaneus, left; after application of lateralization and zonal replacement of the MCO cut surfaces, middle; and final remeshed geometry from MIMICS re-imported as a part, right.

To ensure that this second smoothing and reduction stage did not oversimplify the surface of the calcaneus, the original and final calcaneal surfaces were compared. The two calcanei were mated in SolidWorks to equalize their orientations. The original cut and lateralized calcaneus was colored yellow, and the remeshed intact was colored blue. When superimposed, it is clear that the two are the same size and shape, with only minute surface differences between them with no loss of detail or volume (Figure 3.28). While solving an unfortunate problem, the development of such a technique to use both SolidWorks and MIMICS in the editing and restoration of a bone was notable.

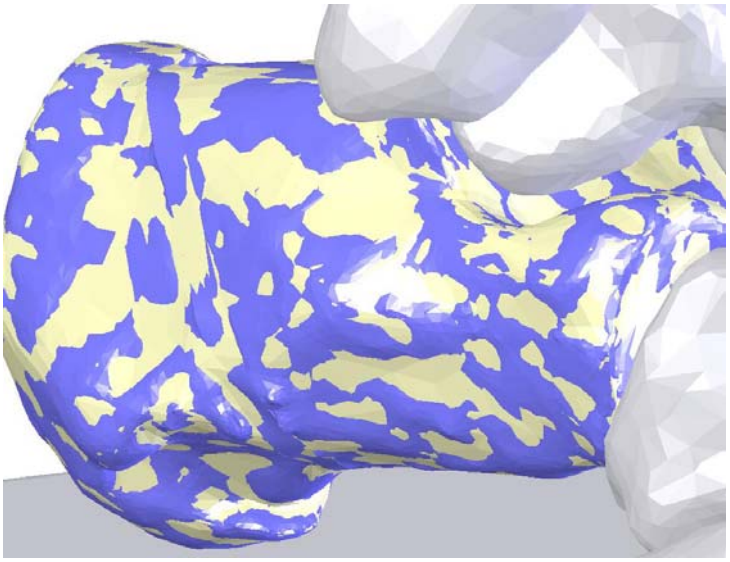

Figure 3.28: Calcaneal Registration For Surface Comparison. Yellow original calcaneal body (after cut and slide), superimposed in place with remeshed geometry in blue.

3.10 Final Refinements: SolidWorks Assembly

The assembly of converted bone part files followed the same course as the prior models. The mating of bone orientations to yield the scan position was followed by the addition of floor plate and proximal indenter virtual hardware. Though neutral joint alignment was preserved, due to soft tissue depth the distal phalanges were lower than the metatarsal heads. As in the prior model the phalanges were manually dorsiflexed a slight amount to allow metatarsal ground contact with the application of the floor plate.

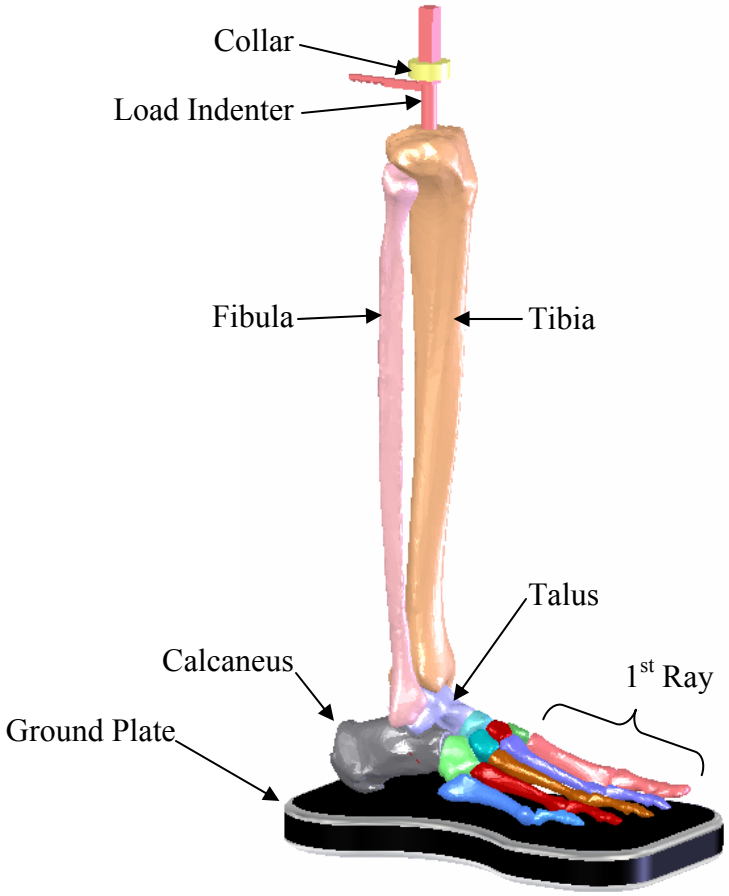

Figure 3.29: Final Foot Model, Overview. Complete SolidWorks assembly, including all bones and hardware. This setup and orientation was used for all final bone models.

[**NOTE**: In a further effort to reduce simulation failure via the bony anatomy losing its 3D contact with the floor plate and falling through (a problem that had for some time been attributed to the triangulated mesh contact with the ground) the contacting surfaces of the calcaneus and metatarsals were briefly modified with the addition of small dome features. These features replaced the underlying mesh geometry with a rounded dome described by a single rotated arc. It was thought that this SolidWorks created, simplified geometry would be handled more robustly by the 3D contact parameters in COSMOSMotion. This did not prove to be the case,

and the dome features were abandoned when solutions presented themselves in COSMOSMotions' definition of 3D contact (see next section).]

3.11 Final Refinements: COSMOSMotion

The bones of the foot model, as they are in the natural foot, are held in articulating opposition at their deepest layer by ligaments, and at increasingly superficial levels-and to a lesser degree-by stabilizing musculature, surrounding fatty tissue and even skin. The inadequate stability of early simulations, and more specifically the movement and constraint (or lack thereof) present at joints, led to further study on accurately describing the architectural network ligaments of the foot. At this stage a more extensive study of the anatomy through in house dissection and further ligament literature search was performed to describe the anatomy. When the ligament network was created for the in house foot model, many previously modeled ligaments were divided into more complex and three dimensionally accurate arrays of tension only ligaments – as will be demonstrated. Additionally, portions of joint capsule through the midfoot and forefoot were added wrapping these bones with action reaction elements to further link the tarsals and metatarsals in a more complete manner as they present naturally. The completeness of the new scanned anatomy also allowed for modeling of the proximal tibiofibular articulation.

Anatomy Refinements

Interosseous Membrane and Tibiofibular Articulation

For the interosseous membrane between the tibia and fibula, reported properties were found only for the interosseous membrane of the forearm. These values suggest a stiffness of 13.1 ± 3N/mm per mm of width. This stiffness per length value was based on the thickest

structure of the forearm which was isolated from surrounding membrane. The full distance between the proximal and distal tibialfibular articulations in the model is approximately 300mm. A buffer of about 20mm was applied to shorten both ends of this area to isolate the function of the interosseous membrane from these proximal and distal articulations. Further taking into account the presence of foramen in the membrane as well as considering the forearm stiffness was found at a thick middle band and not representative of the whole structure, a value of 3.5N/mm^2 was chosen to describe the action of this structure. This stiffness per length equated to an approximate 900N/mm total stiffness of the membrane. The composite stiffness of the membrane was divided amongst the seven elements representing the membrane (Figure 3.30). The proximal articulation was described with elements exhibiting 200N/mm of stiffness to put them in line with the stiffer structure of the ankle articulation (Figure 3.30).

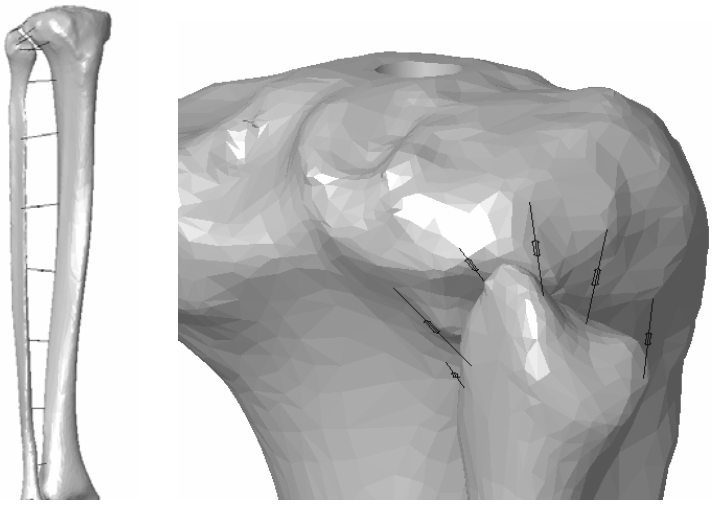

Figure 3.30: Interosseous Membrane and Proximal Tibiofibular Articulation. The seven elements of the interosseous membrane in an anterior view, left. The proximal tibiofibular articulation was described anterior, posterior and superior as seen laterally, right.

Ankle

The final lateral ankle structure incorporated the anterior and posterior tibiofibular, anterior and posterior fibulotalar, fibulocalcaneal, talocalcanal, and talocalcaneal interosseous discussed in Chapter 2 as well as some supporting structures not highlighted there (Figure 3.31).

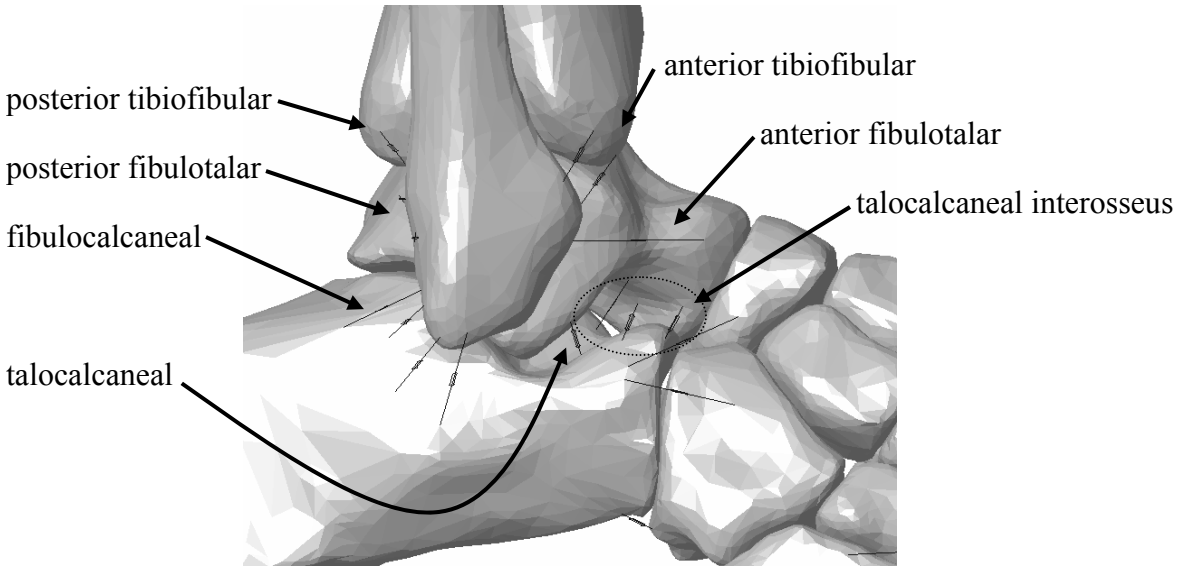

Figure 3.31: Lateral Ankle Ligaments.

The medial structures of the ankle including: anterior and posterior tibiotalar, talocalcaneal, tibiocalcaneal, tibionavicular, and tibiospring ligaments were modeled as arrays to describe the deltoid ligament and accessory medial and posterior structures (Figure 3.32).

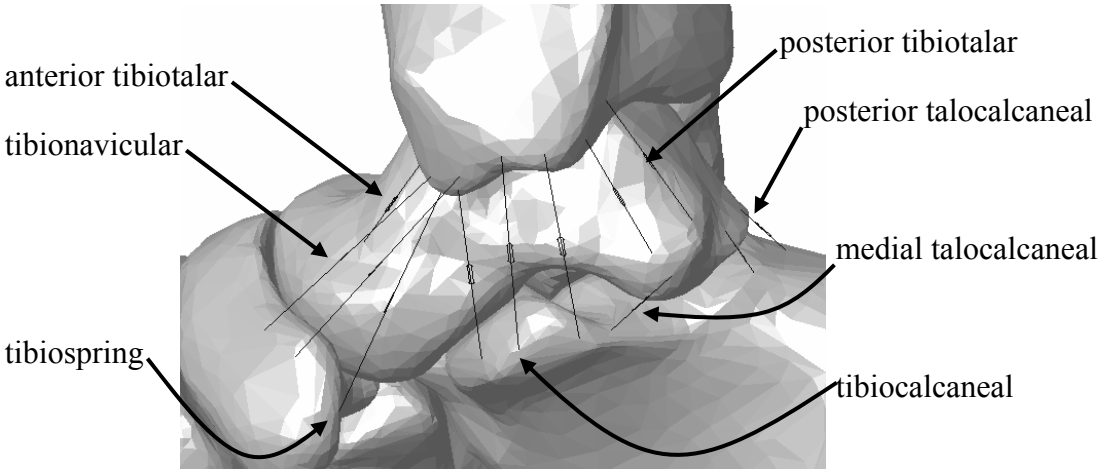

Figure 3.32: Medial Ankle Ligaments.

Spring Ligament Complex

The various portions of the superior, medial and inferior portions of the spring ligament were modeled with extensive arrays (Figure 3.33).

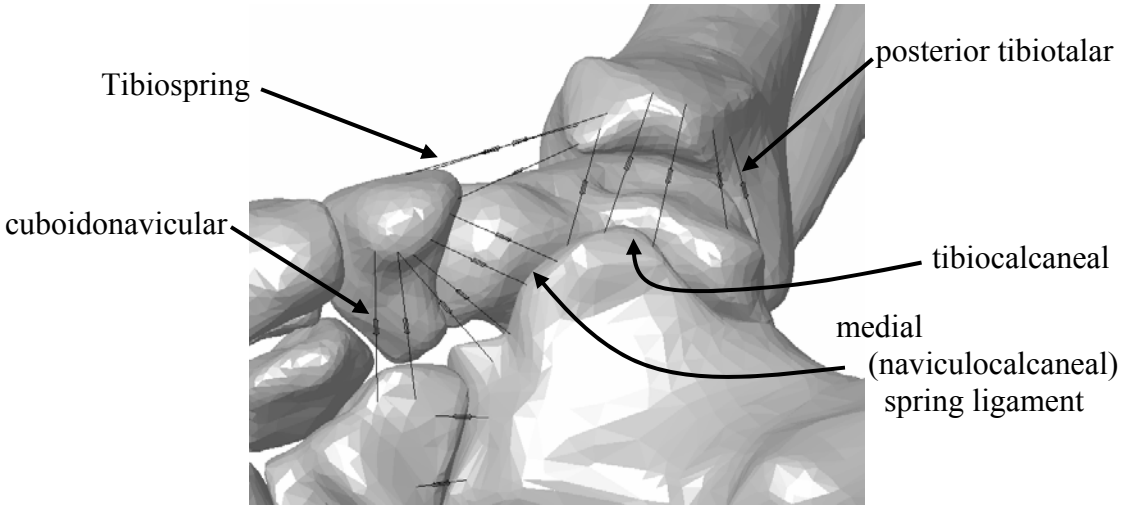

Figure 3.33: Spring Ligament Complex.

Midfoot

The capsular network of ligaments wrapping the mid- and forefoot were modeled with broad arrays to cover joint surfaces as seen from dissection and literature. The majority of these tissues, which have no reported stiffness values, were given 90N/mm of stiffness per element

used to describe them in arrays of 2-3 elements. If a single element was used for a structure it was given 120N/mm stiffness, slightly lower than the average 138N/mm stiffness of the reported ligaments. If a larger array was needed to describe the tissue, 60N/mm stiffness was used. These choices were based on observed size of these structures and additionally modified based on how extensive the arrays to model them were (which in turn is based on the 3D anatomy of the structure). These regions are shown superior (Figure 3.34, left) and inferior (Figure 3.34, right) below.

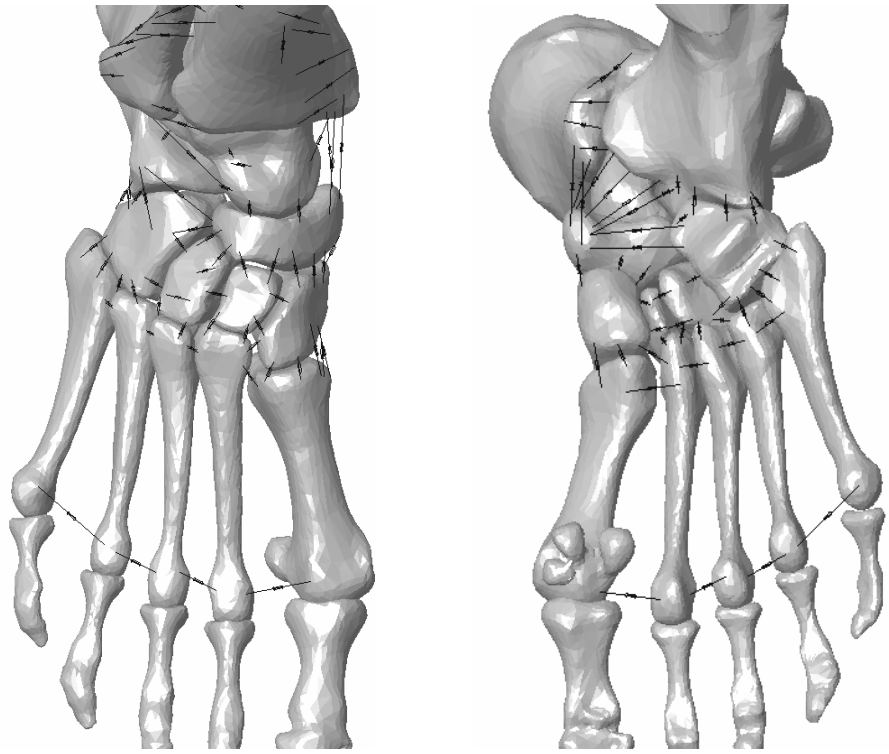

Figure 3.34: Dorsal and Plantar Ligaments of the Midfoot.

Ligament Wrapping

The long plantar ligament and the plantar fascia are both very large structures that span vast (on an anatomic scale) anatomy. The long plantar ligament crosses the inferior intertarsal joint to attach across a span of proximal and distal midfoot locations. A role this structure plays,

in addition to preventing separation of joints across these levels, is likened to a physical hammock for the central intertarsal joints. Portions of the calcaneus, cuboid, navicular, and cuneiforms articulate just above the plantar ligament. The ligament, as it exists in some amount of passive strain, acts in a fashion as a barrier to prevent large dislocation of these joints. The failure of the early model of this ligament to perform this function was seen as the bones of these joints (namely the cuboid) passed through the long plantar ligament array (recalling that the tension only arrays do not interact at all with the bony anatomy except at the origins and insertions).

The plantar fascia experiences a different kind of wrapping. Instead of a close proximity to bone as seen with the long plantar ligament, the plantar fascia experiences significant flaring of its three dimensional shape as it passes the midfoot level. As previously described, the thick structure originating from just under the lip of the anterior aspect of the inferior calcaneal tuberosity broadens and thins as it passes the midfoot level. Nearing the forefoot, this structure flares significantly in the transverse plane to send separate bands of fascia to each ray of the foot. This morphological change is the most significant for a single ligament in the structure of the foot and poses an additional challenge in capturing its anatomy.

The following methods describe how these structures were modeled to account for their 3D peculiarities thus allowing the design of the structure to act on their bones as intended.

Long Plantar Ligament

Small 1mm beads were created in SolidWorks to insert into the mid-substance of these ligaments. The beads gave their ligament arrays greater 3D solid reaction and contact with nearby bony anatomy. These beads were originally football shaped with a vertex on each end. An individual array element in the long plantar ligament would be broken into two tension only

elements. The proximal element would retain the original elements proximal insertion, but attach distally to one of the points of the football shaped bead. The distal element would attach proximally to the other vertex of the bead, and distally to the insertion of the original element. The length-tension equation describing the elements would be duplicated from the original element, and updated to reflect the new length of the shorter dual elements. This length would also serve to promote the bead coming to "rest" in its designed position; these positions were chosen based on where the greatest penetration of the original elements into the bony structure occurred, thus preventing most of this penetration. These beads were added to the 3D contact definitions in COSMOSMotion to allow them to interact as solid objects with the bony anatomy (Figure 3.35). Such interaction enhances the "wrapping" behavior of long ligaments around bony geometry.

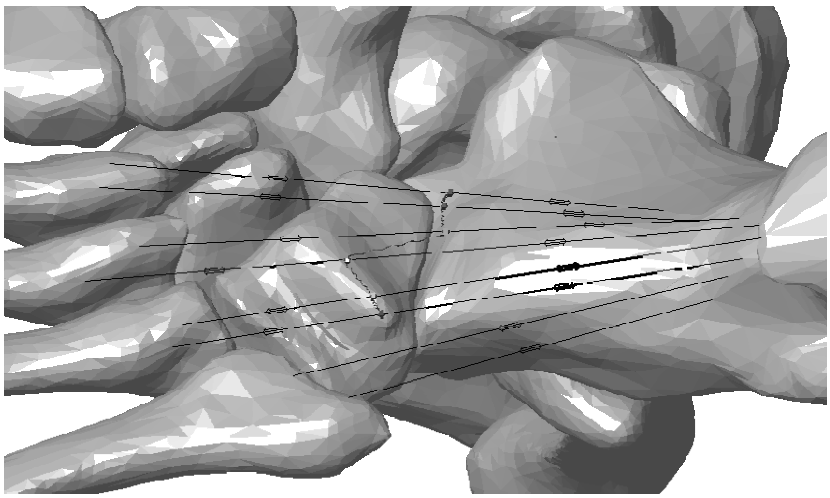

Figure 3.35: Long Plantar Ligament with Beads. Proximal and distal portions of the long plantar ligament are separated by bead solid geometry. Linking springs (discussed below) join portions of the array (arrows).

Early performance of these bead elements was unsatisfactory. The elements would ricochet wildly under the arch of the foot, spinning in all three direction and freezing simulations before their position and orientation ever began to equilibrate. To account for this, a motion restriction was applied to the elements to prevent their 3D rotation. The ends of the football shaped beads would always point towards the origins and insertions of their respective array elements. Performance was still undesirable as the beads would bounce in a jump rope fashion curving back and forth independently of each other, at their design length. The beads were linked with spring elements to simulate the connected sheet behavior of a ligament and maintain appropriate orientation (i.e. prevent the ligament from twisting over on itself). The beads excessive bouncing, rotation and crossing translation were now stilled but simulations continued to fail. The beads would hold true to the surface of the bone, essentially "wrapping" the surface for 20-30 frames of simulation, but would-without fail-suddenly fall through the bone and pop out the other side. This behavior was reminiscent of early failure where the entire foot would all through the floor plate and disappear into simulation space, but was found to be of different causes. Using simplified assemblies of one bone (cuboid) and a single bead, one such ligament element chain was recreated for rapid and repeated testing. Through trial and error, it was discovered that when a revolved feature is used to make a bead (such as was done with the football shaped beads) the 3D contact would simply stop working after several frames of contact. But when an extrude feature (such as a simple square) was used, the 3D contact took and held through the entire simulation. This seemed to be a unique reaction of these two methods of 3D featuring to .stl generated solid bodies. The football shaped beads were modified with a small mid-substance addition of a square extrude feature. This feature prevented the pass through failure immediately (Figure 3.36, left). These beads wrapped bony anatomy and lent the tension

in the long plantar ligament as aid in preventing inferior movement of the tarsal bones they covered (Figure 3.36, right).

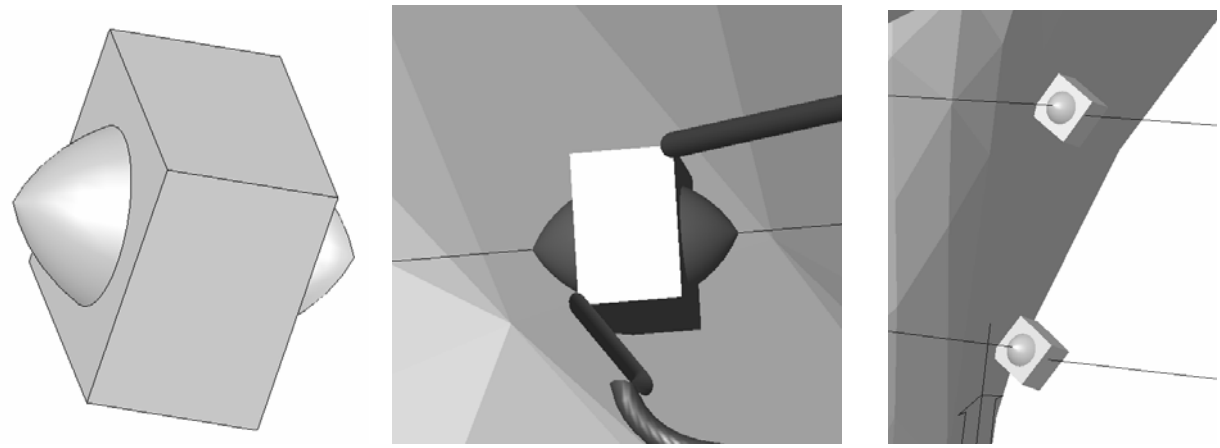

Figure 3.36: Long Plantar Ligament Beads. Final bead alone, left; bead *in situ* with ligament elements attaching to football shaped ends, and restraining springs on cubic body, center; beads during simulation preventing long plantar portions from penetrating the cuboid, right.

Plantar Fascia

The plantar fascia was added in these later models. The geometry and function of this tissue was found, early on, to be complex across this anatomy. To further investigate this, in house dissection and literature[42] suggest that the portion of the fascia inserting in the 2nd and 3rd rays exhibits a marginally more robust tissue bulk. As a result, the 200 N/mm stiffness of the plantar fascia (Chapter 2) was divided in the model to give the medial zone (1st ray) of the ligament a stiffness of 60 N/mm, each branch of the middle zone (2nd and 3rd rays) a stiffness of 50 N/mm, and each of the remaining thin portions of the lateral zone (4th and 5th rays) a stiffness of 20 N/mm.

To account for the mentioned 3D anatomy a similar method of using a SolidWorks intermediate structure, as was used for the long plantar ligament, was devised here. A "ligament tie" was created as a single part. This narrow, saw tooth extrude was equipped with plentiful

vertices to tie into the plantar fascia (Figure 3.37). Like was done with the long plantar ligament, the individual array elements of the fascia were divided into a proximal and distal portion to incorporate the ligament tie. The element length-tension definitions were updated to reflect the change and to account for the dimensions of the ligament tie.

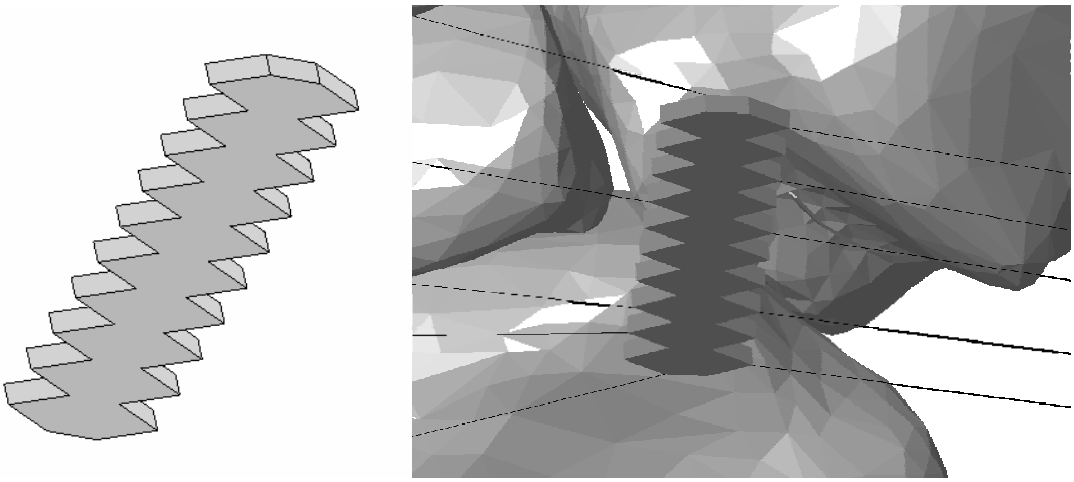

Figure 3.37: Plantar Fascia, Ligament Tie. 3D tie solid body, built with numerous vertices to promote close description of the plantar fascia, left. The tie is shown in place in the model with proximal and distal plantar fascia array elements attached, right.

A point was chosen from each the first metatarsal, fifth metatarsal, and calcaneus. These points were selected as where the center of the portion of the plantar fascia would insert on that bone. These three points were references for a plane which the flat bottom of the ligament tie was mated to. The end effect is that the tie is free to rotate in the transverse plane along its line of action, but not the coronal or sagittal. The allowance of transverse motion is important here to allow the medial and lateral portions of the plantar fascia to each reach their own equilibrium. The locations of this ligament tie in the plantar fascia was selected to correspond to the anatomical level that this structure sees its conversion from a single thick band to flared segments, just before the forefoot. The distal insertions of the plantar fascia were on the

metatarsal heads. The structure naturally inserts on the proximal phalanges but as the phalanges are fused in the model this was redundant and simplified (Figure 3.38).

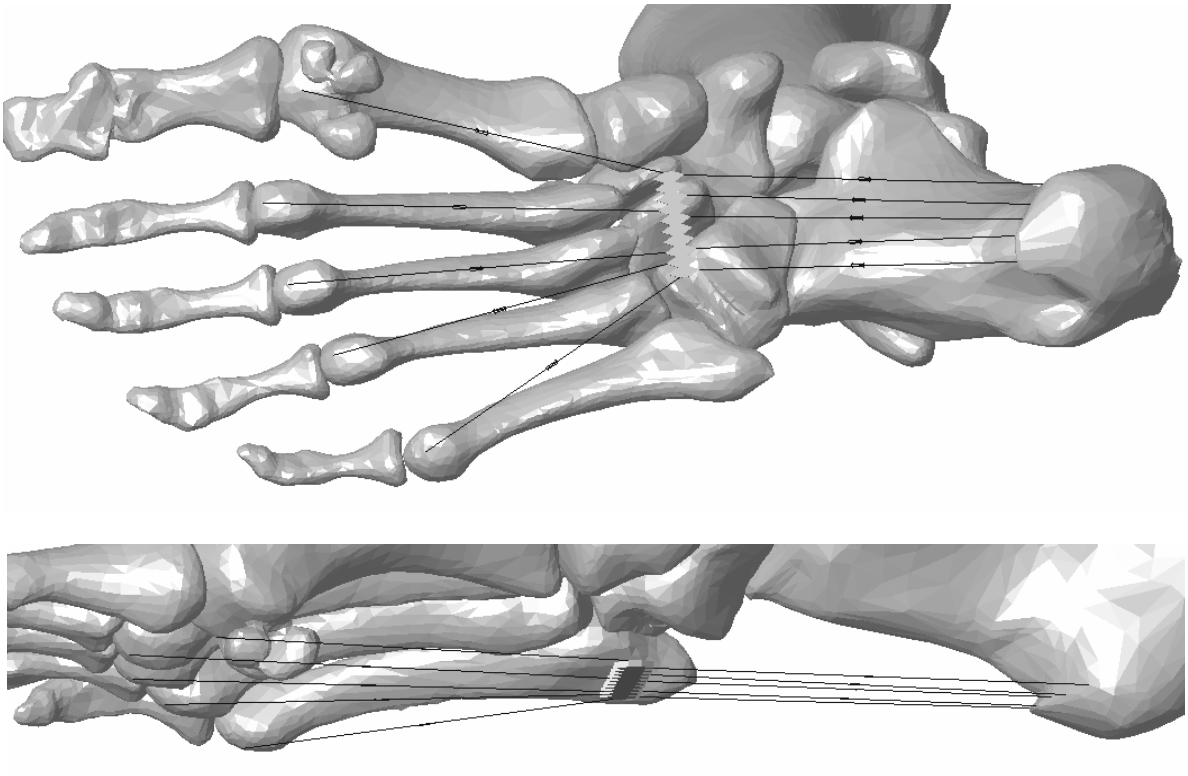

Figure 3.38: The Plantar Fascia, with Ligament Tie. Views of the modeled plantar fascia with ligament tie solid. The anatomy of the plantar fascia changing as it passes the midfoot level and flares to the forefoot was modeled with ligament tie, top – inferior view. This structure is also seen with a lateral view of the origin of the fascia on the inferior lip of the posterior calcaneal tuberosity, bottom.

This method of controlling the ligament tie was chosen over the method used for the long plantar ligament both because the geometry of the plantar fascia is very two dimensional and the extreme length of the plantar fascia described as proximal and distal segments caused great increases in computation time when modeled with separate beads.

Achilles tendon

The Achilles tendon was modeled using four action reaction elements in an array. The origin of the array was a common point on the proximal load fixture. The insertion of the array is along the broad superior ridgeline of the calcaneal tuberosity (Figure 3.39).

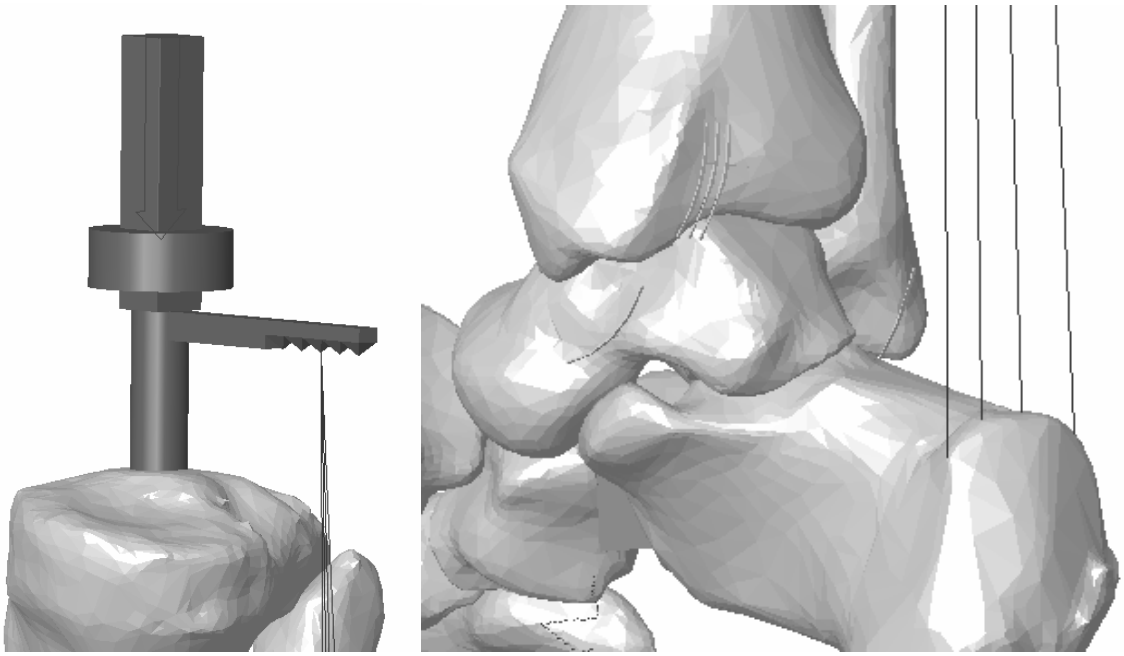

Figure 3.39: Achilles tendon.

Ligament Function Definition Spreadsheet

As the aforementioned ligament structures were enhanced by using more extensive arrays, and with modeling structures (such as the plantar fascia) that were not accounted for before, the ligament function definitions rapidly became unmanageable (in terms of updating/editing). To ease the difficulty of future edits, the function definitions were programmed into an excel spreadsheet to allow them to be rapidly updated and to reduce error.

[**NOTE**: the definitions still require manual transfer via copy/paste to COSMOSMotion; this is a labor intense step.] The spreadsheet contains columns for ligament name, stiffness, length and marker numbers. The spreadsheet was used to create two additional quantities: an *in situ* strain calculation from the design length and an assembly of these individual columns into a single cell that could be copied and pasted as the whole ligament function equation. To combine these cells, the Excel "concatenate" expression was used (Equation 3.5) to yield the same equation as was described previously with Equation 3.1.

```
=CONCATENATE("IF(DM(",$I37,",",$J37,")-",(E37*0.96),":","0,0,-
",$B37,"*(DM(",$I37,",",$J37,")-",(E37*0.96),")-0.1*VR(",$I37,",",$J37,"))")
```

Equation 3.5: Concatenation of Spreadsheet Terms. This form was used to create the output function equation. I37 and J37 are the reference to marker number cells, E37 is the design length of the ligament element, and B37 is the stiffness of the element. Quotation marks enclose and separate text from equation.

Iterative Strain Tensioning

In the last series of early models, where tension only elements were first used, it quickly became apparent that when a 2% strain was applied to the *design* length of the ligament elements that the strain was lost in the settling motion of the simulation in the very first frames of simulation. In nearly all cases the *settled* length was shorter than the *design* length. Measurement verified that few if any of the ligaments were actually under 2% *in situ* strain at the start of body weight application.

With this discovery was also the recognition of the ankle ligament's neutral elongation data reported by Nigg et al.[35], as well as consideration of further studies on *in situ* strains present

in various joints[36-41]. Consideration of these studies led to the decision to increase *in situ* strains from 2% to the 4% average range reported in that study, remembering that 4% was the average reported *in situ* strain in that study. To obtain settled ligaments under 4% *in situ* strain a series of simulations were run. After each simulation the *settled* length of all the ligaments were recorded and compared to the *design* length. The *settled* lengths of the simulation were input as *design* lengths for the next simulation. This process was repeated until the difference between *design* and *settled* lengths were minimized. By performing this calibration process a model was developed where all ligaments were expressed under the 4% *in situ* tension.

Bone Scaling

The process of iteratively measuring each of the 144 ligament elements displacement during simulation to find their settled length was very involved. A displacement plot for each ligament was created to distill a settled value into the excel database. The new equation for the ligament element which took into account this updated settled length, was copied into the function expression for that element. This process took ~45 seconds for each of the 144 ligaments and was required three times to reach acceptable model equilibrium.

The root of this problem stemmed from the gaps between the articular surfaces of the bones. This gap is due to the CT scans inability to differentiate articular cartilage. To reduce the extensive iterative work required to obtain the desired *in situ* strain as well as the user error associated with performing such a task, another method was devised to take the cartilage gaps into account. By performing a scaling feature in SolidWorks on the bone part files, these gaps could be reduced. The concept was that the application of only a small scaling factor would be necessary to reduce the near millimeter gaps between the bony anatomies. There was a desire to avoid assigning each bone its own scaling factor, and instead blanket the model with 1 effective

scaling factor. A concern identified early on was that the long bones, the tibia and fibula (as they exhibited dimensions an order of magnitude greater than the other bones), would experience very different dimensional changes in reaction to the scaling factor as compared to any of the much smaller bones of the foot. A compromise was reached where 2 scaling factors would be used in the model, one for the long bones and one for the small bones (Table 3.5).

Bone	Scaling Factor
Tibia	0.5%
Fibula	0.5%
Talus	2.0%
Calcaneus	2.0%
Navicular	2.0%
Cuboid	2.0%
Cuneiforms	2.0%
Metatarsals	2.0%
Phalanges	2.0%

Table 3.5: Bony Scaling Factors. Factors used in the "scale" feature of SolidWorks to modify the leg, hind-, mid- and forefoot.

As they constituted the majority of the bones and articulations the tarsals, metatarsals, and phalanges were scaled, as individual parts, by $1/4^{th}$ a percent size at a time. Each time they were scaled the assembly was reopened and a interference check was performed at several joints. This check was ensuring that the scaling was not excessive enough to create large interference between bones in the neutral position. At a +2% scaling factor the joints of the hindfoot, midfoot, and forefoot just began to touch with sub cubic millimeter overlap. This scaling factor was kept. The same process was applied to the long bones, and monitored at the tibiotalar and fibulotalar articulations as these articulations were at the end of the long bones they would experience the greatest change in dimension. At +0.5% scaling factor the subtalar joint just began to touch, again at sub cubic millimeter levels (Figure 3.40, Figure 3.41). The scaling

closed a visible amount of the gapping between bones (Figure 3.42). The application of these scaling factors to the bones required only one iteration of the ligament settling and adjusting process to achieve 4% *in situ* strain, most of the correction was due to the changed design length of the structures from the scaled growth-very little actually bony settling occurred after the scaling.

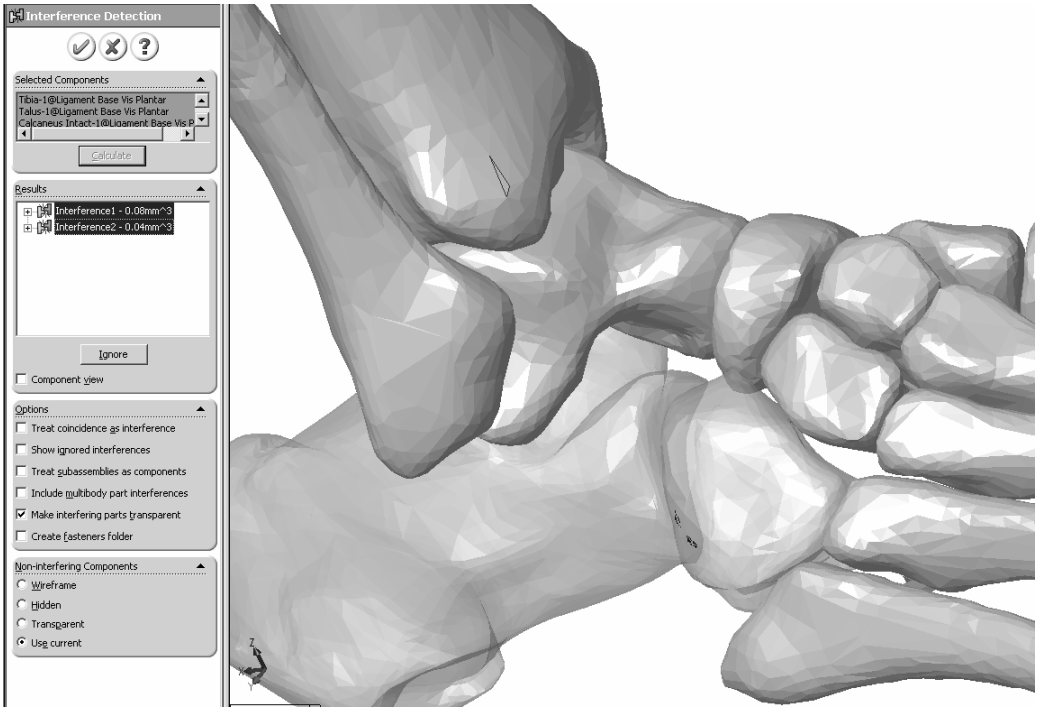

Figure 3.40: Example of Interference Check between Scaled Bones. Interference detection window opened and detection performed for several bony surfaces. Checked here are interferences between the tibia, fibula, talus, calcaneus, cuboid and navicular. With the scaling factors applied via Table 3.5 only two small bony contacts are made, each with less than 0.1mm^3 of volume associated with it.

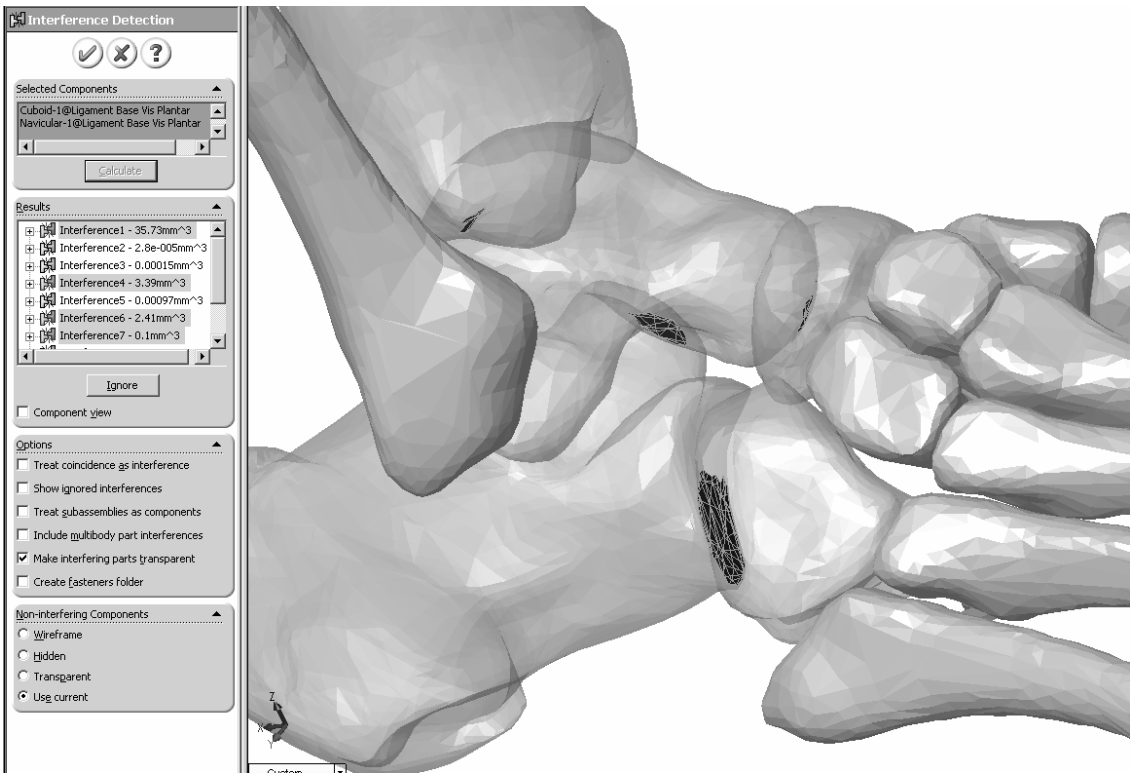

Figure 3.41: Overscaling of Bones. Interference detection window with multiple new interferences calculated. Example showing the effect of 3.0% (1% larger than what was selected) increase to just the talus, calcaneus, cuboid and navicular. Large volumes of interferences are introduced, 37.5mm^3 at the calcaneocuboid joint and > 1mm^3 interferences elsewhere.

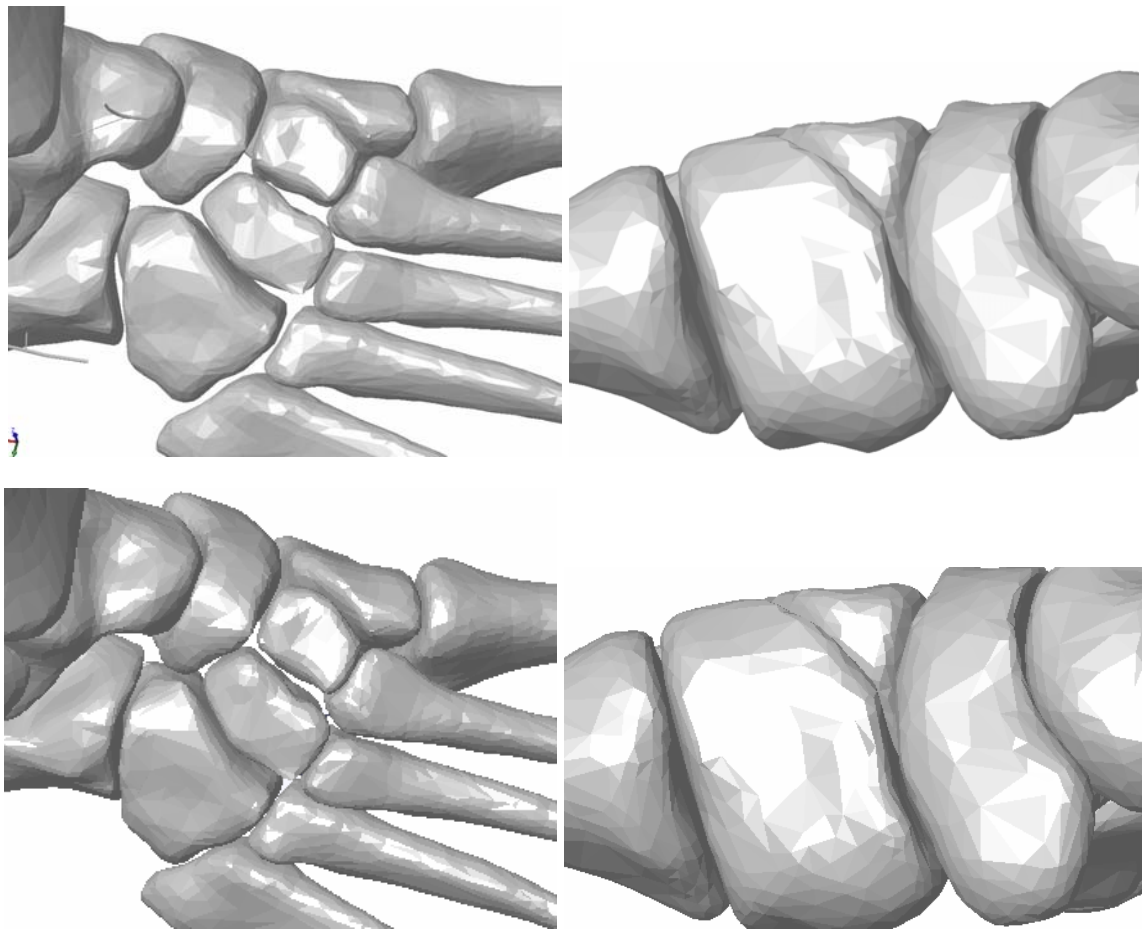

Figure 3.42: Bone Gap Closure Images. Midfoot viewed from an oblique superior, left; and of the medial midfoot, right. Images are of un-scaled original scan bone, top; and with scaling scheme applied for gap closure, bottom. Note gap closure depending on bone size and gap size.

The prior several sub sections discuss the final form of the function expressions which were developed from the re-addressed anatomy, ligament wrapping, iterative straining, and bone scaling; a complete example of these expression spreadsheets can be found in Appendix II

Simulation Rapidity and Stability

By allowing a simulation to run with no significant external loads [**NOTE**: it was found useful to have a constant 10N downward axial load applied in all simulations, this prevented the

model from literally floating away into simulation space before external loads are applied] for several frames a *settled* length would be reached in the ligaments.

Computational time for the early simulations of the entire foot could easily take 2-3 hours. As the models complexity increased with greater detail for ligament arrays and the addition of beads and ligament tie to describe this anatomy, the simulation time could draw out by another few hours or even require overnight processing. Additionally, there were a class of simulation failures that appeared (to one not well versed in the source code of SolidWorks and COSMOSMotion algorithms) to be random. An unchanged assembly could be simulated several times and experience a spontaneous simulation failure 30-60% of the time. The estimated cause of these failures was thought to likely be an inability of the solver to find a convergent solution to a 3D contact or resolution of a ligament load/elongation (particularly in the case of the beaded ligaments which still have greater 3D movement available than any other ligament). In an effort to address both of these issues, several alterations were made to the default choice of simulation parameters.

The geometric accuracy was changed from "use exact geometry" to 100% geometric accuracy on the slider-bar. This was first tested on a simple construct which included a talus allowed one degree of translation and rotation about the axis of translation, which was move into contact with a fixed talus. This simple two bone system required 10 minutes of solver time to finish with the "use exact geometry" option chosen. When this option was unselected and the accuracy slider bar was moved to 100% the solver time dropped to 10 seconds. The motion and contact of the two talar tests were compared and found to be near identical. This single change in simulation parameters brought solver time down from 4-5 hours to 15-45 minutes, still orders of magnitude longer than the 10 second talar experiment, but a vast improvement from 5+ hours.

In the solver parameters tab, two changes were made. The first was a decrease in the accuracy value from 0.0001 to 0.01. The accuracy value considers how the solver determines if a time step has reached convergence in order to move to the next time step. Smaller numbers are listed as being more "accurate". The exact computational change this imparted at the solver level is largely unknown (again a lack of source code and very limited description in help files and online documentation) but in similar small talar tests there were no apparent changes in performance or the results of measured data.

The second change made here was an decrease in minimum step size from 1e-8 to 1e-9 (the smallest step size possible in COSMOSMotion). This allows the solver to break the time steps down further in areas it has trouble reaching convergence. Both of these changes significantly reduced the rate of sudden simulation failure and program freeze. The accuracy reduction potentially loosened restrictions that prevented the solver from advancing to the next frame. The time step size decrease reduced the number of 1st frame failures and failures during the application of load, both of which suddenly perturb the system. The GSTIFF integrator method was kept as a compromise between handling oscillation and describing 3D movement and intermittent contact.

A final series of changes was made in the 3D contact parameters. These changes were in reflection of two problem areas. The simulation failure wherein the foot lost 3D contact with the floor plate and fell into simulation space was one such area. The second was simulation failure caused by sudden spikes in contact force (which were responsible for rapidly and violently displacing the bony anatomy from itself) which would fail the simulation also at the 1st frame or during applications of load, with some instances during settling periods. The parameter of contact stiffness was reduced from 1000 N/mm to 800 N/mm, the penetration distance for

dampening was 0.1mm and the dampening coefficient itself was increased from 50N•sec/mm to 100N•sec/mm . These were not in an effort to approximate any cartilage contact, but instead to reduce and soften the contact between bony anatomies. It was estimated that, sometimes, the beginnings of a bony contact or the rotation of that contact which led to less surface area/volume for contact would create sudden load spikes which would drive the bones away from each other. Whether this was the case, these changes did remarkably reduce the occurrence of simulation failure at those specific times. And the model has not passed through the floor plate since.

3.12 Final Refinements: Failure Modes

Preliminary simulations of the in-house scanned model had a slightly lower failure rate than the earlier models. With the improvement in modeling technique, anatomical description (for constraint of bony anatomy), and the various performance addressing investigations the failure rate has steadily dropped from early rates of near 70% to current rates that are 5% at most. The most common source of failure currently is when a new osteotomy or other minor change (such as a mate, joint, tension only element expression update or 3D contact - not a widespread model alteration) is incorrectly defined in COSMOSMotion. The 5% failure rate of these established models is almost exclusively a failure in the first 10-20 frames of simulation and is thought to be due to the development of an unchecked bony or ligament oscillation. With the addition of the proximal tibiofibular articulation ligament arrays the models were no longer plagued with random occurrences of violent proximal dislocation of these bones and the associated simulation failure due to an oscillating fibula. Ligament wrapping, as described, also reduced computation time and failure rate.

3.13 Final Refinements: Model Performance

With the development and performance of the models ability to simulate a loaded stance documented and repeatable, validation of the results of this model to clinical and experimental findings is discussed in the upcoming chapters.

Chapter 4 - Arch Stability Study

4.1 Introduction

While the whole of the ligament structure of the foot is important to mobility, stability, and function, the plantar structures are some of the most vulnerable to overuse and injury[47]. As described in Chapter 2, the anatomical architecture of these soft tissue structures is critical to arch stability by the role they play in resisting the elongation of the foot and therefore the collapse of the bony arch under load[32,48,49]. Traumatic damage or overuse leading to chronic degradation of these structures can cause a variety of symptoms and injuries such as heel pain, plantar fasciitis and pes planus. Unrelieved, these can lead to severe functional deficits over time[50-54]. The structures of the medial arch play a particularly important role in arch stability and have been the focus of much research encompassing both tissue disease and surgical intervention. Three major ligaments contribute strongly to plantar arch stability: the spring ligament, the long and short plantar ligaments (referred to collectively here out as the plantar ligament), and the plantar fascia. Various experimental studies have been performed to isolate and elucidate the role these structures play, some of which were incorporated in the design of this computational model[55-62].

Two studies on arch stability and soft tissue behavior were considered for early validation of this model. Huang et al investigated arch height and overall arch stiffness under varying ligament transection combinations and varying axial compressive loads in a cadaver model to determine the relative contributions of each structure with respect to the intact foot[59]. Crary et al experimentally loaded cadaver feet in a similar manner while investigating the effect of plantar

fascia release on the strain in the spring and long plantar ligament[57]. Strain gauges were attached to these ligaments along their bulk fiber direction to record unloaded and loaded lengths before and after fascia release, further details of the recreation of these studies is described below.

4.2 Materials and Methods

Modeling Arch Stability

The first validation focused on simulating the experimental cadaveric study performed to investigate the contribution of plantar soft tissue structures to arch stability. As done experimentally, an axial load of 690N was applied to the load fixture on the proximal tibia during simulation[59]. Arch height was calculated in the experimental study as the vertical distance between a Kirschner wire placed in the talar neck and the platform the foot rested on, as measured by a potentiometer. Arch height was measured in the computational model by marking a point on the talar neck and a point on the foot platform in the medial view, and tracking the vertical displacement between these points over the duration of simulation (Figure 4.1).

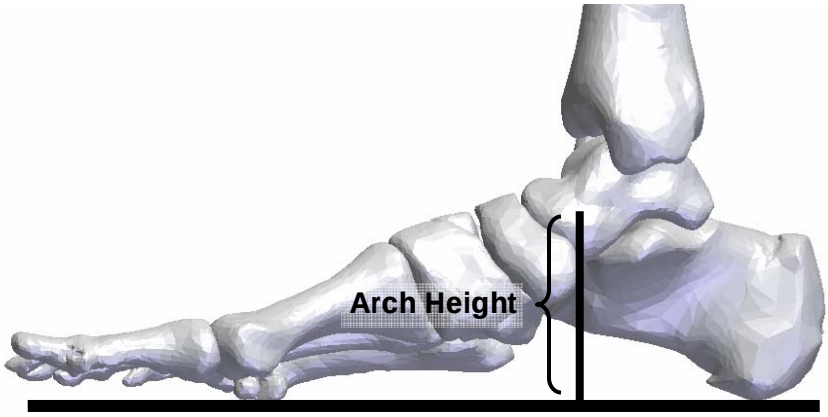

Figure 4.1: Height Measurement Method. The point of application in the talar neck as described in Huang et al. is located at the center of the talar neck cross section when viewed medially. This was recreated by choosing the center of a triangulated surface that was located in

the middle of the neck in this perspective. For all models this exact surface was the same point of measure. The same was true of the point on the ground plate.

To simulate sequential release of structures, entire ligament arrays were suppressed from action in corresponding to the variation of sectioning those ligaments in the experimental study. The suppressing of an element from simulation effectively removes its interaction in any way with the simulation. These modeled combinations were: intact, single structure suppressed states, dual structure suppressed states, and all structures suppressed. The contribution to arch stability is based on the ratio of one structure's additional displacement to the total displacement created in the absence of the three plantar structures[59] (Equation 4.1). This measure was described in Huang et al as a method of comparing these structures.

$$\text{Percent Contribution} = (S_{ad}) / (SP_{ad} + PL_{ad} + PF_{ad}) * 100$$

Equation 4.1: Percent Contribution. Where S_{ad} is the selected structures additional displacement from intact; SP, PL, and PF terms are the additional displacements of each the spring ligament, plantar ligament, and plantar fascia. Additional displacements are calculated by subtracting the difference between the end height of the cut state and that of the intact foot.

Modeling Fascia Release

The second validation recreated the experimental cadaveric study to investigate the strain present in plantar structures of loaded cadaver feet before and after plantar fascia release. As done experimentally, an axial load of 920N was applied to the load fixture on the proximal tibia[57]. In the literature, strain was measured over a portion of the bulk fiber direction of the spring and plantar ligaments. The study states in text,

> "One DVRT strain gauge … was placed on the plantar medial aspect of the spring ligament just proximal to its insertion into the navicular" and "A second DVRT … was placed on the medial side of the long plantar ligament overlying the calcaneocuboid joint. Gauges were oriented parallel to the major longitudinal bundles of the ligaments being tested."

To mimic the anatomical choices made experimentally to measure strain, the portions of the computational arrays that represented the common fiber direction of the spring and plantar ligaments at the locations selected in literature were averaged to yield total ligament elongation (Figure 4.2); however, unlike the experimental study, the strains over the entire origin and insertion, as opposed to a 5-6mm region[57], were measured. Simulations were run on both the intact structure and with the plantar fascia suppressed from simulation.

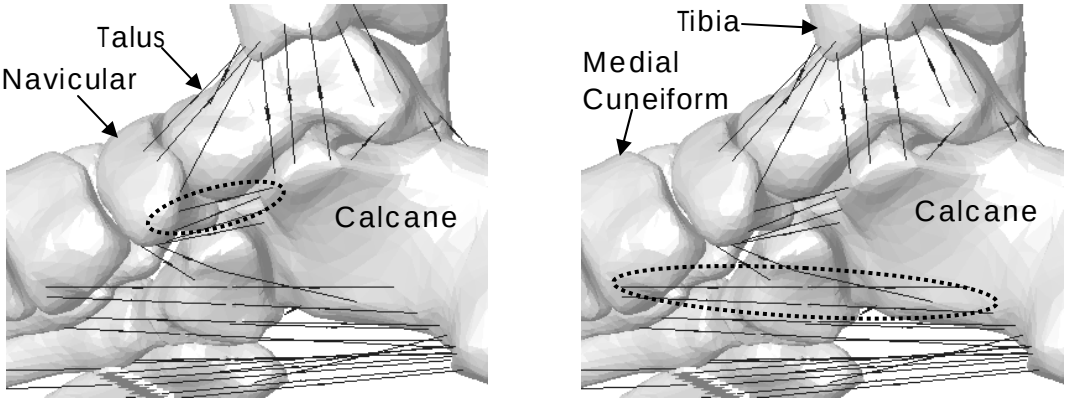

Figure 4.2: Plantar Strain Measurement Sites. The portions of the modeled spring ligament anatomy described in Crary et al[57] as a placement site for strain measurement, left; and the portions of the modeled plantar ligament chosen for strain measurement, right. These structures were tracked in simulation for determination of model predicted strain in these tissues. Visible also are ligament arrays of the medial ankle, other structure hidden for clarity.

Model Sensitivity

As mentioned in Chapter 3, the range of *in situ* strains reported by Nigg et al[35] (2% - 6% *in situ* strain) was determined for only a selected group of the more mobile ankle joint ligaments. Additionally, reported ligament stiffness values have a large range[31,42]. To explore how the range of reported global *in situ* strain and ligament stiffness values would affect model outcome, two sequences of additional simulations were performed on the computational model that mimicked the experimental setup of Huang et al[59]. Simulations of global ligament in situ strains of 2%, 4%, and 6% - encompassing the range found by Nigg et al[35] - were performed. The second sensitivity tests were modifications of ligament stiffness. Siegel et al[31] reported stiffness values for major ankle ligaments that had an average standard deviation of ±43% while Kitaoka et al[42] reported values for plantar fascia stiffness with a standard deviation of ±35%. These sequences were created by editing the versions of the master spreadsheet to update the function expression for all structures. These expressions were then applied to a series of simulations and behavior was noted.

4.3 Results

Arch Stability

The displacement of the arch, (drop in talar neck height when loaded), was used as a measure of arch stability experimentally[59]. In the computational model, the measured arch height of the intact foot decreased by 6.46mm as a simulated body load of 690N was applied. In subsequent simulations, each plantar ligament deficient state exhibited a greater displacement of the arch than the intact state (Figure 4.3). In the single structure deficient states, the spring ligament's removal led to a 6.83mm arch displacement. The plantar ligament's removal had a

greater impact of 7.04mm, followed by the plantar fascia, which had the greatest displacement with 10.18mm of arch deformation.

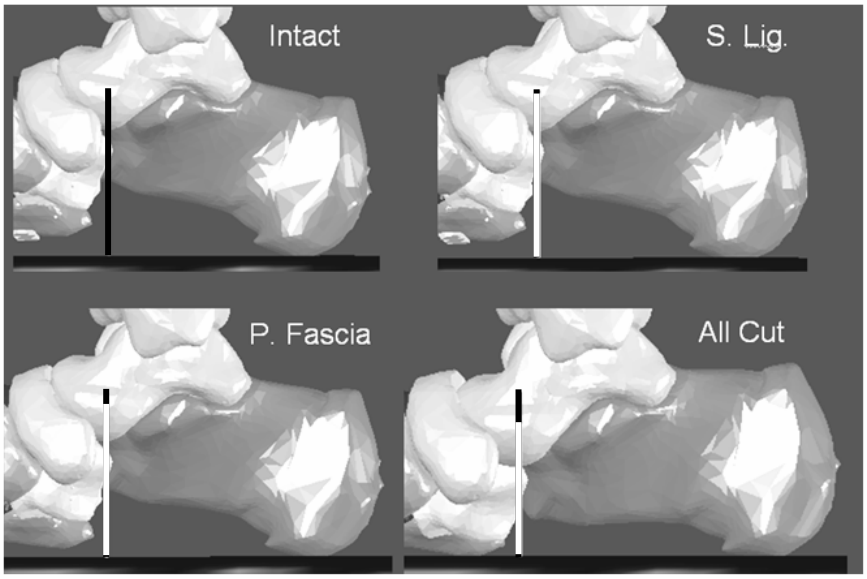

Figure 4.3: Selected Changes in Arch Height. Arch height changes in a loaded intact specimen (upper left); with suppression of the spring ligament (upper right); plantar fascia (lower left), and all three plantar structures (lower right). Note measurement of mid-talar neck to ground superimposed over the intact distance, denoted by black line, and orientation of calcaneus during successively weakened arch simulations.

For dual structure deficient states: the arch displayed the greatest displacement when only the spring ligament remained, 16.27mm; was more stable when only the plantar ligament remained, 12.14mm; and most stable when only the plantar fascia remained, 7.18mm. The simulation of all three of these structures deficient exhibited the greatest displacement of the arch, 19.11mm. In this simulation, enough displacement was generated to allow the base of the fifth metatarsal to begin engaging the floor plate at the point of maximum load. This arch collapse was reported in the literature under 920N axial loading for the all structures transected

in the experimental setting. The relative contribution of these structures to arch stability followed trends seen experimentally[59] (Figure 4.4).

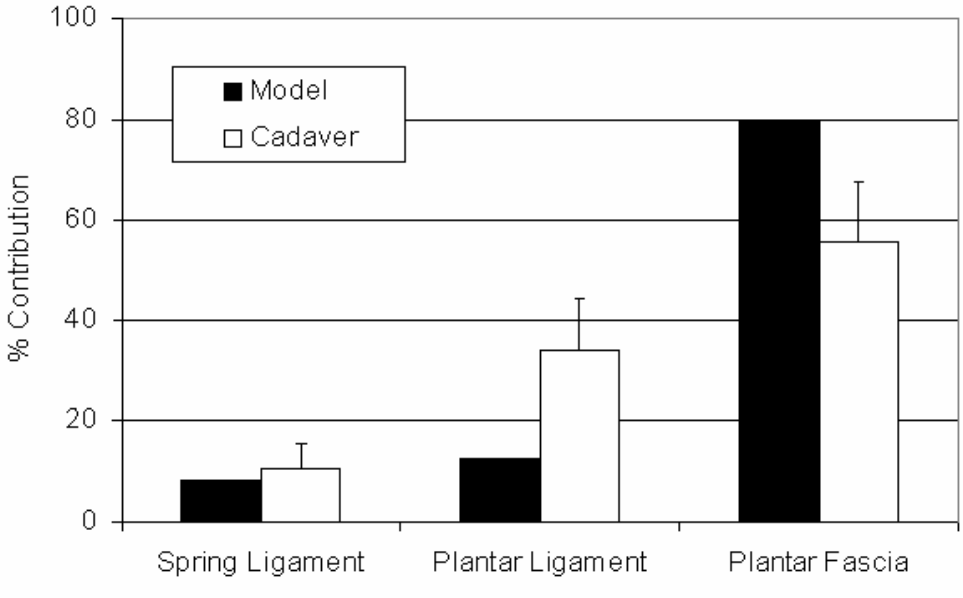

Figure 4.4: Contribution to Arch Height. This plot is the comparison between relative contributions of the three plantar structures to arch stability as seen in the computational model and experimental cadaver study. As discussed in Equation 4.1 this was calculated as the ratio of that deficient state's displacement to the total displacement created in the absence of all three plantar structures[59].

Fascia Release

In the intact model, with a baseline of 2% *in situ* strain in all ligament tissues, the spring ligament demonstrated an average additional strain of 1.51% when loaded to 920N. The model plantar ligament demonstrated an average additional loaded strain of 1.61%. With the plantar fascia suppressed from simulation, the spring ligament's additional strain rose to 3.02% under loading and the plantar ligament's additional strain rose to 4.89% under loading (Figure 4.5). Of note also with the removal of the plantar fascia in the model, the resting strain of the spring and

plantar ligaments increased, respectively, by an additional 0.1% and 0.5% from their 2% *in situ* baseline. The conditioned ligaments in the experimental study increased in strain by 0.7% for the spring and 0.8% for the plantar ligament[57]. In both the computational model and in the reported literature, the plantar ligament's increase in loaded strain between states (intact and plantar fascia release) was double that of the spring ligaments increase in strain[57].

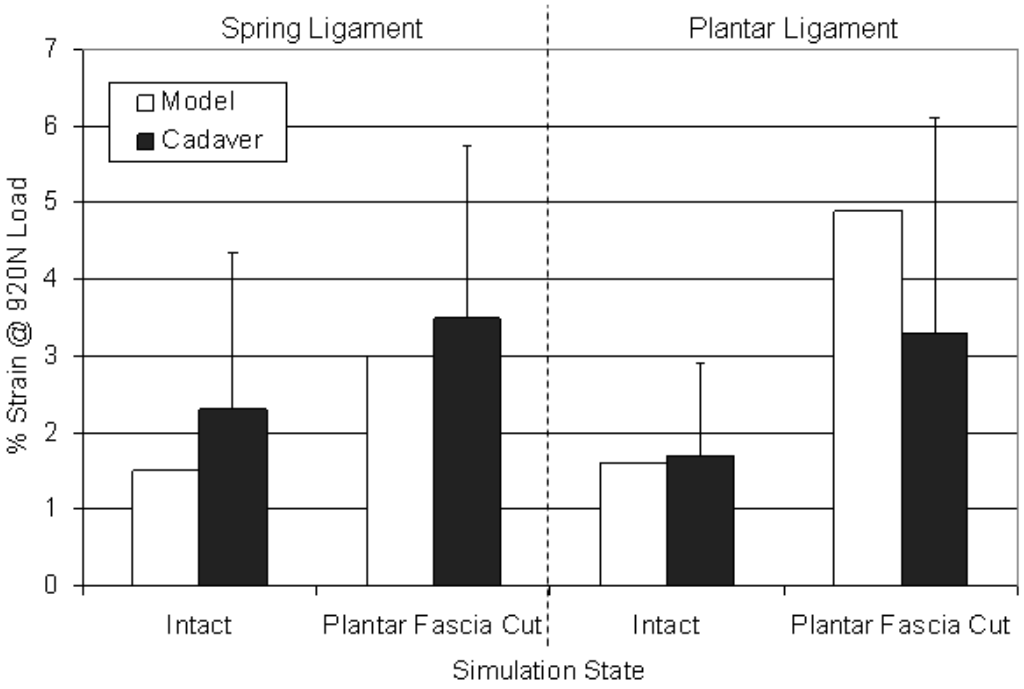

Figure 4.5: Tissue Strain Following Fascia Release. Strain response of the spring ligament and plantar ligament in the intact state and after plantar fascia was removed, under 920N axial compressive loading. In both the computational model and experimental study, the increase in strain in the plantar ligament was double the increase seen in the spring ligament[57].

Load Sharing Measurements

While not a measure made in either study, one of the benefits of this computational modeling technique is the ease by which both elongation and load data can be collected from the

ligament arrays. Measurements of load present in the plantar structures after one of the structures was transected were thus readily available from the computational model (Figure 4.6). For all the various transection states, the maximum load present in the plantar fascia was ~380N, the maximum for the plantar ligament was almost 600N, and the maximum for the spring ligament was 258N.

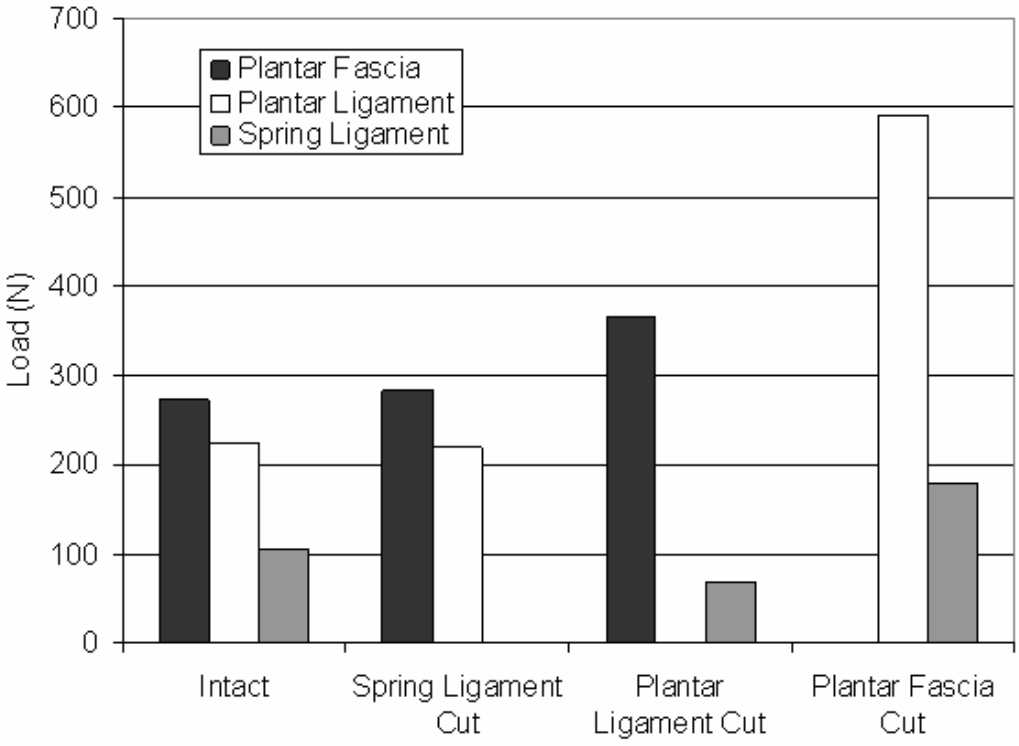

Figure 4.6: Plantar Tissue Loads. Load present in the three plantar structures at different simulation states. Load magnitude appears as zero when the structure is in its transected simulation state. Note the apparent priority of the plantar fascia in the different states.

Sensitivity Tests

In situ strain: The results of the sensitivity tests varying global *in situ* strain from 2% to 4% and then 6% affected the contribution of all structures. The spring ligament experienced a continuous decrease from 8.0% at 2% strain, to 0.9% at 6% strain. The plantar ligaments

contribution increased from 12.5% to 18.7% across the same range, with a greater jump between 4% and 6%. The plantar fascia fluctuated, starting at 79.5% at 2%, peaking at 84.4% contribution at 4%, and dropping to 80.3% contribution at 6% global strain, which corresponded to the interplay between the spring and plantar ligaments at 4% (Figure 4.7).

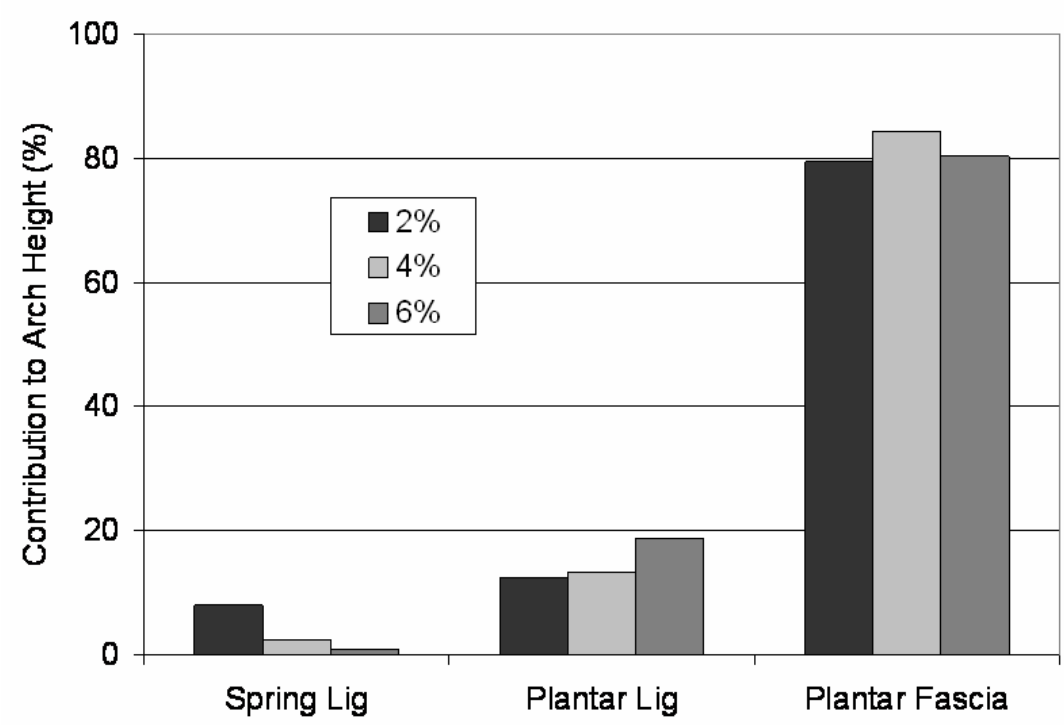

Figure 4.7: Global *in situ* Strain Sensitivity. Arch height contribution of single structures (spring ligament, plantar ligament, and plantar fascia) for sensitivity tests of 2%, 4%, and 6% global *in situ* strain.

Ligament stiffness: The second set of simulations varied the stiffness of the ankle ligaments by reported standard deviations for the bulk of the soft tissue (±43%[31]). and plantar fascia (±35%[42]). For test simulations a standard deviation less than the average value, the spring ligament was recorded with a higher contribution of 3.9%; at average and increased global stiffness, the spring ligament dropped to 2.4% and 0% contribution respectively. The plantar

ligament fluctuated, starting at 11.8% contribution with less global stiffness, 13.1% at the average, and dropping back to 11.1% at higher global stiffness. The plantar fascia remained somewhat constant at 84.2% and 84.4% for increased and average stiffness respectively, increasing in contribution with higher global stiffness to 88.9% (Figure 4.8).

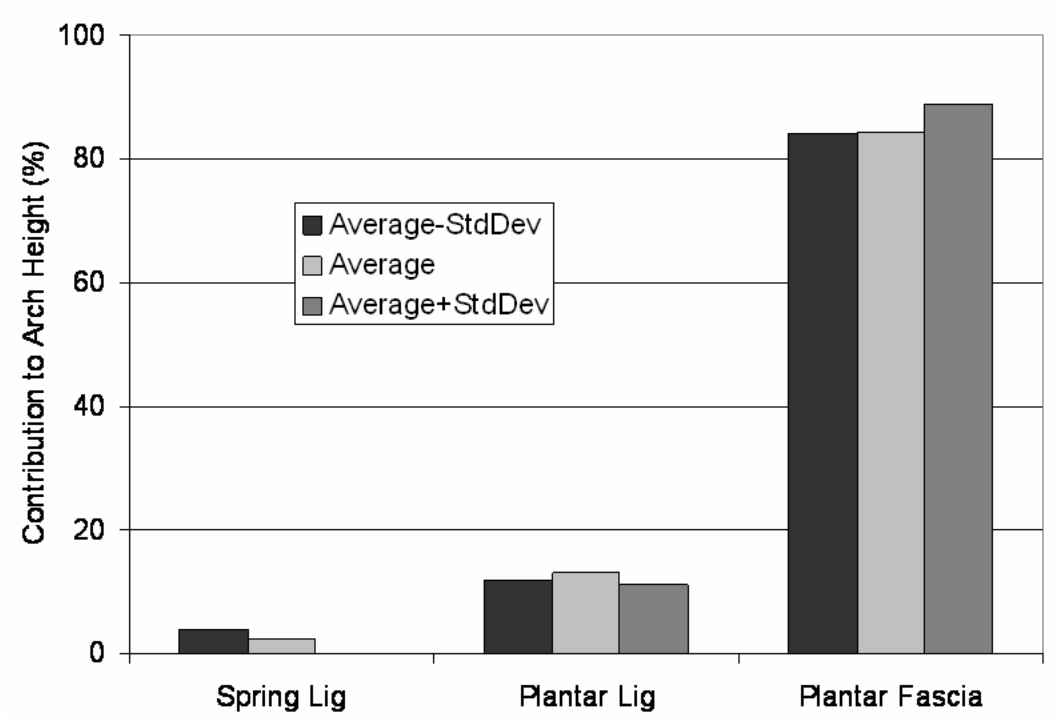

Figure 4.8: Stiffness Sensitivity Results. Arch height contribution of single structures (spring ligament, plantar ligament, and plantar fascia) for sensitivity tests of global stiffness where stiffness values are a standard deviation below and above the average for the plantar fascia (±35%) and remaining ligaments (±43%).

4.4 Discussion

Contribution to Stability: From the arch stability simulation, the order of contribution strength from the plantar structures was shown to be predictive of the response of these tissues in experimental studies. This was seen both in the single structure and dual structure deficient

states; the plantar fascia was always the greatest contributor to arch stability and the spring ligament was always the weakest – which is in agreement with experimental findings.

Ligament Strain: The comparison with the ligament strain study during fascia release also demonstrated the model's robust ability to predict both that the plantar ligament would experience double the increase in strain as the spring ligament, as well as the increase in resting length of these ligaments after fascia release. In the literature, this increase of strain after fascia release both under loading and during rest was attributed to the spring and plantar ligaments taking up intrinsic and extrinsic function, respectively, of the transected plantar fascia.

Sensitivity tests: demonstrated how values within the range of reported ankle ligament *in situ* strains and stiffness can affect the results of a simulation. *In situ* strain deviations across the reported spectrum of 2%-6% minimally influenced the magnitudes of model behavior but did not alter the overall conclusion. Minimal influence was also seen by varying ligament stiffness, which from literature showed a very large standard deviation of 43% for ankle ligaments and 35% for the plantar fascia. While lower stiffness and *in situ* strains allowed greater deformation of the arch under loading, and conversely higher stiffness and strain allowed less deformation, trends in soft tissue structural importance remained unchanged and in agreement with literature.

Literature that investigates the plantar fascia does so in general terms of arch stability and mechanical function, seldom with investigation into how its disease or removal affects deeper plantar structures[32,42,57,62,63]. Experimental work on these plantar structures is confined to indirect measures of contribution[59] and strain over small, superficial portions[57]. The spring ligament, plantar ligament and plantar fascia are three dimensional structures. Each of these structures engages a different group of bones, at different depths in the arch of the foot. This suggests that these plantar structures have an overlapping function and are not affected

independently by the strengths or weakness of their constituents. As these tissues fail, the fewer remaining structures become engaged with a higher load as shown computationally, increasing their propensity to fail as these loads surpass the ultimate strength of the ligament.

Chapter 5 – Simulation of Flatfoot

5.1 Introduction

As with all tissues or system of the body, diseases can afflict at any level of the structure. Of the numerous maladies of the foot, the one chosen as a validation tool for this model was Adult Acquired Flatfoot Deformity (AAFD). AAFD, also known as *pes planus*, and posterior tibial tendon insufficiency (PTTI) is a multi-stage degenerative disease which leads to improper joint alignment causing pain and affecting mobility of the foot and ankle. This disease was chosen due to its extensive prior study both at clinical and experimental levels. Such study has a broad focus in the treatments of this disease. As the disease has affect on multiple joints and structures in the foot, surgical treatment is extensive. Clinical and experimental studies have yielded an expanse of data for comparing these differing methods. While much documentation has been performed about the benefits of these treatments, significant ambiguity remains of the origins of complications related to them.

5.2 Background: Flatfoot and its Treatments

Presentation and Involvement

AAFD is a degenerative disease of the foot with greatest occurrence in ages commonly ranging from the early to mid 40's into the 60's years of age[64-69]. The classification of "degenerative" is given because without treatment both the underlying tissue injury and the abnormal physical morphology continue to exacerbate over time. The exact conditions leading to the onset of AAFD are not fully understood; however, an emergent weakness in the posterior tibial tendon (PTT) is considered to be a key indicator/origin[50,67,70-75]. AAFD is a four stage

disease; stage I is marked by a chronic pain or tenderness along the posterior tibial tendon (PTT) pathway, with no visible foot deformity and correction possible through foot orthotics and rest; by stage II the chronic weakening of the PTT has progressed far enough to start weakening underlying soft tissues, this leads to gross foot deformities that can be observed in the clinic and usually necessitates surgical intervention. The deformities include forefoot abduction, medial arch collapse, external rotation, and hindfoot valgus[67,70,71,76]. At Stage II these deformities are still flexible and the foot can be manually manipulated into its pre-disease configuration. Stage III is a continuance of the degeneration of these structures, the beginnings of soft tissue scarring and arthritis due to significantly out of alignment articular surfaces begins to stiffen the deformation into a more permanent and rigid configuration. Stage IV sees a rigid, fixed deformity of the foot and the beginnings of joint damage further upwards into the ankle level. Stages III and IV require more extensive surgical correction, Stage II is the earliest that surgical intervention is necessary[67,70,73,74,77].

The origins of the mechanical failure in this disease are centered about that early indication of weakening of the PTT[50,55,67,69-71,73-75,78-80]. The posterior tibialis muscle acts through the PTT at the talonavicular joint to stabilize and support the alignment of the medial arch. This muscle also provides some adduction and internal rotation at the midtarsal joint level. The tendon is thought to incur mounting micro damage that overcomes the rate of regeneration over a long period of time, this tendon frays and will eventually fully rupture[81]. The PTT is not the only supportive structure of the medial arch, the aforementioned spring ligament, long and short plantar ligaments, plantar fascia, deep tarsal ligaments, and portions of the medial and lateral collateral ligaments also play a role in the support of the medial arch[32,67,70,75,76,80-82]. These tissues degrade as their load increases during gait and stance in the absence of support

from the PTT[69,83.] In the duration preceding PTT rupture, there is a transfer of deformation-resisting load from that weakening tendon to these ligaments. When the PTT fails, these structures no longer have muscular support and now fully resist the deforming load of stance and gait. Over time the same overwhelming micro damage that lead to the degeneration of the PTT will break down these ligament structures, furthering the course of the disease[81,82].

A study was performed by Deland et al.[82] on a pool of 31 subjects which were diagnosed with AAFD and 31 control subjects who had ankle and hindfoot MR for reasons unrelated to flatfoot. Many ligaments in the foot were analysed with this MR data including: the spring ligament (divided into superomedial and inferomedial calacaneonavicular parts), long and short plantar ligaments, plantar fascia, deltoid ligament (divided into anterior, posterior, and deep parts), the plantar naviculocuneiform ligament, talocalcaneal interosseus ligament, and the tarsometatarsal ligaments. The bulk of these tissues, which experienced some instances of tearing, were divided up into a grade 0-IV classification of damage. Grade 0 denoted no visible alteration; grades I & II denote altered appearance (as seen by altered signal intensity on MR) of less than or more than 50% of the cross sectional area of the ligament, respectively; grades III & IV denote partial tearing of less than or more than 50%, respectively. A few tissues (plantar fascia, long and short plantar ligament) showed no tearing on imaging. These tissues were thus given a different gradation, mild (<25% altered appearance), moderate (25% - 50% altered appearance), and severe (>50% altered appearance)[82]. A summary of the results showed: the bulk of the superomedial spring ligament of subjects were grade IV; the inferomedial spring ligament at grade II; the majority of the talocalcaneal interosseus and anterior superficial deltoid ligaments at grade I; the deep deltoid, posterior superficial deltoid, plantar metatarsocuneiform, and naviculocuneiform ligaments at grade 0. For the mild/moderate/severe gradations the long

and short plantar ligaments were all mild, and the plantar fascia exhibited the majority of its findings to be moderate damage. The study also analyzed the PTT and found it to be, in the flatfoot group, mostly either grade III or IV. (Note that all measurements were primarily or solely grade 0 or mild, with the exception of the talocalcaneal interossues which was 12 subjects for grade 0, 17 subjects for grade I, and 2 subjects for grade II, an interesting finding)[82]. Even with these findings, the study asserted that there is no method of correlating these results with the functional behavior of ligaments.

Diagnosis, Stage II

Diagnosis at Stage II can be done early in the clinical setting with an examination. Under loading, such as relaxed standing, the degenerative signs of flatfoot including forefoot abduction, medial arch collapse, and hindfoot valgus are readily seen (Figure 5.1).

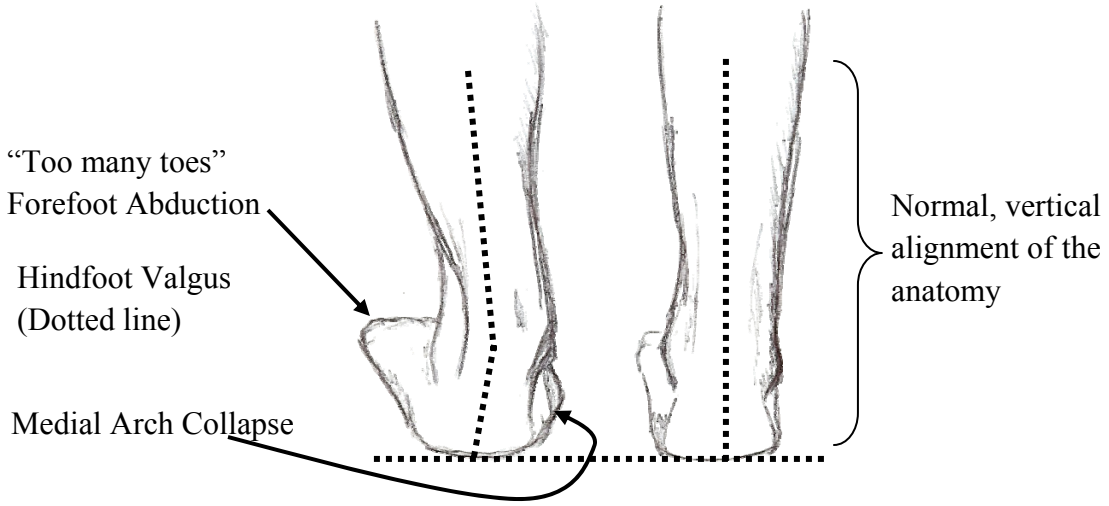

Figure 5.1: Diagram of Flatfoot. This diagram is a typical clinical presentation of flatfoot during relaxed stance. The left foot is showing the common indicators; forefoot abduction, hindfoot valgus, medial arch collapse. The right foot is "normal". Diagram is redrawn from common flatfoot imagery in the public domain.

The examining physician can manually manipulate the foot and determine the degree of flexibility remaining in the joints. For further measure and as a surgical guide, the degree of deformity at these joints can be quantified by joint angles measured radiographically. This method of diagnosis was standardized by Sangeorzan et al[84] in 1993 and has been used often since[69-72,76,79,85,82,83]. These quantifying measurements are made in two views, a lateral view and a "dorsoplantar" view. The lateral view is a standard image to show the mid-saggital plane of the foot. The second view is at an angle between observing the transverse plane and the coronal plane. For the purposes of simplification this view will be called an anteroposterior view tilted down 70° and lifted to above the foot (Figure 5.2).

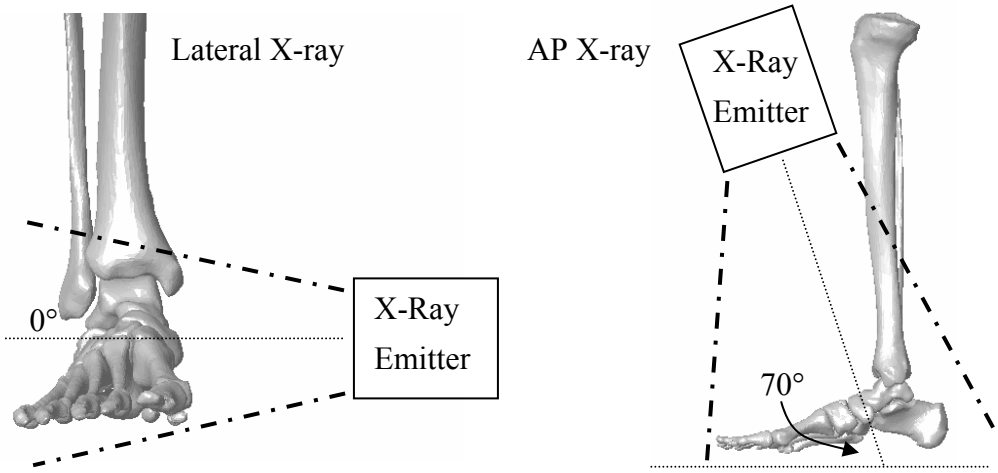

Figure 5.2: X-Ray Orientations for Flatfoot. Angles of orientation for capturing x-rays for diagnosis of flatfoot severity. The lateral view taken horizontally of the foot, left; the AP view taken from a 70° raised angle from the AP direction and centered over the midfoot, right.

This view captures the tilted superior view of the bones of the mid- and forefoot. In these views there are five major joint measures that can be made to describe the common deformities of AAFD. Talar 1st Metatarsal Angle: as seen in the lateral view. The talar axis is defined by the

following: the midpoint of a line passing through the dome of the talus to the inferior beak of the lateral process; and second midpoint, from a line which bisects the head of the talus and is identified at the articular borders. These 2 midpoints describe a talar axis. The metatarsal axis is described by 2 points, which are both midpoints of lines which terminate on the superior and inferior borders of the proximal and distal diaphyseal limits. The angle between these axes is the Talar 1st Metatarsal Angle (L-T1MT) in the lateral view (Figure 5.3, top). Calcaneal Pitch: seen from the lateral view. A line drawn from the inferior border of the calcaneal tuberosity to the anterior inferior articular process; is compared to a line drawn from the inferior border of the calcaneal tuberosity to the distal inferior articular border of the first metatarsal. This compared angle is calcaneal pitch (L-CP) in the lateral view (Figure 5.3, middle). TaloCalcaneal Angle: seen from the lateral view. A line drawn from the midpoint of a line connecting the superior and inferior aspects of the posterior calcaneal tuberosity, and a second midpoint from a line drawn between the superior and inferior borders at the level of the sustentaculum tali form the calcaneal axis. This axis and the talar axis described for L-T1MT angle describe the TaloCalcaneal (L-TC) angle in the lateral view (Figure 5.3, bottom).

Talo 1st Metatarsal Angle: as seen in the AP view. An axis is defined as normal to the midpoint of a line drawn between the medial and lateral borders of the talar articular surface. The metatarsal axis is described by 2 points, which are both midpoints of lines which terminate on the medial and lateral borders of the proximal and distal diaphyseal limits. The angle between these 2 axes is the Talo 1st Metatarsal angle (AP-T1MT) in the AP view (Figure 5.4, left). Talonavicular Angle: seen from the AP view. A line perpendicular to the midpoint of a line bisecting the proximal articular borders of the navicular describes a navicular axis. The same talar axis from the AP-T1MT view is used as well. The angle between these axes is the

talonavicular angle (AP-TN) in the AP view, also known as talonavicular coverage angle (Figure 5.4, right).

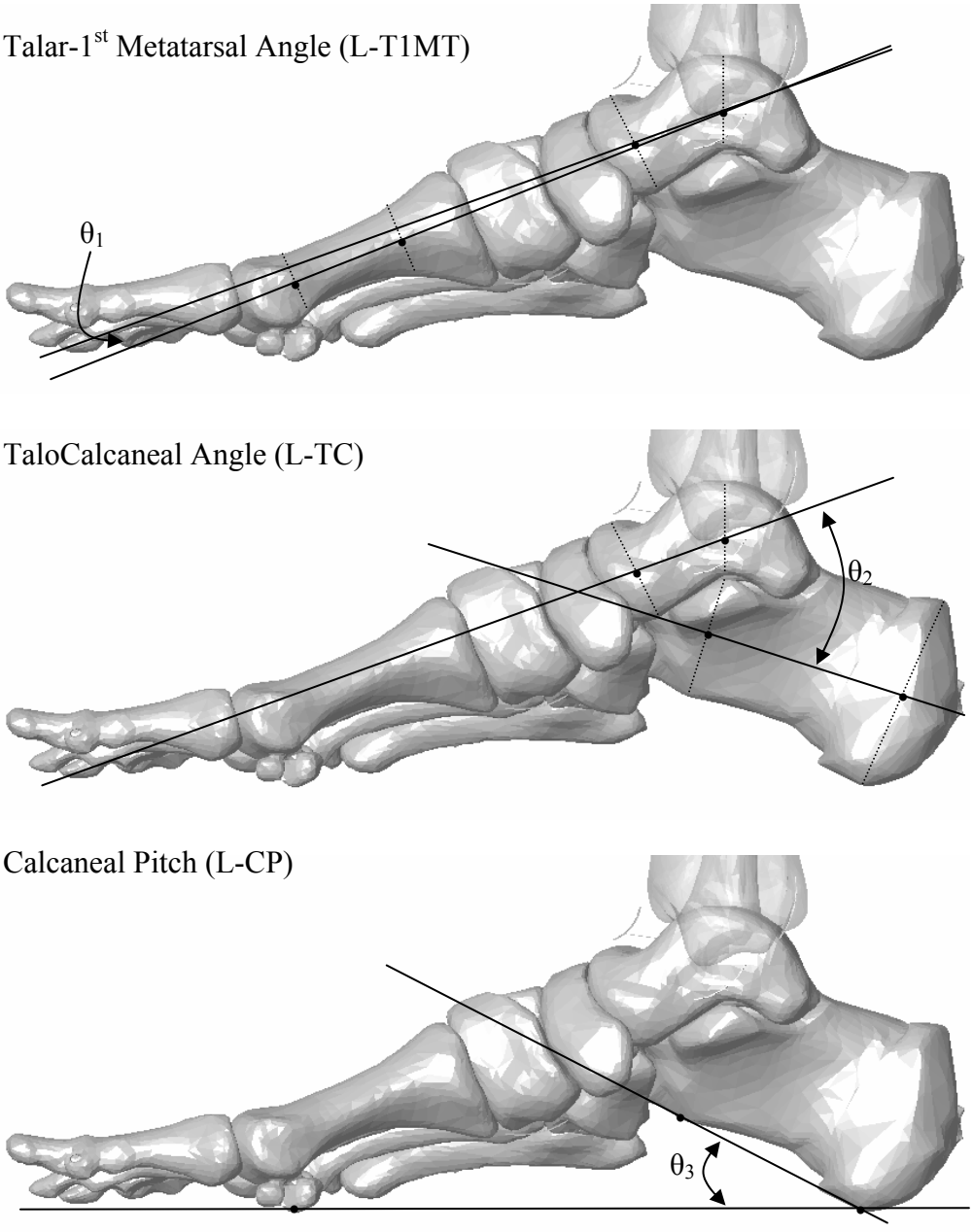

Figure 5.3: Lateral x-ray Angle Measurement Technique. The diagrams presented here illustrate the methods mentioned in literature[67,84] to create the lateral angle measurements for L-T1MT, L-TC, and L-CP angles. Dotted lines and bullets show anatomical landmarks and measurements used to generate angle axes (solid), with accompanying angle measure $\theta_{1\text{-}3}$.

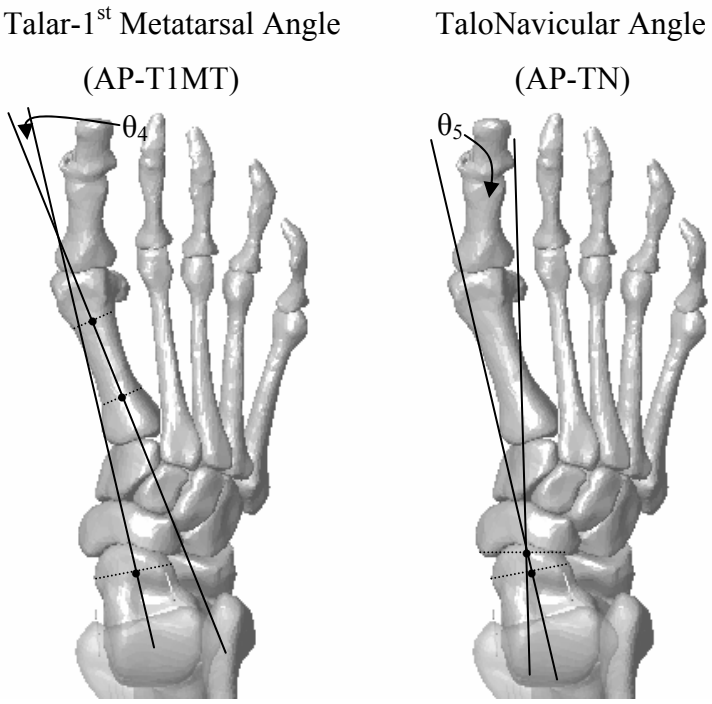

Figure 5.4: AP and Angle Measurement Techniques. The diagrams presented illustrate the methods mentioned in literature[67,84] to create the AP angle measurements for AP-T1MT, and AP-TN angles. For these the talar and navicular axis, the axis itself is drawn normal to the single dotted lines connecting the medial and lateral borders of the articular surfaces. Dotted lines and bullets show anatomical landmarks and measurements used to generate angle axes (solid), with accompanying angle measure $\theta_{4\text{-}5}$.

Treatments

As mentioned, surgical intervention at Stage II AAFD is capable of relieving many of the symptoms and underlying causes of the disease and preventing its further progression into Stage III and IV. This intervention is accomplished by a series of soft tissue and bony procedures which work in conjunction to correct the morphology seen in AAFD and strengthen the architecture of the foot.

A survey of 104 orthopaedic surgeons in 2003 gave the following breakdown in treatment choices when presented with a typical Stage II AAFD case: of soft tissue procedures, 94% would perform some reconstruction of the PTT, 53% would repair the spring ligament; of bony procedures, 73% would perform a medializing calcaneal osteotomy (MCO) and 41% would perform a lateral column lengthening procedure[74]. This study identifies a short list of bony procedures which are of particular importance to this simulation.

Medializing Calcaneal Osteotomy

The hindfoot valgus deformity mentioned in association with AAFD is of particular concern when treating this disease. Hindfoot valgus is a positive feedback deformity. Once the line of action of the Achilles tendon is no longer centered through the ankle center, the gastrocnemius and soleus apply an externally rotating moment about this joint, through the tendon, which acts to further hindfoot valgus. The Medializing Calcaneal Osteotomy (MCO) is often performed as a hindfoot valgus corrective procedure[70,73,74,79,86]. The primary objective of the MCO is to alter the insertion location of the soleus / gastrocnemius complex in an effort to re-establish the neutral pull direction of the Achilles tendon. This maintains its strength as a plantorflexor and diminishes its capability of causing hindfoot valgus. The osteotomy is accomplished by removing the entire calcaneal posterior tuberosity from the body of the calcaneus. The tuberosity is "slid" medially approximately 1cm then screwed in place through the posterior heel to reduce and stabilize the fragment in its new location. The movement of this fragment, the insertion of the Achilles tendon, effectively realigns the tendon pull with the ankle rotational center to restore joint appearance as in the right foot of Figure 5.1.

Lateral Column Lengthening

Two other major morphological deformities of the presenting Stage II AAFD are very significant forefoot abduction and medial arch collapse. These deformities can be treated with a lateral column procedure, which in essence expands the lateral column to drive the forefoot into adduction and shore up the medial arch in the process. The Evans opening wedge osteotomy (Evans), and CalcaneoCuboid Distraction Arthrodesis (CCDA) are the most common of these LCL procedures[69,68,70,73,74,79,87-89,86].

The Evans procedure is performed by creating an osteotomy in the anterior calcaneus, in the coronal plane usually ~1cm behind the anterior articular facet. The calcaneus is then "opened" laterally and a wedge (usually an auto graft bone wedge) is inserted into the osteotomy. The wedge is approximately 1cm in width at its external side. The graft and calcaneus are held in place to heal with a small plate and unicortical screws. This wedging expands the length of the lateral column and is thus a lengthening procedure.

The difference between the CCDA procedure and the Evans osteotomy is location. The CCDA wedge is inserted between the calcaneus and the cuboid. To accomplish this fusion, the calcaneocuboid joint capsule is opened laterally and the articular surfaces are shaved back to subchondral bone. The typical ~1cm wedge, as created for the Evans procedure, is inserted into this joint space and the fusion is reduced by a small plate and unicortical screws. This wedging procedure, as Evans, expands the length of the lateral column and is thus classified as a lengthening procedure. While a wide range of angle changes results, correction of excessive forefoot abduction is the most significant outcome following a LCL procedure. The Evans procedure has been reported to result in a 12.5 to 26° correction at the talonavicular joint[66,68,84] while the CCDA procedure results in 11.2 to 26.2° correction at this level[69,68].

Complications associated with both Evans and CCDA include non- or delayed union, incision site problems (sural nerve damage, infection, painful hardware), arthritic development, and tightness or pain in the lateral foot[69,66,68,90]. It has been demonstrated experimentally that the Evans procedure increases passive tension in the lateral portion of the long plantar ligament with a decrease or slackening in the medial portion[91]. A slackened medial plantar fascia was created experimentally after application of either a CCDA or MCO, with more loosening seen after the CCDA[58]. These findings may describe phenomenon that correspond to reported lateral foot pain following surgery[66]. In addition to ligament strain, the Evans procedure has been shown to experimentally increase calcaneocuboid joint contact force, which is an arthritic risk factor[64,65,68,92,93]. Finally, these corrections can alter not only tissue loading and joint contact, but gait and foot biomechanics by impacting plantar pressure distributions[94-96,89,90].

Soft Tissue Procedures

Soft tissue repair re-establishes the support once granted by the failed posterior tibial tendon. Restoring the function of the PTT is almost exclusively accomplished by a tendon transfer, commonly from the flexor digitorum longus[67,69,70,73,79,97]. This transfer is performed by removing the flexor digitorum tendon from its distal insertion, and binding the tendon to the damaged tibialis posterior insertion. This serves to utilize the muscular pull of the flexor digitorum to reestablish the stability granted to the medial arch by the tibialis posterior.

5.3 Materials and Methods

Loading Parameters: For bodyweight, a downward force vector of 690N was applied at the proximal tibia to load the foot and ankle as in stance. The Achilles soft tissue element array was set to ½ body weight or 345N. For a relaxed weight-bearing stance, muscle activation

beyond that of the soleus / gastrocnemius complex is minimal and was excluded from the simulation[83,92].

Modeling Stage II Flatfoot: The approach to creating the soft tissue flatfoot model hinged around the MR study performed by Deland et al.[82] which investigated which and to what degree soft tissue structures displayed possible damage. Those categories of altered appearance of the ligament tissue as well as degree of full thickness tearing served as a template to adjust the stiffness values of affected ligaments in the model (Table 5.1).

Structure	Average Damage Level	Stiffness Modification
Superomedial Spring	Stage IV	-7/8th
Inferomedial Spring	Stage II	-3/8th
Talocalcaneal Interosseus	Stage I	-1/8th
Plantar Fascia	Stage I	-1/8th
Plantar metatarsocuneiform	Stage 0	None
Plantar naviculocuneiform	Stage 0	None
Long and Short plantar	Stage 0	None
Deep deltoid	Stage 0	None
Anterior superficial deltoid	Stage I	-1/8th
Posterior superficial deltoid	Stage 0	None

Table 5.1: Flatfoot Damage Classification and Stiffness Modification. This table shows the "flatfoot scheme" applied to the model to simulated ligament deficiency with this disease. Stiffness modification was used to alter the behavior of the ligament arrays in the properties spreadsheet for these simulations.

To create this template a scaling of ligament stiffness was applied to the grade 0-IV experimental findings. The scaling started at 100% intact stiffness for grade 0 and ramped up to 12.5% intact stiffness ($1/8^{th}$) for grade IV. This 12.5% assumed a slightly less than full thickness dissection of the tissue. For simplicity (as stated in the study no correlation can be made, only assumed, between MR appearance and ligament function) a linear scale was applied between the

endpoints. Intermediate grades were thus scaled in eights. The only tissue to show non-intact levels in the mild/moderate/severe grading was the plantar fascia, its stiffness was scaled to 87.5% ($7/8^{th}$) to reflect a grade I degradation (Table 5.2). As with the arch stability study, these scaling factors were applied to a copy of the master ligament properties sheet to yield updated formulation reflective of flatfoot (Table 5.3).

Ligament	Stiffness	Stiffness Adj	Flatfoot Stiffness
Interosseus Talocalcaneal 1	90	-12.5%	78.75
Interosseus Talocalcaneal 2	90	-12.5%	78.75
Interosseus Talocalcaneal 3	90	-12.5%	78.75
Plantar Calcaneonavicular (Spring) 1	50	-37.5%	31.25
Plantar Calcaneonavicular (Spring) 2	50	-37.5%	31.25
Plantar Calcaneonavicular (Spring) 3	50	-87.5%	6.25
Plantar Calcaneonavicular (Spring) 4	50	-37.5%	31.25
Plantar Fascia Base 1	40	-12.5%	35
Plantar Fascia Base 2	40	-12.5%	35
Plantar Fascia Base 3	40	-12.5%	35
Plantar Fascia Base 4	40	-12.5%	35
Plantar Fascia Base 5	40	-12.5%	35
Plantar Fascia End 1	60	-12.5%	52.5
Plantar Fascia End 2	50	-12.5%	43.75
Plantar Fascia End 3	50	-12.5%	43.75
Plantar Fascia End 4	20	-12.5%	17.5
Plantar Fascia End 5	20	-12.5%	17.5
Tibionavicular Part 1	40	-12.5%	35
Tibionavicular Part 2	40	-12.5%	35
Tibiospring 1	200	-12.5%	25
Tibiospring 2	61	-87.5%	7.625

Table 5.2: Ligament Element Spreadsheet, Flatfoot Stiffness Adjustments. The ligament arrays and elements this scheme effected. Showing original stiffness values, adjustment based on Table 5.1 and final flatfoot stiffness values for affected ligaments

Ligament	Flatfoot Ligament Equation
Interosseus Talocalcaneal 1	IF(DM(4421,4422)-7.6512:0,0,-78.75*(DM(4421,4422)-7.6512)-0.1*VR(4421,4422))
Interosseus Talocalcaneal 2	IF(DM(4423,4424)-6.0192:0,0,-78.75*(DM(4423,4424)-6.0192)-0.1*VR(4423,4424))
Interosseus Talocalcaneal 3	IF(DM(4425,4426)-4.9536:0,0,-78.75*(DM(4425,4426)-4.9536)-0.1*VR(4425,4426))
Plantar Calcaneonavicular (Spring) 1	IF(DM(4487,4488)-22.1568:0,0,-31.25*(DM(4487,4488)-22.1568)-0.1*VR(4487,4488))
Plantar Calcaneonavicular (Spring) 2	IF(DM(4489,4490)-19.9968:0,0,-31.25*(DM(4489,4490)-19.9968)-0.1*VR(4489,4490))
Plantar Calcaneonavicular (Spring) 3	IF(DM(4491,4492)-17.664:0,0,-6.25*(DM(4491,4492)-17.664)-0.1*VR(4491,4492))
Plantar Calcaneonavicular (Spring) 4	IF(DM(4493,4494)-17.2512:0,0,-31.25*(DM(4493,4494)-17.2512)-0.1*VR(4493,4494))
Plantar Fascia Base 1	IF(DM(5515,5516)-62.2752:0,0,-35*(DM(5515,5516)-62.2752)-0.1*VR(5515,5516))
Plantar Fascia Base 2	IF(DM(5517,5518)-59.2992:0,0,-35*(DM(5517,5518)-59.2992)-0.1*VR(5517,5518))
Plantar Fascia Base 3	IF(DM(5519,5520)-57.4656:0,0,-35*(DM(5519,5520)-57.4656)-0.1*VR(5519,5520))
Plantar Fascia Base 4	IF(DM(5521,5522)-55.3728:0,0,-35*(DM(5521,5522)-55.3728)-0.1*VR(5521,5522))
Plantar Fascia Base 5	IF(DM(5523,5524)-55.1328:0,0,-35*(DM(5523,5524)-55.1328)-0.1*VR(5523,5524))
Plantar Fascia End 1	IF(DM(5525,5526)-63.024:0,0,-52.5*(DM(5525,5526)-63.024)-0.1*VR(5525,5526))
Plantar Fascia End 2	IF(DM(5527,5528)-68.2176:0,0,-43.75*(DM(5527,5528)-68.2176)-0.1*VR(5527,5528))
Plantar Fascia End 3	IF(DM(5529,5530)-64.464:0,0,-43.75*(DM(5529,5530)-64.464)-0.1*VR(5529,5530))
Plantar Fascia End 4	IF(DM(5531,5532)-59.5584:0,0,-17.5*(DM(5531,5532)-59.5584)-0.1*VR(5531,5532))
Plantar Fascia End 5	IF(DM(5533,5534)-51.12:0,0,-17.5*(DM(5533,5534)-51.12)-0.1*VR(5533,5534))
Tibionavicular Part 1	IF(DM(4625,4626)-27.84:0,0,-35*(DM(4625,4626)-27.84)-0.1*VR(4625,4626))
Tibionavicular Part 2	IF(DM(4627,4628)-25.7088:0,0,-35*(DM(4627,4628)-25.7088)-0.1*VR(4627,4628))
Tibiospring 1	IF(DM(4629,4630)-18.1728:0,0,-25*(DM(4629,4630)-18.1728)-0.1*VR(4629,4630))
Tibiospring 2	IF(DM(4631,4632)-25.536:0,0,-7.625*(DM(4631,4632)-25.536)-0.1*VR(4631,4632))

Table 5.3: Ligament Element Spreadsheet, Flatfoot Ligament Equations. Grouped element function equations for the modeled ligaments affected by the flatfoot scheme as they would be entered in COSMOSMotion.

Modeling the Medializing Calcaneal Osteotomy: This hindfoot osteotomy was created in SolidWorks by directly modifying the calcaneus. A line in the lateral view was manually positioned to isolate the Achilles tuberosity from the body of the calcaneus. Using this line, three points around the tuberosity were chosen to define a plane. The plane was used as a guide for a "split" feature which detached the fragment of the tuberosity. The "copy/move" feature was then applied to the fragment to move it medially (along a medial line entity) 10mm. A "combine" feature was then used to reaffix the fragment to the body of the calcaneus to form the MCO (Figure 5.5).

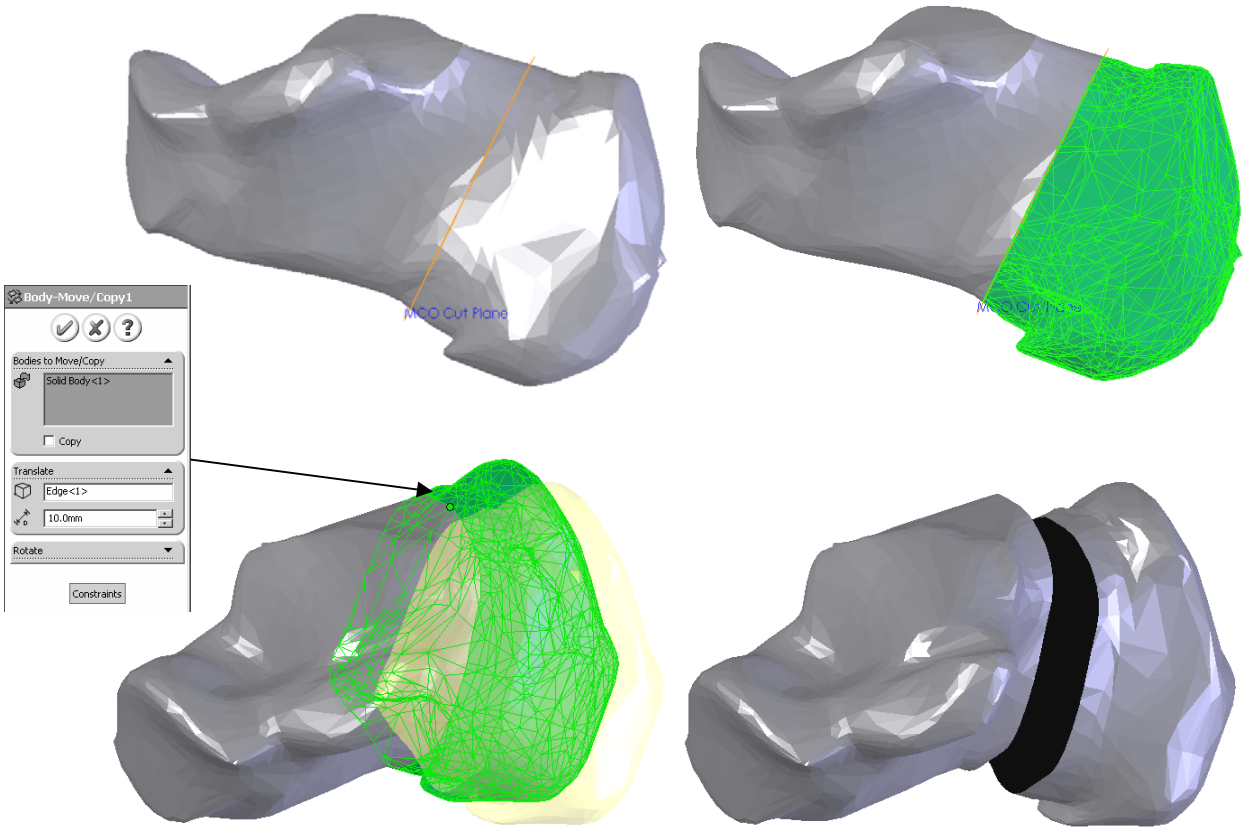

Figure 5.5: Creation of the MCO. The MCO was created in SolidWorks using a variety of cut, move, and combine features along with some reference geometry. The intact geometry with window from a medial view (upper left), separated tuberosity fragment (upper right), MCO slide performed with the "move/copy" feature window shown in an oblique view (lower left), and final medialized osteotomy with highlighted (black) cut face (lower right).

Modeling the Evans Procedure: In a manner similar to the MCO, a line was used to isolate the anterior facet of the calcaneus approximately 10mm behind the anterior articular surface (calcaneocuboid articulation). From this line a reference plane was created to be parallel to the articular surface and existing at the osteotomy depth. The isolated portion was detached with the "split" feature, and the fragment became a second body. This fragment was rotated

internally about its medial most edge. Through measurement, a rotation of 21.5° was found to be necessary to open the lateral cut surface of the calcaneus by 10mm. The wedge was extruded as a solid feature with a rectangular cross section, inside the osteotomy space. On attempting to use the "combine" feature to resolve the wedge, fragment, and body of the calcaneus into one solid body a "zero thickness geometry" error was tripped. This error was due to the body to body point contact at the medial border of the osteotomy, SolidWorks does not allow bodies to be in point contact and still joined. To account for this the small flaring section of the medial fragment border was removed with a cut to separate that contact between fragment and body, and the "combine" proceeded without further error as the solid bodies were fused to form the Evans osteotomy (Figure 5.6).

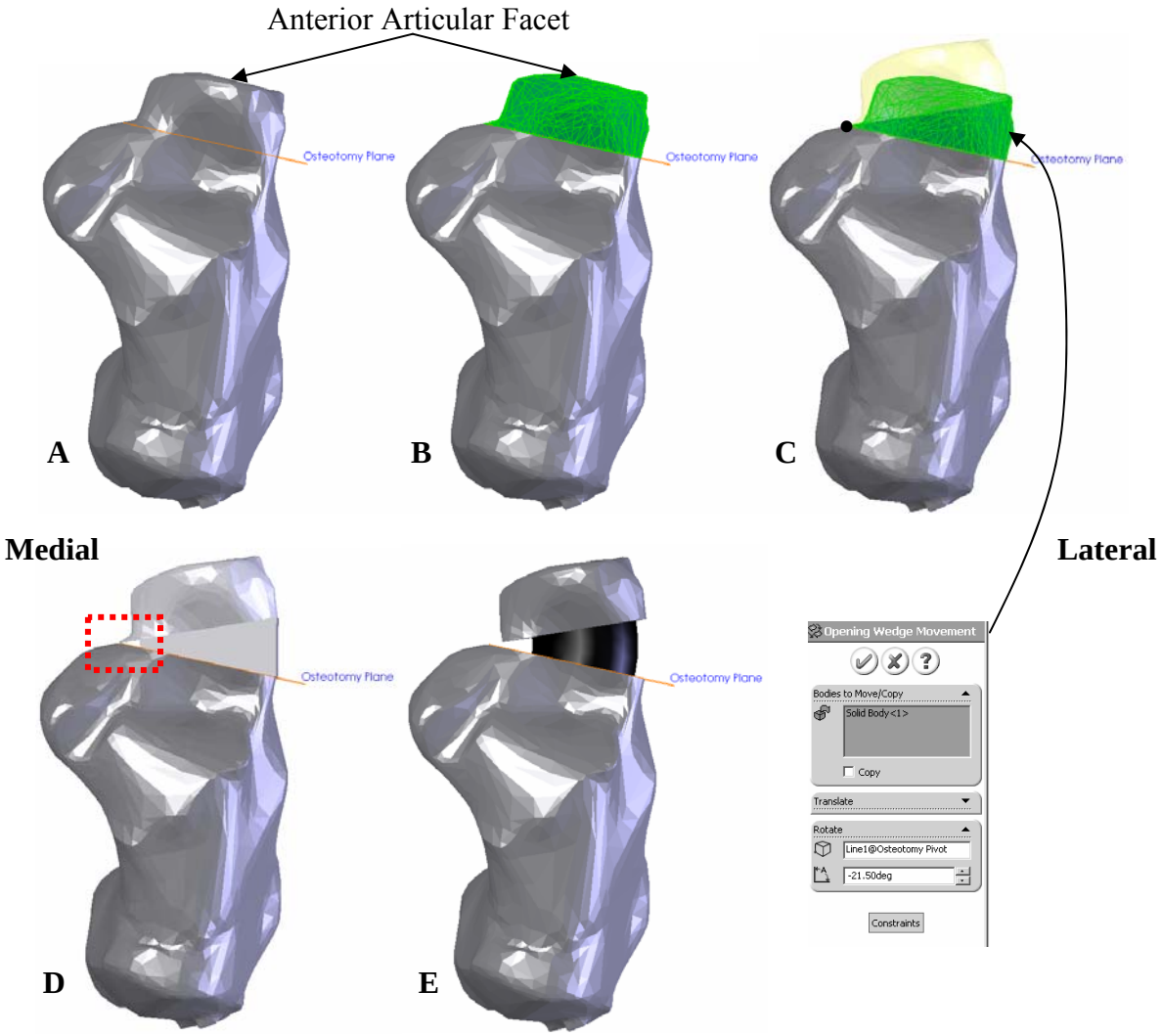

Figure 5.6: Evans Opening Wedge Osteotomy, Calcaneus. All images are superior views. The opening wedge osteotomy was performed with a similar line to plane formation for osteotomy reference as the the MCO. The cut plane for this osteotomy was placed 1cm posterior to the anterior articular facet, A and B. The fragment was rotated about the medial edge of the cut, C - bullet. Body-body point contact causing "zero thickness geometry" error shown within red dashed box, D. Final wedge fragment trimmed to be within the bony borders of the calcaneus, E. Rotation to fit the 1cm osteotomy was found to be 21.5° (lower right).

Modeling the CCDA: In a similar manner as previous, approximately 3mm of the most superficial shared articular joint surfaces of the cuboid and calcaneus were removed to leave flat geometry. The cuboid was then rotated internally about its medial border with the calcaneus such that a 10mm wide, full depth wedge could be placed between the two bones. Wedge, cuboid, and calcaneus were then fused to form the CCDA (Figure 5.7).

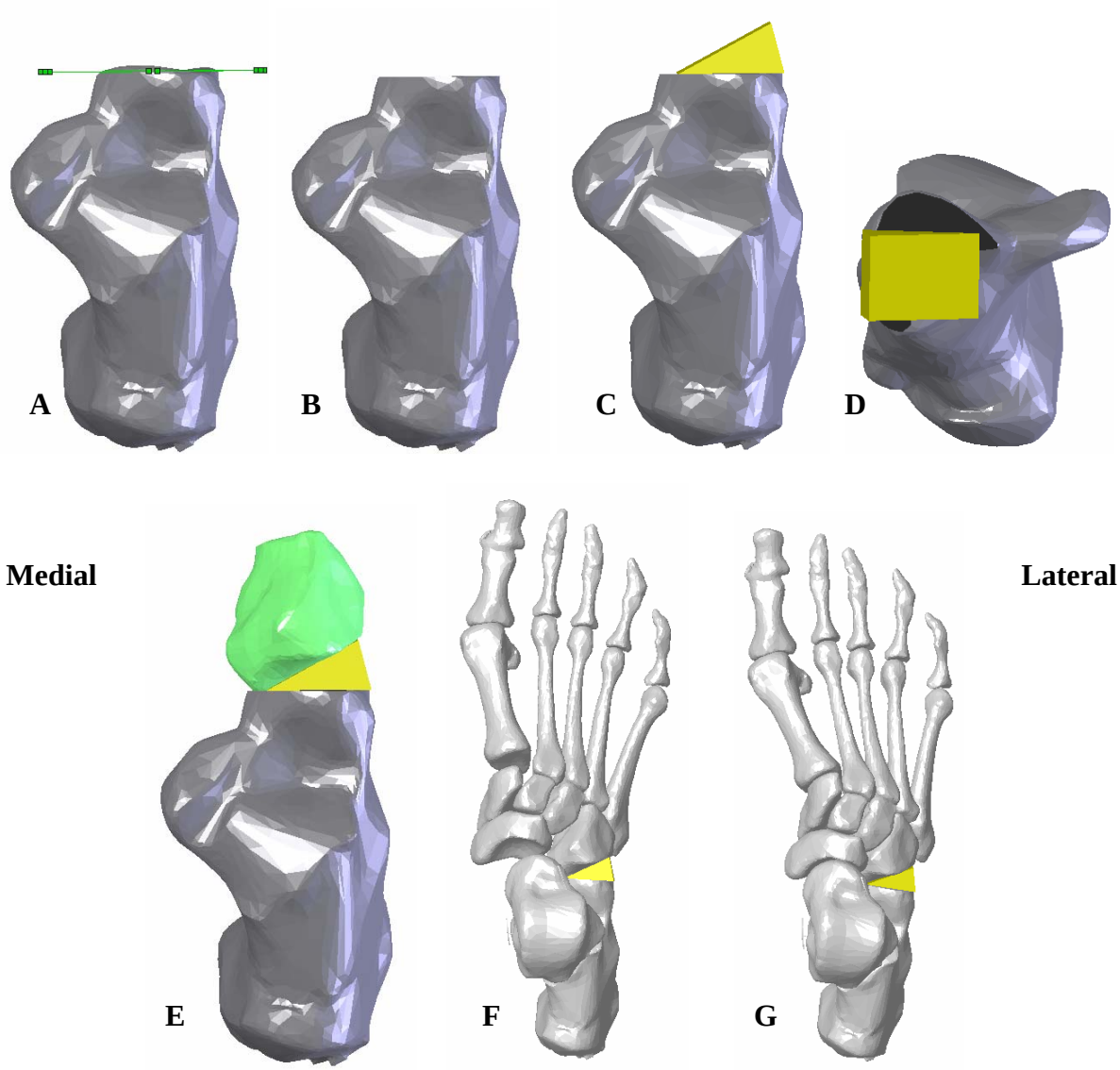

Figure 5.7: Modeling the CCDA. All views superior except D which is anterior. The calcaneocuboid distraction arthrodesis was performed by first simulating the shaving of articular surfaces calcaneus and cuboid. Points on the calcaneal anterior articular surface were chosen

which represented the plane of that surface. These points were used to create a reference plane which was used in an "extrude cut" feature to remove the anterior 0.5mm of surface, A and B. This was done to the cuboid as well to yield flat articular geometries. These flat geometries were mated to a 1cm wide wedge in a similar manner to the Evans osteotomy to cover the articular surface, C through E. To prevent excessive initial 3D body interference from failing simulation, the mid and forefoot were manually translated ~1cm to remove this time zero interference, F. Bony articulations were reestablished in the first frame of simulation, G.

Simulations and Measurements: Seven configurations were simulated in total: normal intact, flatfoot, and flatfoot at various osteotomy states (MCO, Evans, CCDA, Evans & MCO, CCDA & MCO). Radiographic views of flatfoot were created and measurements were standardized by adding referencing markers to anatomic landmarks used for flatfoot diagnosis. Such markers described the following measures: in the Lateral view; Talo-1st MetaTarsal (L-T1MT), Calcaneal Pitch (L-CP), and TaloCalcaneal (L-TC) joint angles; in the AnteroPosterior (AP) view: Talo-1st MetaTarsal (AP-T1MT) and TaloNavicular coverage (AP-TN) angles); refer back to Figure 5.3 and Figure 5.4. Soft tissue strain was measured directly from the elongation of soft tissue ligament arrays across both the long plantar ligament and plantar fascia. Total contact force between the calcaneus and cuboid were measured in all simulations except those containing the CCDA where the joint was fused. Plantar load magnitudes were measured through bony ground contact at the distal rays and at the calcaneus. Calcaneal varus / valgus: is often mentioned as a clinically observable marker but radiographs are typically not used to measure this. A method was devised computationally by using the posterior ground surface and an axis from a manually positioned mid-sagittal plane in the calcaneal body (Figure 5.8).

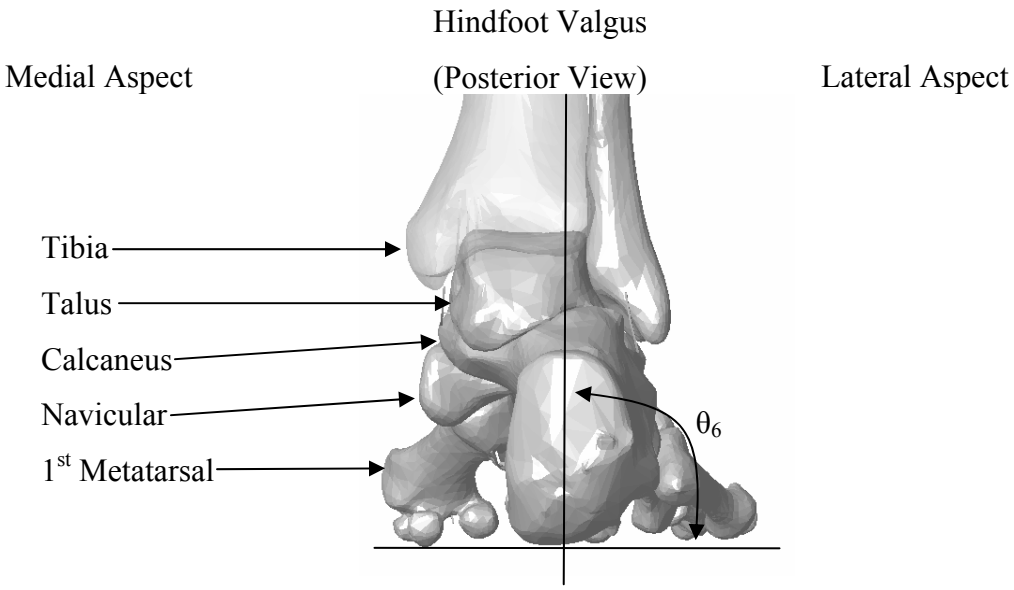

Figure 5.8: Hindfoot Valgus Measurement Technique. Hindfoot valgus measure as seen in the posterior view. Angle is measured in this method from the lateral side. Horizontal axis represents the level of the ground, vertical axis is created in the calcaneal part file from a sagittal plane located at the center of the geometry, from these axes the hindfoot valgus angle is determined θ_6

5.4 Results

Radiographic Joint Angles: The joint angle data showed the changes the flatfoot model imparted in comparison to intact and the subsequent changes imposed by the simulated surgical corrections (Table 5.4). The flatfoot model resulted in a 9.1° drop in the arch when considering the L-T1MT angle. This change was accompanied by a 1.6° plantarflexion of the talus seen in the L-TC and a 2.6° reduction in L-CP. In the AP view, both the AP-T1MT and the AP-TN angles abducted by 8.9° and 1.9°, respectively.

Joint Angle (°) †	Normal	Flatfoot					
	Intact	Intact	MCO	Evans	CCDA	Evans & MCO	CCDA & MCO
L-T1MT (θ_1)	0.5	-8.6	-3.7	2.9	6.8	1.2	0.8
L-TC (θ_2) ††	39.4	41.0	37.9	43.2	37.5	41.3	35.8
L-CP (θ_3)	16.6	14.0	13.1	19.5	15.7	17.0	13.7
AP-T1MT (θ_4)	7.2	-1.7	7.2	11.9	16.8	13.5	20.5
AP-TN (θ_5)	-7.0	-8.9	-6.5	2.4	-2.4	3.5	-0.4
Hindfoot (θ_6) ††	93.4	96.4	87.7	94.7	93.1	90.9	86.9

Table 5.4: Joint Angles For Simulation States. Joint angles measured for normal and flatfoot surgical stages, in degrees, as depicted in Figure 2. Angles are: Lateral Talo-1st MetaTarsal (L-T1MT), θ_1; Lateral TaloCalcaneal (L-TC), θ_2; Lateral Calcaneal Pitch (L-CP), θ_3; AnteroPosterior Talo-1st MetaTarsal (AP-T1MT), θ_4; AnteroPosterior TaloNavicular angle (AP-TN), θ_5, Hindfoot varus / valgus (Hindfoot), θ_6. † Negative values denote crossing a neutral axis: for L-T1MT, this signifies a drooping medial arch; for AP-T1MT and AP-TN, this signifies abduction. †† neither the L-TC nor hindfoot angles have an associated neutral axis. L-TC values greater than intact normal indicate talar plantarflexion. Hindfoot less or greater than intact indicate more varus and valgus, respectively.

With the MCO: L-T1MT angle improved by 4.9° not reaching the normal intact level; the talus dorsiflexed by 3.1° at the L-TC angle passing the normal intact; L-CP worsened 0.9°; AP-T1MT angle improves by 8.9° in a return to normal intact; AP-TN improves by 2.4 to near normal. The Evans and CCDA: both improve L-T1MT angle by 11.5° and 15.4° from flatfoot, surpassing intact; L-TC angle worsened 2.2° with the Evans while improving by 3.6° with CCDA to pass normal intact; L-CP improved in both cases, 5.5° with Evans and 1.7° with CCDA to beyond intact normal; both procedures also improved AP-T1MT and AP-TN by adducting these joints, 13.6° and 18.5° at the AP-T1MT for Evans and CCDA respectively; 11.3°

and 6.5° at the AP-TN for Evans and CCDA respectively – AP angles all surpassing intact levels.

For Evans & MCO and CCDA & MCO: trends were similar, L-T1MT angles were improved by 9.8° and 9.4° for Evans & MCO and CCDA & MCO respectively to near intact normal; at the L-TC angle, Evans & MCO worsened by 0.3° while CCDA & MCO improved by 5.2° surpassing intact normal; a reverse was seen at L-CP with Evans & MCO improving 3.0° to near normal intact while CCDA & MCO worsened by 0.3°; Evans & MCO improved AP-T1MT by 15.2° and CCDA & MCO by 22.2° both surpassing intact normal; Evans & MCO improved AP-TN by 12.4° and CCDA & MCO by 8.5° both surpassing intact normal.

Calcaneal varus/valgus was also influenced by these procedures. In the intact normal foot, the calcaneal angle was 93.4°. The flatfoot model brought the calcaneus 3° further into valgus. The MCO alone corrected this angle with 8.7° of varus rotation from flatfoot, surpassing intact normal. Evans and CCDA both also corrected this angle by 1.7° and 3.2° respectively. Evans & MCO affected this angle less than MCO alone but greater than Evans, with a 5.5° varus rotation. CCDA & MCO affected this angle greater than either procedure alone, with a 9.5° varus rotation from flatfoot.

Ligament Strain: Soft tissue strains in the long plantar ligament and plantar fascia were calculated from resting and loaded stance lengths (Table 5.5). Medial / lateral tissue strain distribution was relatively equal in the intact normal simulation. With flatfoot, an overall increase in tissue strain was seen with medial ligament portions being affected more than lateral portions. The MCO countered this somewhat, shifting the greater strains to the lateral portions and slightly easing medial portions. Both Evans and CCDA followed this trend but with slightly less lateral strain in the long plantar ligament and slightly more in the plantar fascia. Evans or

CCDA with MCO procedures affected a lessening of medial strains in the long plantar ligament close to intact normal levels whereas medial strain in the plantar fascia lessened past intact normal levels. Lateral strain for the combination procedures was highest in the long plantar ligament and relatively unchanging in the plantar fascia compared to either procedure without MCO.

% Strain in Ligament Structures	Normal	Flatfoot					
Long Plantar Array	Intact	Intact	MCO	Evans	CCDA	Evans & MCO	CCDA & MCO
Long Plantar 1 (med)	1.0	2.8	2.1	2.4	2.1	1.9	1.4
Long Plantar 2	1.0	2.8	2.5	2.7	2.3	2.2	2.2
Long Plantar 3	1.5	2.8	2.5	3.0	2.5	2.7	2.0
Long Plantar 4	1.8	2.3	3.1	3.4	2.9	3.3	2.2
Long Plantar 5	1.7	2.9	2.7	3.5	2.9	3.5	2.6
Long Plantar 6	1.8	2.7	3.0	3.9	3.2	4.0	3.2
Long Plantar 7	0.6	1.2	2.1	2.7	2.0	3.5	3.1
Long Plantar 8 (lat)	1.7	1.7	5.3	4.1	4.0	5.6	6.0
Plantar Fascia Array	Intact	Intact	MCO	Evans	CCDA	Evans & MCO	CCDA & MCO
Plantar Fascia 1 (med)	3.9	7.2	3.4	2.5	2.0	1.6	0.4
Plantar Fascia 2	2.1	4.3	2.1	2.2	1.8	1.2	0.5
Plantar Fascia 3	2.7	4.5	3.5	3.5	3.3	2.5	1.5
Plantar Fascia 4	2.7	4.0	3.6	4.7	4.1	5.1	3.8
Plantar Fascia 5 (lat)	3.2	3.7	4.2	4.7	4.7	4.7	4.8

Table 5.5: Ligament Strain. Soft tissue strains calculated from resting to loaded, in percent strain, for the long plantar ligament and plantar fascia for all computational simulations. Elements of these ligaments are listed medial (med) to lateral (lat).

Calcaneocuboid Contact Load: The calcanealcuboid joint load in the intact normal loaded foot was 763N. This load rose 16% to 888N in flatfoot and dropped to near intact normal levels (772N) with an MCO. Calcanealcuboid joint load increased 111% to 1608N, more than doubling, with the Evans procedure. The addition of the Evans procedure to an MCO only slightly reduced this increase, to 93% above intact normal or 1471N.

Plantar Ground Loads: In the intact normal foot, forefoot load was well balanced with 116N in the first ray and 125N in combined rays 4 & 5 (Table 5.6). Flatfoot raised the 1st ray ground contact by 7.8%, to 125N and also doubled 2nd ray ground contact. With respect to intact

normal, the MCO halved the 1st ray load while increasing 4th & 5th ray combined loads by 131%. Also with respect to intact normal, both Evans and CCDA reduced flatfoot forefoot loading by greater than 67% and 84% respectively, while increasing 4th & 5th ray loading by 105% and 114% respectively. The combinations of Evans or CCDA with MCO exhibited the greatest redistribution with respect to normal intact – 93% and 100% reduction of 1st ray loading and 154% and 171% increase in 4th & 5th ray combined loading, respectively. In the lateral 4th and 5th rays, the 5th ray always exhibited the greater ground contact load.

Load in Plantar Region	Normal	Flatfoot					
	Intact	Intact	MCO	Evans	CCDA	Evans & MCO	CCDA & MCO
Ray 1	116	125	58	38	18	8	0
Ray 2	8	16	2	6	9	4	0
Ray 3	40	36	23	38	47	25	26
Ray 4	24	30	79	52	49	56	53
Ray 5	61	60	117	122	133	160	177
Calcaneus	428	422	410	431	448	443	441

Table 5.6: Plantar Ground Contact Loads. Plantar ground contact loads, in Newtons. Listed are loads under rays 1-5 as well as the heel.

5.5 Discussion

In this validation study, model predicted several biomechanical functions of the foot and ankle in these simulated states – intact, flatfoot, and four different surgical corrective procedures for Stage II AAFD.

Radiographic Joint Angles: The joint angles found in the intact simulation were compared to available definitions of the clinically "normal" foot. The L-T1MT angle is considered normal at close to 0 degrees[70] and has been reported at 3.3° ± 4.9° in a study of 56 normal feet[76], and 0.0° ± 0.5° in a study of 1174 normal feet[85]. The intact L-T1MT angle in the simulation was 0.5°. L-TC angles are found from 50.3° ± 5.6° to 45.8° ± 0.4° in literature[76,85]; this angle in simulation was 39.4°. L-CP is reported to be 22.8° ± 4.7° for intact[76]; in simulation,

this angle was 16.6°. AP-T1MT angle is not as widely reported for intact feet for which the simulation angle was 7.2° into adduction from neutral. AP-TN coverage angles have been reported at 10.4° ± 4.2° for intact feet[85] and was 7.0° in simulation. Hindfoot valgus angle was reported at 5° (range 3° to 7°) for an intact population of 56 feet and 9° (range 4° to 15°) for a clinical flatfoot population of 39 feet. That angle was measured with goniometer aligned to the Achilles tendon and the axis of the calcaneus with center placement over the talus[76]. The tibia in the computational simulation was aligned vertical (normal to the ground plate), thus the apparent hindfoot angle with respect to the long axis of the tibia was 3.4° for the intact, and 6.4° for the flatfoot simulations.

The following morphological changes from the intact normal limb were observed in the simulated flatfoot: drop in the L-T1MT angle, diminishing L-CP, plantarflexion of the talus seen with L-TC angle, uncovering of the talonavicular joint surface with AP-TN abduction, abduction of the forefoot from the AP-T1MT angle, and hindfoot valgus. These changes all correlate to clinical signs of Stage II AAFD[67,70,72,73,76,85]. A study of 25 clinically presenting flatfoot subjects (39 feet) yielded a L-T1MT angle of 17.5° ± 6.4° of downward collapse (indicated as a negative value in our simulation); L-TC angle of 36.2° ± 30.5°; L-CP angle of 16.3° ± 6.3°; and a AP-TN angle of 22.3° ± 6.7° of abduction (indicated as a negative value in our simulation) with no reported AP-T1MT angle. The direction these measurements were seen to change from the normal foot to the diseased state was predicted in the flatfoot simulations, with the exception of L-TC which was seen to increase in simulation but decrease in clinical findings, although standard deviations were extremely large. The increasing L-TC angle seen in our simulation is an indicator of talar plantarflexion, which other investigators[67,69,70] corroborate as a key feature of adult acquired flatfoot deformity.

The MCO improved all joint angles with the exception of L-CP, which was likely influenced by the observed calcaneal varus rotation. Clinically, the MCO is used to stabilize the line of action of the Achilles tendon to eliminate the positive feedback mechanism for hindfoot valgus[74,98,99,94]. In this foot, simulation of the MCO reduced hindfoot valgus and brought the calcaneus into several degrees of varus (i.e. angle measure less than flatfoot), providing the same benefit as is sought clinically.

The LCL procedures also provided correction to these joint angles. Both surgical methods adjusted the L-T1MT angle to beyond intact levels creating a higher arch. The Evans procedure failed to prevent talar plantarflexion and contributed to the deformity slightly when considering L-TC angle, while the CCDA showed correction by imparting talar dorsiflexion. Clinically and experimentally, both the Evans and CCDA have been seen to improve L-T1MT angle[64,66,68,69,84,92] Talar plantarflexion also experiences a small correction for both procedures, but with a large standard deviation in the literature[68,92] which may explain the models' discrepancy for the Evans procedure. L-CP was restored to a higher than intact level with LCL procedures. Clinically and experimentally, L-CP has been seen to increase with either lateral column procedure[68,92].

The AP-T1MT and AP-TN forefoot abduction angles as well as L-T1MT angle were impacted the most by Evans and CCDA in the simulations. Clinically, these AP angles have received the most correction for AAFD by targeting the lateral column[64,66,68,69,84,92]. Calcaneal varus / valgus rotations for the Evans and CCDA were slightly improved over flatfoot to near normal intact levels. Measurements for hindfoot valgus changes for these bony procedures are not commonly reported although it is widely accepted that the MCO improves hindfoot valgus[70]. This was seen in the model as the only changes in this angle more than ~1.5° were when an

MCO was performed alone or in combination with a lateral column procedure – all of these angle changes were in a varus direction.

Evans & MCO and CCDA & MCO exhibited a blend of each procedures' separate effects in influencing joint angle change. Both methods demonstrated a middle ground effect on the L-T1MT angle, more improvement than MCO alone, but less than the LCL procedure alone. The L-TC measure of talar plantarflexion was unchanged with the opposing effects of Evans & MCO, while CCDA & MCO combined to dorsiflex the talus further than either had separately – again these effects were small in the model and clinically[68,92]. L-CP saw a similar interplay where the falling MCO and raising Evans resulted in a near intact normal angle. The CCDA & MCO however resulted in a pitch angle close to that of the original flatfoot. Both AP angles exhibited constructive interference with the combination procedures, again with the CCDA & MCO bringing greater adduction to the forefoot as measured by the AP-T1MT angle. The Evans & MCO exhibited greater adduction of the AP-TN angle. The forefoot corrections for these combination procedures were the greatest among all simulations. Finally, the addition of the MCO to either LCL procedure yielded more calcaneal varus rotation than either lateral column procedure alone, with the CCDA & MCO having the greatest varus rotation of all simulations. Currently, combination procedures such as these are somewhat common, with the MCO treating hindfoot valgus and LCL correcting forefoot abduction[66,67,70,74] but reports of angular corrections are not readily available.

Ligament Strain: The model simulations suggest that the lateral column lengthening procedures also lengthen the lateral portions of the long plantar ligament and plantar fascia, which cross both the Evans and CCDA sites, as does the MCO. The simulations showed more than doubling of strain values in the lateral portions of the long plantar ligament, and a

slackening of the medial portions compared to flatfoot. This agrees with DiNucci et al.[91] where tightening was found in the lateral bands of the long plantar ligament while the medial portions were visibly slack. The model showed a decrease of more than 52% of the strain in the medial portions of the plantar fascia with the MCO and a drop of 66-73% with Evans and CCDA respectively. These findings agree with Horten et al.[58] who found that MCO and CCDA slackened the medial band of the plantar fascia, with a greater drop in strain attributed to the CCDA; no values were reported for lateral portions of the fascia in that study.

Calcaneocuboid Contact Load: LCL procedures are considered to be a likely cause of accelerated arthritic development in the mid and hindfoot, of particular note is the Evans osteotomy. The joint contact force in both model of Evans and Evans & MCO more than doubled as compared to levels at intact normal, intact flatfoot, or MCO alone. Cooper et al.[93] experimentally found a quadrupling of contact load at the calcanealcuboid joint, and clinical follow-up has discovered arthritic development in this joint after at follow-up with patients who received the Evans procedure[64,65,68].

Plantar Ground Loads: The flatfoot model showed a shifting of loading towards the 1st ray. This was overcorrected by the subsequent MCO, Evans, CCDA, and combination procedures to shift the load laterally, in most cases at least doubling 4th and 5th ray ground contact. Tien et al.[95] found an increase in cadaveric 5th metatarsal average *pressure* by 46% ± 42% (range -4% to 141%) for the Evans procedure, and 104% ± 58% (range 9% to 216%) for the CCDA. In the model, the contact *loads* increased by 100% at the 5th metatarsal for Evans and 122% for CCDA. Arangio et al.[89] experimentally found a drop in % bodyweight carried by the 1st metatarsal and an increase to the 4th and 5th metatarsals with the application of an MCO; this too agrees with the simulations' prediction of shift in body weight distribution. Hadfield et al.[94]

found a significant offloading of average pressure to the 1st and 2nd metatarsal heads with an MCO and a significant increase in lateral hindfoot pressure but no change to medial hindfoot pressure and a trend for an increased lateral forefoot forefoot pressure. In the absence of soft tissue, directly comparing pressure to simulated plantar loading can be problematic. The heel in the model made ground contact in one area of the calcaneus which area did shift slightly lateral as the calcaneus rolled in the varus direction and θ_6 changed from 96.4° to 87.7° from flatfoot to MCO states. This roll would likely result in similar pressure changes as seen experimentally[94] as more lateral regions of the heel pad are loaded. Scott et al.[96] found an increase in lateral forefoot pressures after both Evans and CCDA, with no significant difference between the procedures; in the model, 5th metatarsal contact loads were similar between the two procedures, 122N for Evans and 133N for CCDA.

Chapter 6 - Overall Discussion

The areas of research that could benefit from computational modeling are as diverse as the fields themselves. In the field of orthopaedics, these models continue to demonstrate their utility. Describing an accurately modeled anatomical system by digital means is a tremendous accomplishment alone in terms of storage, handling, and re-use of anatomy. The digital models take up very little space (a current solved simulation is approximately 20-30 megabytes of disk space, ready-to-run setups are ~7 megabytes) the storage of hundreds of reassembled anatomies would fit on a handful of digital discs – which do not require 24 hours to thaw. Related is the notion that the anatomy can be reused. Hundreds of surgical configurations can be performed on the exact same "specimen" or vastly different surgical studies can be performed across the same database of specimens over years. With improvements in software and our knowledge of the behavior of tissues, the resultant predictions from these models will continue to converge with live tissue behavior.

Of the computational methods, rigid body modeling suffers the same weaknesses of all computational models, a reliance on measured physical characteristics for input to modeling parameters such as stiffness values, *in situ* strains, fiber direction, and three-dimensional architecture. There are several similarities and differences between this method and the FEA model presented by Cheung et al.[3-8]. Both methods used high resolution medical scans to isolate bony geometry (here with CT, there with MR). Both methods add soft tissue behavior (here with elements arrays to simulate ligament and capsule, there with some ligaments individually addressed and others' behavior approximate through a soft tissue volume). Specific differences

occur in two areas; the material differences between FEA and rigid body simulation, and the target behavior of interest. The first is defined by the challenges associate with using the chosen simulation method. FEA has tremendous strength in calculating internal stress and strain, but suffers from prolonged computation time especially when computing large motions in a more dynamic model; and in nonlinear analyses with multiple 3D contact conditions for example. In contrast, the rigid body method is insensitive to internal stress and strain, but is aptly suited for calculating large construct kinematics very rapidly. The second area of difference is concerned with behavior studied, for the FEA studies the focus was plantar soft tissue deformation (through stress/strain and contact area) and ligament strain for various footwear studies[3-5], surgical release of fascia[8], and sensitivity studies[6,7]. For the method presented in this work, the focus was joint movement, ligament strain, joint contact and plantar load distribution through rigid bony anatomy. This approach was applied to AAFD and the consequences of the disease as well as its surgical corrections; this was also coupled with prior comparison to construct and structural properties of the medial arch. Both sets of measurements are valuable to research and to answer questions in orthopaedics. The ability to measure these different quantities depends on the simulation technique used, though some overlap exists (such as with ligament strains).

Anatomy capture: The benefits of obtaining complete scan data were emphasized in the transition from the Visible Human Project's data sets to the in-house capture of leg and foot anatomy. The programs used – MIMICS and SolidWorks - were not designed by the same corporations which required a degree of finesse in processing the data from one to the other. By aligning the specimen with respect to the scan field, and obtaining neutral position of the ankle, much of the scan processing and model assembly hardships were avoided altogether.

Model creation in SolidWorks. Assembly of the bones in 3D space and building/connecting various indenters and ground plates for external control of the assembly was straightforward. Some of the greatest difficulties in preparing simulations were the creation of osteotomies. Surgical guidelines as discussed in the literature leave questions about osteotomy cut plane position and angle, as well as other bone dressing (how osteotomies are shaped) and fracture reducing issues (amount of fusion, precise bone placement). These are overcome in the surgical arena by mentoring and extensive practice. For an outside experimenter without years of practice in the operating room, re-creating these osteotomies was more difficult. Descriptions of "1cm posterior to the anterior facet" and "bulk of the posterior calcaneal tuberosity" were not SolidWorks input fields. Even without operating room experience, there are enough literature and book descriptions of these techniques available (including surgical residents to question) that the primary means and methods of creating these surgical repairs are anticipated to closely approximate common surgical technique. Creating various cut surfaces and wedges for procedures required the addition of a framework of reference geometry to the bones to describe the surgical guidelines for such procedures. Once this framework was in place, such procedures could be simulated. This leads to the potential necessity of either close collaboration of simulators and surgeons, or the availability of a vast quantity of post surgical scan data for statistical analysis of technique. Most likely, a combination of these methods will yield the best results.

Simulation in COSMOSMotion. The progression from spring elements to action reaction elements was delayed early by slack length issues and adequate soft tissue modeling. As *in situ* strains were added, they first were wholly ineffective in generating a pre-strained state in tissues, but did act to reduce joint gaps somewhat. This early closure stabilized both spring and tension

only models even though it was not immediately recognized as doing so. With development of the final models, the deficiency of maintaining the *in situ* strains were first addressed with iterative reduction of joint gaps by refreshing the pre-strain. A more robust final solution was found in the combination of mild iterative reduction and slight scaling of bony size.

Adequate soft tissue modeling was a challenge on two fronts. Increasing the size of element arrays to define a single anatomical structure with multiple "fibers" was a trade between reducing computation time and failure with shorter times to equilibrium, and increasing computation time due to complexity as well as modeler effort in defining and updating the increasing list of element functions. The author foresees the potential of future research in this area to utilize custom programming to automate much of this complexity; it was a difficult balance in the development stage. The behavior of these soft tissues, from a perspective of tension/compression springs vs. tension only elements with action reaction forces (once it could be successfully implemented) –was a straightforward and readily logical choice. The reported studies on stiffness and slack length were very helpful but incomplete. Further data was considered from more common sources such as ligament modulus of elasticity, but this required detailed information about ligament cross sectional area – information that was just as incomplete and error prone in the literature as stiffness. The tensile behavior of ligaments demonstrates a toe region before entering into a linear region, whereas a linear stiffness was assumed for ligament tensile behavior in the computational models. The literature reports that the in situ strain of ligaments in the beginning of the linear region is between 3-5%[9,36-39]. Study of the wrist and ankle has demonstrated that many of these ligaments are in strain beyond the toe region in the neutral position[35,41]. Further, the toe region is very sensitive to experimental testing protocols, such as tare load, and data in this region is not sufficiently quantified. Thus, a linear

stiffness was the most appropriate choice. The concept of considering the toe region of tissue behavior leads to the prospect of creating bi-linear behavior of the tension only expressions. This was considered and briefly explored for the model. Using a more detailed function expression, a toe region can be created to describe a more true three phase behavior (slack, toe, linear region – example of this is given in Appendix III). However, this more complex behavior is less supported by quantitative measures in literature than the previous method, and was thus not adopted in this model.

The literature leaves much to be desired in terms of quantitative behavior of the entire network of ligaments for the foot and ankle. Challenges due to the small size of ankle tissues have long retarded the exhaustive study of the individual components of the foot and ankle in vitro. Even with these deficiencies, this model has demonstrated an ability to use high resolution 3D geometry and reported ligament properties to create results that are in close agreement with many reported experimental findings.

An additional area for improvement lies with the inclusion of muscular action on the target joint. For the foot, the Achillies tendon was easily added due to its simple line of action to the calcaneus. Most other foot muscle, notably the posterior tibial tendon which is seen to play a role in flatfoot, act on the foot at several locations as their tendon bodies wrap around anatomy. This behavior is similar to the ligament wrapping discussed in earlier chapters. The difficulty here is preserving the tension in the muscle elements while adding their stability to the various joints they cross in various sheathes and retinacula. Those tendon paths in fact are much more extensive 3D paths than the wrapping considered for the plantar ligament and plantar fascia. Adding such elements was explored with the addition of sheath-simulating guide features which were manually added to bone, to direct the force of the tendon along its path. The addition of

these pathways and additional tendon elements was successfully, but imparting their behavior lead to some simulation instability and overall poor performance. Images of this technique are given in Appendix VI.

Experimental Validation. The predictive power of the final model variations was tested with consideration to experimental findings of arch stability granted by plantar structures, ligament strains in the presence of fascia release, and a multitude of experimental and clinical findings related to aspects of AAFD and its corrections.

Arch Stability: An additional strength of the developed computational models is the measurement of other parameters of interest such as ligament loads in the various injured states. Experimentally, the ultimate loads of ligaments have been measured, such as the plantar fascia at 1189 ± 244N [20]. In the computational simulation of arch stability the plantar fascia was not seen to exceed 400N, suggesting that with either one of the spring or plantar ligaments transected, this tissue will not suffer failure under one cycle of stance loading. Likewise, the tibio-spring part of the spring ligament, which originates from the medial/anterior angle of the distal tibia and inserts into the bulk of the anterior posterior spring ligament complex, is reported to have a yield load of 351 ± 231N [23]. When considering all the single and dual structure deficient simulations, these modeled spring ligament bands experienced a maximum of 258N of load, which falls within the standard deviation of reported yield. This may be further exacerbated by cyclic loading to damage the spring ligament over time. The plantar ligament, being a deep and complex band of tissues, is not easily measured experimentally and thus no experimental values are available for comparison. However, due to its robust size – less than the plantar fascia, but more than the tibio-spring and spring ligaments – a yield load can be estimated between that of the plantar fascia and spring ligament portion. In the computational model, the

maximum load in the plantar ligament during all simulations was nearly 600N when the plantar fascia was transected, which is almost twice the yield load of the spring ligament portion, but half that of the plantar fascia. Thus, under these conditions the plantar ligament could well be at risk for chronic damage.

Flatfoot Simulations. This computational model is an aid in understanding the complex weave of cause and effect seen with these surgical complication precursors. Joint angle corrections, which influence or are influenced by soft tissue tension, conspire in some manner to alter gait characteristics. Some side effects of this include the commonly seen complications, fixation failure, accelerated joint arthritis, and pain. This model successfully predicted the various clinical and experimental joint angles changes that result from these common surgical techniques, including agreement with the strengths of each technique. The soft tissue components of the model exhibited strain alterations across their bulk that correspond to experimental findings of how these tissues behave with lateral column procedures. Altered ground contact was simulated in close agreement with experimental and clinical findings of these corrective procedures. The exact interplay between these various factors, which is still largely unknown, is difficult to unravel in the clinical population. Ellis et al.[24] found significantly higher lateral midfoot average pressures in patients with lateral foot pain, which is a significant correlative finding in the potential source of this pain. The degree of deformity for flatfoot in this model suggests that the standard sizes for the MCO and lateral column procedures would lead to overcorrection of deformity. When considering the range of flatfoot deformity from the literature, this suggests the importance of size choice when assessing deformity to avoid the related complications mentioned here. Future work both clinically and with computational

modeling as presented here, will further enlighten the community to the potential complications of these procedures and aid in the discovery of new treatments and tailoring of current ones.

The overall performance of the model was good, with most results falling very near or within reported standard deviations. The trends of plantar contribution to stability, ligament strain values from fascia release, flatfoot and corrected joint angle changes, medial to lateral ligament strain, and plantar load distribution were all very similar to reported findings, and complimented each other overall.

The notable exceptions were total arch deformation in the stability model and calcaneocuboid contact force in the osteotomy simulations of AAFD repair. A possible explanation for excessive arch deformation can lie either with the incomplete body of data reporting ligament behavior, or the level of modeled dissection when compared to experimental conditions. An area of weakness in the model is that it only models ligament and bone behavior; the effects of musculature, fatty tissue, and skin layers are totally absent from the simulation. This may describe a somewhat less-stiff overall structure, and certainly comes into play when analyzing ground contact distribution. Calcaneocuboid contact force was found to be several times higher in simulation than experimentally determined. Possible explanations include 3D contact parameters which may not be restrictive enough in allowing bony interference, improper choices of slack length for ligaments crossing the calcaneocuboid joint (recalling that such data are only available for major ankle structures), or modeled ligament linearity which may be inadequate to predict realistic load magnitudes. Even with such magnitude errors, the trends of these effects correctly predicted.

This model methodology, now established and verified within certain parameters, is set to take the next steps in comparison to more complex experimental simulations. With these further

simulations, additional data and relative changes unique to this model's predictive ability will be able to investigate the biomechanical consequences of numerous bony and soft tissue pathologies and repairs to the foot. The long-term goal of this computational modeling approach is for it to serve not only as a powerful research tool, but as a pre-surgical predictive planner for corrective procedures of the foot/ankle complex.

Literature Cited

Literature Cited

1. Halloran JP, Petrella AJ, Rullkoetter PJ. Explicit finite element modeling of total knee replacement mechanics. *J Biomech*. 2005;38(2):323-331.

2. Anderson DD, Goldsworthy JK, Li W, et al. Physical validation of a patient-specific contact finite element model of the ankle. *J Biomech*. 2007;40(8):1662-1669.

3. Cheung JT, Zhang M. A 3-dimensional finite element model of the human foot and ankle for insole design. *Arch Phys Med Rehabil*. 2005;86(2):353-358.

4. Cheung JT, Zhang M. Parametric design of pressure-relieving foot orthosis using statistics-based finite element method. *Med Eng Phys*. 2008;30(3):269-277.

5. Yu J, Cheung JT, Fan Y, et al. Development of a finite element model of female foot for high-heeled shoe design. *Clin Biomech (Bristol, Avon)*. 2008;23 Suppl 1:S31-38.

6. Cheung JT, Zhang M, An K. Effects of plantar fascia stiffness on the biomechanical responses of the ankle-foot complex. *Clin Biomech (Bristol, Avon)*. 2004;19(8):839-846.

7. Cheung JT, Zhang M, Leung AK, Fan Y. Three-dimensional finite element analysis of the foot during standing--a material sensitivity study. *J Biomech*. 2005;38(5):1045-1054.

8. Cheung JT, An K, Zhang M. Consequences of partial and total plantar fascia release: a finite element study. *Foot Ankle Int*. 2006;27(2):125-132.

9. Gill TJ, Van de Velde SK, Wing DW, et al. Tibiofemoral and patellofemoral kinematics after reconstruction of an isolated posterior cruciate ligament injury: in vivo analysis during lunge. *Am J Sports Med*. 2009;37(12):2377-2385.

10. Liu F, Kozanek M, Hosseini A, et al. In vivo tibiofemoral cartilage deformation during the stance phase of gait. *J Biomech*. 2010;43(4):658-665.

11. Wu J, Seon JK, Gadikota HR, et al. In situ forces in the anteromedial and posterolateral bundles of the anterior cruciate ligament under simulated functional loading conditions. *Am J Sports Med*. 2010;38(3):558-563.

12. Yu J, Cheung JT, Fan Y, et al. Development of a finite element model of female foot for high-heeled shoe design. *Clin Biomech (Bristol, Avon)*. 2008;23 Suppl 1:S31-38.

13. Anderst WJ, Tashman S. A method to estimate in vivo dynamic articular surface interaction. *J Biomech*. 2003;36(9):1291-1299.

14. Anderst W, Zauel R, Bishop J, Demps E, Tashman S. Validation of three-dimensional model-based tibio-femoral tracking during running. *Med Eng Phys*. 2009;31(1):10-16.

15. Bey MJ, Kline SK, Tashman S, Zauel R. Accuracy of biplane x-ray imaging combined with model-based tracking for measuring in-vivo patellofemoral joint motion. *J Orthop Surg Res*. 2008;3:38.

16. Bey MJ, Zauel R, Brock SK, Tashman S. Validation of a new model-based tracking technique for measuring three-dimensional, in vivo glenohumeral joint kinematics. *J Biomech Eng*. 2006;128(4):604-609.

17. Dao TT, Marin F, Ho Ba Tho MC. Sensitivity of the anthropometrical and geometrical parameters of the bones and muscles on a musculoskeletal model of the lower limbs. *Conf Proc IEEE Eng Med Biol Soc*. 2009;2009:5251-5254.

18. Lenaerts G, Bartels W, Gelaude F, et al. Subject-specific hip geometry and hip joint centre location affects calculated contact forces at the hip during gait. *J Biomech*. 2009;42(9):1246-1251.

19. Stief F, Kleindienst FI, Wiemeyer J, et al. Inverse dynamic analysis of the lower extremities during nordic walking, walking, and running. *J Appl Biomech*. 2008;24(4):351-359.

20. Remy CD, Thelen DG. Optimal estimation of dynamically consistent kinematics and kinetics for forward dynamic simulation of gait. *J Biomech Eng*. 2009;131(3):031005.

21. Richards CT. The kinematic determinants of anuran swimming performance: an inverse and forward dynamics approach. *J. Exp. Biol*. 2008;211(Pt 19):3181-3194.

22. Meyer AR, Wang M, Smith PA, Harris GF. Modeling initial contact dynamics during ambulation with dynamic simulation. *Med Biol Eng Comput*. 2007;45(4):387-394.

23. Edwards WB, Gillette JC, Thomas JM, Derrick TR. Internal femoral forces and moments during running: implications for stress fracture development. *Clin Biomech (Bristol, Avon)*. 2008;23(10):1269-1278.

24. Koehle MJ, Hull ML. A method of calculating physiologically relevant joint reaction forces during forward dynamic simulations of movement from an existing knee model. *J Biomech*. 2008;41(5):1143-1146.

25. Chao EYS, Armiger RS, Yoshida H, Lim J, Haraguchi N. Virtual Interactive Musculoskeletal System (VIMS) in orthopaedic research, education and clinical patient care. *J Orthop Surg Res*. 2007;2:2.

26. Lin H, Nakamura Y, Su F, et al. Use of virtual, interactive, musculoskeletal system (VIMS) in modeling and analysis of shoulder throwing activity. *J Biomech Eng*. 2005;127(3):525-530.

27. Chao EYS. Graphic-based musculoskeletal model for biomechanical analyses and animation. *Med Eng Phys*. 2003;25(3):201-212.

28. Liacouras PC, Wayne JS. Computational modeling to predict mechanical function of joints: application to the lower leg with simulation of two cadaver studies. *J Biomech Eng*. 2007;129(6):811-817.

29. Netter FH. *Atlas of Human Anatomy*. 4th ed. Philadelphia, PA: Saunders/Elsevier; 2006.

30. Sarrafian SK. *Anatomy of the Foot and Ankle: Descriptive, Topographic, Functional*. 2nd ed. Philadelphia: Lippincott; 1993.

31. Siegler S, Block J, Schneck CD. The mechanical characteristics of the collateral ligaments of the human ankle joint. *Foot Ankle*. 1988;8(5):234-242.

32. Hicks JH. The mechanics of the foot. II. The plantar aponeurosis and the arch. *J. Anat*. 1954;88(1):25-30.

33. Perry J. Anatomy and biomechanics of the hindfoot. *Clin. Orthop. Relat. Res*. 1983;(177):9-15.

34. Taniguchi A, Tanaka Y, Takakura Y, et al. Anatomy of the spring ligament. *J Bone Joint Surg Am*. 2003;85-A(11):2174-2178.

35. Nigg BM, Skarvan G, Frank CB, Yeadon MR. Elongation and forces of ankle ligaments in a physiological range of motion. *Foot Ankle*. 1990;11(1):30-40.

36. Butler DL, Kay MD, Stouffer DC. Comparison of material properties in fascicle-bone units from human patellar tendon and knee ligaments. *J Biomech*. 1986;19(6):425-432.

37. Blankevoort L, Kuiper JH, Huiskes R, Grootenboer HJ. Articular contact in a three-dimensional model of the knee. *J Biomech*. 1991;24(11):1019-1031.

38. Blankevoort L, Huiskes R, de Lange A. The envelope of passive knee joint motion. *J Biomech*. 1988;21(9):705-720.

39. Li G, Gil J, Kanamori A, Woo SL. A validated three-dimensional computational model of a human knee joint. *J Biomech Eng*. 1999;121(6):657-662.

40. Song Y, Debski RE, Musahl V, Thomas M, Woo SL. A three-dimensional finite element model of the human anterior cruciate ligament: a computational analysis with experimental validation. *J Biomech*. 2004;37(3):383-390.

41. Savelberg HH, Kooloos JG, Huiskes R, Kauer JM. Strains and forces in selected carpal ligaments during in vitro flexion and deviation movements of the hand. *J. Orthop. Res*. 1992;10(6):901-910.

42. Kitaoka HB, Luo ZP, Growney ES, Berglund LJ, An KN. Material properties of the plantar aponeurosis. *Foot Ankle Int*. 1994;15(10):557-560.

43. Pfaeffle HJ, Tomaino MM, Grewal R, et al. Tensile properties of the interosseous membrane of the human forearm. *J. Orthop. Res*. 1996;14(5):842-845.

44. Liacouras PC, Virginia CU. Computational Modeling to Predict Mechanical Function of Joints: Validations and Applications of Lower Leg Simulations. 2006.

45. The National Library of Medicines Visible Human Project. 2003. Available at: http://www.nlm.nih.gov/research/visible/visible_human.html [Accessed March 26, 2010].

46. Iaquinto J, Adelaar RS, Wayne JS. Simulation of contact gait in the cadaveric lower extremity using a novel below knee simulator. *Foot Ankle Int*. 2008;29(1):66-71.

47. Cailliet R, Cailliet R. *Foot and Ankle Pain*. 2nd ed. Philadelphia: Davis Co; 1983.

48. Kim W, Voloshin AS. Role of plantar fascia in the load bearing capacity of the human foot. *J Biomech*. 1995;28(9):1025-1033.

49. Wright DG, Rennels DC. A Study of the Elastic Properties of Plantar Fascia. *J Bone Joint Surg Am*. 1964;46:482-492.

50. Mosier SM, Pomeroy G, Manoli A. Pathoanatomy and etiology of posterior tibial tendon dysfunction. *Clin. Orthop. Relat. Res*. 1999;(365):12-22.

51. Badlissi F, Dunn JE, Link CL, et al. Foot musculoskeletal disorders, pain, and foot-related functional limitation in older persons. *J Am Geriatr Soc*. 2005;53(6):1029-1033.

52. Barrett SJ, O'Malley R. Plantar fasciitis and other causes of heel pain. *Am Fam Physician*. 1999;59(8):2200-2206.

53. Graves RH, Levin DR, Giacopelli J, White PR, Russell RD. Fluoroscopy-assisted plantar fasciotomy and calcaneal exostectomy: a retrospective study and comparison of surgical techniques. *J Foot Ankle Surg*. 1994;33(5):475-481.

54. Wolgin M, Cook C, Graham C, Mauldin D. Conservative treatment of plantar heel pain: long-term follow-up. *Foot Ankle Int*. 1994;15(3):97-102.

55. Deland JT, Arnoczky SP, Thompson FM. Adult acquired flatfoot deformity at the talonavicular joint: reconstruction of the spring ligament in an in vitro model. *Foot Ankle*. 1992;13(6):327-332.

56. Choi K, Lee S, Otis JC, Deland JT. Anatomical reconstruction of the spring ligament using peroneus longus tendon graft. *Foot Ankle Int*. 2003;24(5):430-436.

57. Crary JL, Hollis JM, Manoli A. The effect of plantar fascia release on strain in the

spring and long plantar ligaments. *Foot Ankle Int*. 2003;24(3):245-250.

58. Horton GA, Myerson MS, Parks BG, Park YW. Effect of calcaneal osteotomy and lateral column lengthening on the plantar fascia: a biomechanical investigation. *Foot Ankle Int*. 1998;19(6):370-373.

59. Huang CK, Kitaoka HB, An KN, Chao EY. Biomechanical evaluation of longitudinal arch stability. *Foot Ankle*. 1993;14(6):353-357.

60. Jennings MM, Christensen JC. The effects of sectioning the spring ligament on rearfoot stability and posterior tibial tendon efficiency. *J Foot Ankle Surg*. 2008;47(3):219-224.

61. Jerosch J, Schunck J, Liebsch D, Filler T. Indication, surgical technique and results of endoscopic fascial release in plantar fasciitis (E FRPF). *Knee Surg Sports Traumatol Arthrosc*. 2004;12(5):471-477.

62. Kitaoka HB, Luo ZP, An KN. Effect of plantar fasciotomy on stability of arch of foot. *Clin. Orthop. Relat. Res.* 1997;(344):307-312.

63. Murphy GA, Pneumaticos SG, Kamaric E, et al. Biomechanical consequences of sequential plantar fascia release. *Foot Ankle Int*. 1998;19(3):149-152.

64. Hintermann B, Valderrabano V, Kundert HP. Lengthening of the lateral column and reconstruction of the medial soft tissue for treatment of acquired flatfoot deformity associated with insufficiency of the posterior tibial tendon. *Foot Ankle Int*. 1999;20(10):622-629.

65. Moseir-LaClair S, Pomeroy G, Manoli A. Intermediate follow-up on the double osteotomy and tendon transfer procedure for stage II posterior tibial tendon insufficiency. *Foot Ankle Int*. 2001;22(4):283-291.

66. Tellisi N, Lobo M, O'Malley M, et al. Functional outcome after surgical reconstruction of posterior tibial tendon insufficiency in patients under 50 years. *Foot Ankle Int*. 2008;29(12):1179-1183.

67. Deland JT. Adult-acquired flatfoot deformity. *J Am Acad Orthop Surg*. 2008;16(7):399-406.

68. Thomas RL, Wells BC, Garrison RL, Prada SA. Preliminary results comparing two methods of lateral column lengthening. *Foot Ankle Int*. 2001;22(2):107-119.

69. van der Krans A, Louwerens JWK, Anderson P. Adult acquired flexible flatfoot, treated by calcaneocuboid distraction arthrodesis, posterior tibial tendon augmentation, and percutaneous Achilles tendon lengthening: a prospective outcome study of 20 patients. *Acta Orthop*. 2006;77(1):156-163.

70. Pinney SJ, Lin SS. Current concept review: acquired adult flatfoot deformity. *Foot*

Ankle Int. 2006;27(1):66-75.

71. Shibuya N, Ramanujam CL, Garcia GM. Association of tibialis posterior tendon pathology with other radiographic findings in the foot: a case-control study. *J Foot Ankle Surg*. 2008;47(6):546-553.

72. Richie DH. Biomechanics and clinical analysis of the adult acquired flatfoot. *Clin Podiatr Med Surg*. 2007;24(4):617-644, vii.

73. Lee MS, Vanore JV, Thomas JL, et al. Diagnosis and treatment of adult flatfoot. *J Foot Ankle Surg*. 2005;44(2):78-113.

74. Hiller L, Pinney SJ. Surgical treatment of acquired flatfoot deformity: what is the state of practice among academic foot and ankle surgeons in 2002? *Foot Ankle Int*. 2003;24(9):701-705.

75. Hogan JF. Posterior tibial tendon dysfunction and MRI. *J Foot Ankle Surg*. 1993;32(5):467-472.

76. Coughlin MJ, Kaz A. Correlation of Harris mats, physical exam, pictures, and radiographic measurements in adult flatfoot deformity. *Foot Ankle Int*. 2009;30(7):604-612.

77. Kitaoka HB, Alexander IJ, Adelaar RS, et al. Clinical rating systems for the ankle-hindfoot, midfoot, hallux, and lesser toes. *Foot Ankle Int*. 1994;15(7):349-353.

78. Hill K, Saar WE, Lee TH, Berlet GC. Stage II flatfoot: what fails and why. *Foot Ankle Clin*. 2003;8(1):91-104.

79. Marks RM, Long JT, Ness ME, Khazzam M, Harris GF. Surgical reconstruction of posterior tibial tendon dysfunction: prospective comparison of flexor digitorum longus substitution combined with lateral column lengthening or medial displacement calcaneal osteotomy. *Gait Posture*. 2009;29(1):17-22.

80. Greisberg J, Hansen ST, Sangeorzan B. Deformity and degeneration in the hindfoot and midfoot joints of the adult acquired flatfoot. *Foot Ankle Int*. 2003;24(7):530-534.

81. Wacker J, Calder JDF, Engstrom CM, Saxby TS. MR morphometry of posterior tibialis muscle in adult acquired flat foot. *Foot Ankle Int*. 2003;24(4):354-357.

82. Deland JT, de Asla RJ, Sung I, Ernberg LA, Potter HG. Posterior tibial tendon insufficiency: which ligaments are involved? *Foot Ankle Int*. 2005;26(6):427-435.

83. Emmerich J, Wülker N, Hurschler C. [Influence of the posterior tibial tendon on the medial arch of the foot: an in vitro kinetic and kinematic study]. *Biomed Tech (Berl)*. 2003;48(4):97-105.

84. Sangeorzan BJ, Mosca V, Hansen ST. Effect of calcaneal lengthening on

relationships among the hindfoot, midfoot, and forefoot. *Foot Ankle*. 1993;14(3):136-141.

85. Ledoux WR, Shofer JB, Ahroni JH, et al. Biomechanical differences among pes cavus, neutrally aligned, and pes planus feet in subjects with diabetes. *Foot Ankle Int*. 2003;24(11):845-850.

86. Hix J, Kim C, Mendicino RW, Saltrick K, Catanzariti AR. Calcaneal osteotomies for the treatment of adult-acquired flatfoot. *Clin Podiatr Med Surg*. 2007;24(4):699-719, viii-ix.

87. Bolt PM, Coy S, Toolan BC. A comparison of lateral column lengthening and medial translational osteotomy of the calcaneus for the reconstruction of adult acquired flatfoot. *Foot Ankle Int*. 2007;28(11):1115-1123.

88. Sands AK, Tansey JP. Lateral column lengthening. *Foot Ankle Clin*. 2007;12(2):301-308, vi-vii.

89. Arangio GA, Salathe EP. A biomechanical analysis of posterior tibial tendon dysfunction, medial displacement calcaneal osteotomy and flexor digitorum longus transfer in adult acquired flat foot. *Clin Biomech (Bristol, Avon)*. 2009;24(4):385-390.

90. Ellis SJ, Yu JC, Johnson AH, et al. Plantar pressures in patients with and without lateral foot pain after lateral column lengthening. *J Bone Joint Surg Am*. 2010;92(1):81-91.

91. Dinucci KR, Christensen JC, Dinucci KA. Biomechanical consequences of lateral column lengthening of the calcaneus: Part I. Long plantar ligament strain. *J Foot Ankle Surg*. 2004;43(1):10-15.

92. Logel KJ, Parks BG, Schon LC. Calcaneocuboid distraction arthrodesis and first metatarsocuneiform arthrodesis for correction of acquired flatfoot deformity in a cadaver model. *Foot Ankle Int*. 2007;28(4):435-440.

93. Cooper PS, Nowak MD, Shaer J. Calcaneocuboid joint pressures with lateral column lengthening (Evans) procedure. *Foot Ankle Int*. 1997;18(4):199-205.

94. Hadfield MH, Snyder JW, Liacouras PC, et al. Effects of medializing calcaneal osteotomy on Achilles tendon lengthening and plantar foot pressures. *Foot Ankle Int*. 2003;24(7):523-529.

95. Tien TR, Parks BG, Guyton GP. Plantar pressures in the forefoot after lateral column lengthening: a cadaver study comparing the Evans osteotomy and calcaneocuboid fusion. *Foot Ankle Int*. 2005;26(7):520-525.

96. Scott AT, Hendry TM, Iaquinto JM, et al. Plantar pressure analysis in cadaver feet after bony procedures commonly used in the treatment of stage II posterior tibial tendon insufficiency. *Foot Ankle Int*. 2007;28(11):1143-1153.

97. Guyton GP, Jeng C, Krieger LE, Mann RA. Flexor digitorum longus transfer and medial displacement calcaneal osteotomy for posterior tibial tendon dysfunction: a

middle-term clinical follow-up. *Foot Ankle Int*. 2001;22(8):627-632.

98. Myerson MS, Corrigan J. Treatment of posterior tibial tendon dysfunction with flexor digitorum longus tendon transfer and calcaneal osteotomy. *Orthopedics*. 1996;19(5):383-388.

99. Nyska M, Parks BG, Chu IT, Myerson MS. The contribution of the medial calcaneal osteotomy to the correction of flatfoot deformities. *Foot Ankle Int*. 2001;22(4):278-282.

100. Cheng HK, Lin C, Wang H, Chou S. Finite element analysis of plantar fascia under stretch-the relative contribution of windlass mechanism and Achilles tendon force. *J Biomech*. 2008;41(9):1937-1944.

Appendix I: Ankle and Foot Dissection

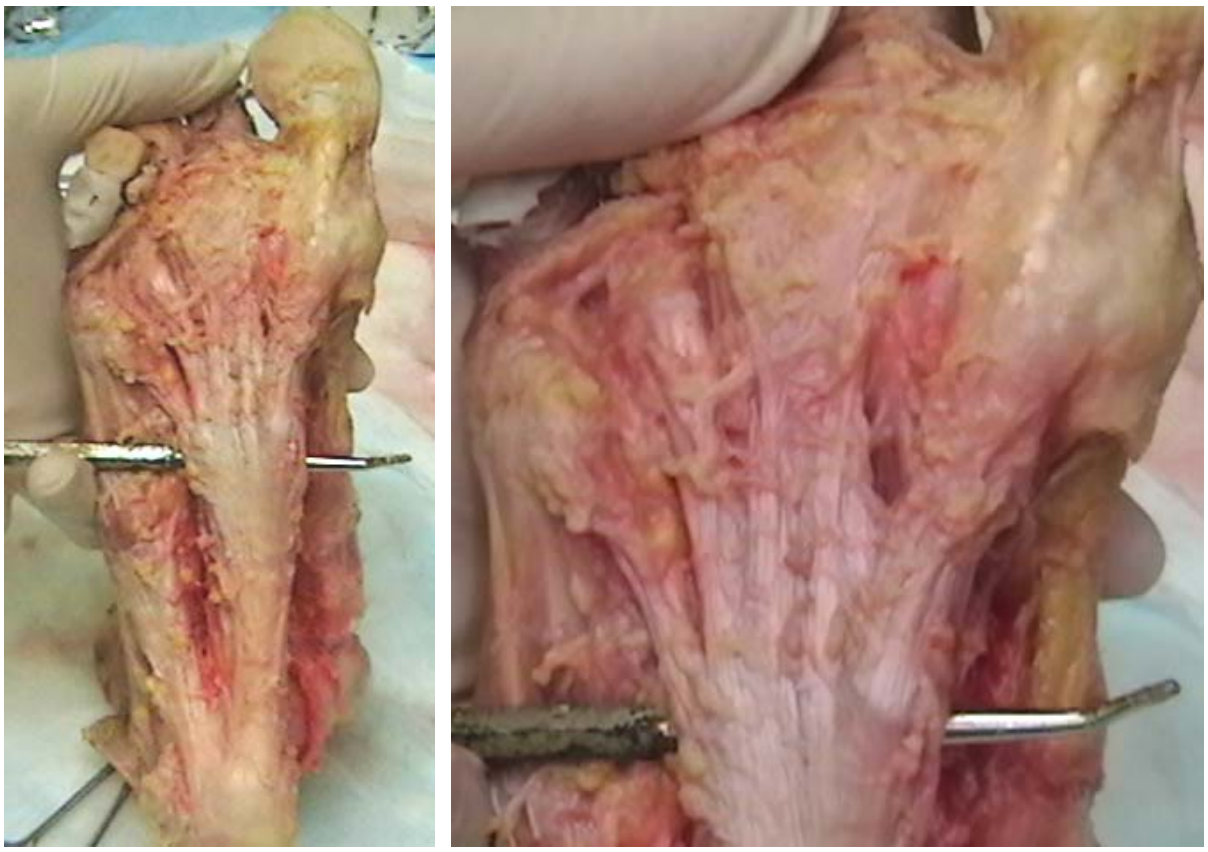

The plantar fascia exposed from calcaneal origin into metatarsal region, left. Close up view of the distal dispersion of the fibers into the forefoot, right.

(Left is anterior, bottom is lateral) Superficial portions of the plantar ligament, probe is approximately at the calcaneocuboid joint level.

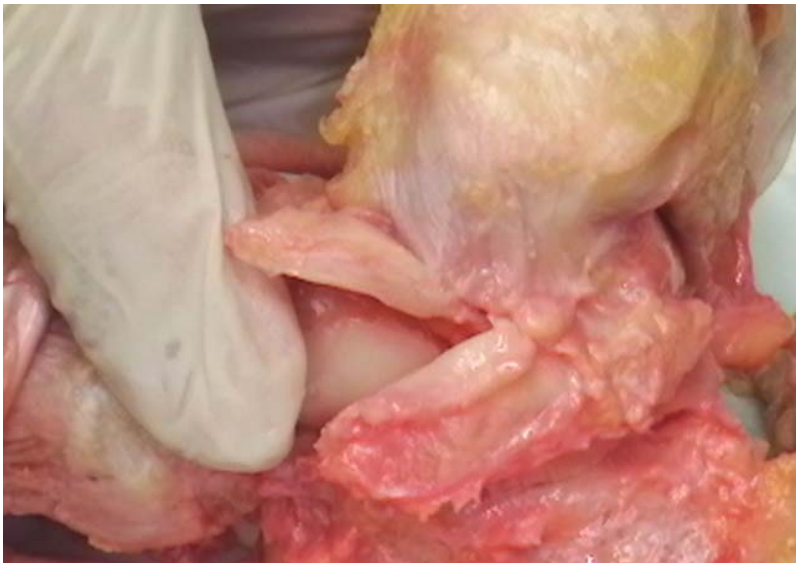

(Tibia is at the top, left is anterior, medial view) Edge-on cut of the robust deltoid ligament

Appendix II: Ligament Definition Spreadsheet

Ligament	Stiffness	Physical Length	Settle 1 Length	Settled 3 (Gen 5)	Marker 1	Marker 2
Anterior Talofibular	142	25.157	23.800	22.77	4323	4324
Anterior Tibiofibular 1	120	10.342	15.000	14.08	4325	4326
Anterior Tibiofibular 2	120	8.936	13.000	12.30	4327	4328
Anterior Tibiotalar part	90	13.421	12.100	11.13	4329	4330
Calcaneal Cubiod	90	15.880	15.600	14.64	4331	4332
Calcaneofibular 1	64	19.102	16.100	15.68	4333	4334
Calcaneofibular 2	64	17.630	14.000	14.60	4335	4336
Calcaneonavicular	120	21.481	19.200	19.08	4337	4338
Distal Intermetatarsal 5	90	15.931	15.710	15.86	4339	4340
Distal Intermetatarsal 6	90	9.934	9.300	9.63	4341	4342
Distal Intermetatarsal 7	90	11.099	10.700	10.93	4343	4344
Distal Intermetatarsal 8	90	21.431	20.300	20.80	4345	4346
Dorsal Calcanealcuboid 1	90	8.014	7.300	7.05	4347	4348
Dorsal Calcanealcuboid 2	90	8.533	7.900	7.83	4349	4350
Dorsal Cuboidenavicular	120	10.607	10.300	10.30	4353	4354
Dorsal Cuneocuboid 1	120	6.243	6.200	6.10	4351	4352
Dorsal Cuneocuboid 2	120	6.283	5.900	6.02	4355	4356
Dorsal Cuneonavicular 1	120	8.398	8.070	8.18	4357	4358
Dorsal Cuneonavicular 2	120	7.735	7.700	7.70	4359	4360
Dorsal Cuneonavicular 3	120	6.778	7.200	6.80	4361	4362
Dorsal Cuneonavicular 4	120	9.385	8.400	8.15	4363	4364
Dorsal Cuneonavicular 5	60	9.480	9.800	9.800	4369	4370
Dorsal Cuneonavicular 6	60	8.420	8.200	8.200	4371	4372
Dorsal Cuneonavicular 7	60	7.840	7.600	7.600	15875	15876
Dorsal Cuneonavicular 8	60	7.240	6.900	6.900	15877	15878
Dorsal Intercuneiform 1	120	5.850	5.300	5.34	4373	4374
Dorsal Intercuneiform 2	60	5.440	4.900	4.900	4375	4376
Dorsal Intercuneiform 3	60	5.320	6.000	6.000	15873	15874
Dorsal Metatarsal 1	90	4.974	4.400	4.40	4377	4378
Dorsal Metatarsal 2	90	5.571	5.800	5.69	4379	4380
Dorsal Metatarsal 3	90	4.848	4.800	4.79	4381	4382
Dorsal Metatarsal 4	90	7.125	7.700	7.85	4383	4384
Dorsal Talonavicular 1	120	4.868	5.200	3.71	4385	4386
Dorsal Talonavicular 2	120	6.312	6.200	6.20	4387	4388
Dorsal Tarsometatarsal 1	90	10.528	9.600	9.57	4389	4390
Dorsal Tarsometatarsal 10	90	6.342	7.500	7.29	4411	4412
Dorsal Tarsometatarsal 11	90	6.347	4.700	4.73	4413	4414
Dorsal Tarsometatarsal 12	90	13.113	10.000	8.98	4415	4416
Dorsal Tarsometatarsal 13	90	13.300	9.800	8.97	5639	5640
Dorsal Tarsometatarsal 14	90	10.870	7.600	7.600	5641	5642
Dorsal Tarsometatarsal 2	90	7.926	7.330	7.07	4391	4392
Dorsal Tarsometatarsal 3	90	5.588	5.700	5.63	4393	4394
Dorsal Tarsometatarsal 4	90	6.713	5.800	5.47	4395	4396
Dorsal Tarsometatarsal 5	90	6.166	6.400	6.35	4397	4398
Dorsal Tarsometatarsal 6	90	5.322	5.400	5.18	4399	4400
Dorsal Tarsometatarsal 7	90	7.428	8.100	7.93	4403	4404
Dorsal Tarsometatarsal 8	90	5.824	5.200	4.84	4405	4406
Dorsal Tarsometatarsal 9	90	4.959	5.200	5.52	4407	4408
Inferior Calcaneocuboid	90	6.210	4.900	5.25	4419	4420
IOM 1	126	20.367	14.000	13.94	4429	4430
IOM 2	126	27.130	19.000	19.11	4431	4432
IOM 3	126	26.437	18.000	18.35	4433	4434
IOM 4	126	20.482	14.000	14.42	4435	4436
IOM 5	126	14.350	10.000	9.50	4437	4438
IOM 6	126	9.837	6.800	6.67	4439	4440
IOM 7	126	6.606	6.800	6.59	4441	4442

Ligament	Stiffness	Settled 3 4% strain
Anterior Talofibular	142	IF(DM(4323,4324)-21.8592:0,0,-142*(DM(4323,4324)-21.8592)-0.1*VR(4323,4324))
Anterior Tibiofibular 1	120	IF(DM(4325,4326)-13.5168:0,0,-120*(DM(4325,4326)-13.5168)-0.1*VR(4325,4326))
Anterior Tibiofibular 2	120	IF(DM(4327,4328)-11.808:0,0,-120*(DM(4327,4328)-11.808)-0.1*VR(4327,4328))
Anterior Tibiotalar part	90	IF(DM(4329,4330)-10.6848:0,0,-90*(DM(4329,4330)-10.6848)-0.1*VR(4329,4330))
Calcaneal Cubiod	90	IF(DM(4331,4332)-14.0544:0,0,-90*(DM(4331,4332)-14.0544)-0.1*VR(4331,4332))
Calcaneofibular 1	64	IF(DM(4333,4334)-15.0528:0,0,-64*(DM(4333,4334)-15.0528)-0.1*VR(4333,4334))
Calcaneofibular 2	64	IF(DM(4335,4336)-14.016:0,0,-64*(DM(4335,4336)-14.016)-0.1*VR(4335,4336))
Calcaneonavicular	120	IF(DM(4337,4338)-18.3168:0,0,-120*(DM(4337,4338)-18.3168)-0.1*VR(4337,4338))
Distal Intermetatarsal 5	90	IF(DM(4339,4340)-15.2256:0,0,-90*(DM(4339,4340)-15.2256)-0.1*VR(4339,4340))
Distal Intermetatarsal 6	90	IF(DM(4341,4342)-9.2448:0,0,-90*(DM(4341,4342)-9.2448)-0.1*VR(4341,4342))
Distal Intermetatarsal 7	90	IF(DM(4343,4344)-10.4928:0,0,-90*(DM(4343,4344)-10.4928)-0.1*VR(4343,4344))
Distal Intermetatarsal 8	90	IF(DM(4345,4346)-19.968:0,0,-90*(DM(4345,4346)-19.968)-0.1*VR(4345,4346))
Dorsal Calcanealcuboid 1	90	IF(DM(4347,4348)-6.768:0,0,-90*(DM(4347,4348)-6.768)-0.1*VR(4347,4348))
Dorsal Calcanealcuboid 2	90	IF(DM(4349,4350)-7.5168:0,0,-90*(DM(4349,4350)-7.5168)-0.1*VR(4349,4350))
Dorsal Cuboidenavicular	120	IF(DM(4353,4354)-9.888:0,0,-120*(DM(4353,4354)-9.888)-0.1*VR(4353,4354))
Dorsal Cuneocuboid 1	120	IF(DM(4351,4352)-5.856:0,0,-120*(DM(4351,4352)-5.856)-0.1*VR(4351,4352))
Dorsal Cuneocuboid 2	120	IF(DM(4355,4356)-5.7792:0,0,-120*(DM(4355,4356)-5.7792)-0.1*VR(4355,4356))
Dorsal Cuneonavicular 1	120	IF(DM(4357,4358)-7.8528:0,0,-120*(DM(4357,4358)-7.8528)-0.1*VR(4357,4358))
Dorsal Cuneonavicular 2	120	IF(DM(4359,4360)-7.392:0,0,-120*(DM(4359,4360)-7.392)-0.1*VR(4359,4360))
Dorsal Cuneonavicular 3	120	IF(DM(4361,4362)-6.528:0,0,-120*(DM(4361,4362)-6.528)-0.1*VR(4361,4362))
Dorsal Cuneonavicular 4	120	IF(DM(4363,4364)-7.824:0,0,-120*(DM(4363,4364)-7.824)-0.1*VR(4363,4364))
Dorsal Cuneonavicular 5	60	IF(DM(4369,4370)-9.408:0,0,-60*(DM(4369,4370)-9.408)-0.1*VR(4369,4370))
Dorsal Cuneonavicular 6	60	IF(DM(4371,4372)-7.872:0,0,-60*(DM(4371,4372)-7.872)-0.1*VR(4371,4372))
Dorsal Cuneonavicular 7	60	IF(DM(15875,15876)-7.296:0,0,-60*(DM(15875,15876)-7.296)-0.1*VR(15875,15876))
Dorsal Cuneonavicular 8	60	IF(DM(15877,15878)-6.624:0,0,-60*(DM(15877,15878)-6.624)-0.1*VR(15877,15878))
Dorsal Intercuneiform 1	120	IF(DM(4373,4374)-5.1264:0,0,-120*(DM(4373,4374)-5.1264)-0.1*VR(4373,4374))
Dorsal Intercuneiform 2	60	IF(DM(4375,4376)-4.704:0,0,-60*(DM(4375,4376)-4.704)-0.1*VR(4375,4376))
Dorsal Intercuneiform 3	60	IF(DM(15873,15874)-5.76:0,0,-60*(DM(15873,15874)-5.76)-0.1*VR(15873,15874))
Dorsal Metatarsal 1	90	IF(DM(4377,4378)-4.224:0,0,-90*(DM(4377,4378)-4.224)-0.1*VR(4377,4378))
Dorsal Metatarsal 2	90	IF(DM(4379,4380)-5.4624:0,0,-90*(DM(4379,4380)-5.4624)-0.1*VR(4379,4380))
Dorsal Metatarsal 3	90	IF(DM(4381,4382)-4.5984:0,0,-90*(DM(4381,4382)-4.5984)-0.1*VR(4381,4382))
Dorsal Metatarsal 4	90	IF(DM(4383,4384)-7.536:0,0,-90*(DM(4383,4384)-7.536)-0.1*VR(4383,4384))
Dorsal Talonavicular 1	120	IF(DM(4385,4386)-3.5616:0,0,-120*(DM(4385,4386)-3.5616)-0.1*VR(4385,4386))
Dorsal Talonavicular 2	120	IF(DM(4387,4388)-5.952:0,0,-120*(DM(4387,4388)-5.952)-0.1*VR(4387,4388))
Dorsal Tarsometatarsal 1	90	IF(DM(4389,4390)-9.1872:0,0,-90*(DM(4389,4390)-9.1872)-0.1*VR(4389,4390))
Dorsal Tarsometatarsal 10	90	IF(DM(4411,4412)-6.9984:0,0,-90*(DM(4411,4412)-6.9984)-0.1*VR(4411,4412))
Dorsal Tarsometatarsal 11	90	IF(DM(4413,4414)-4.5408:0,0,-90*(DM(4413,4414)-4.5408)-0.1*VR(4413,4414))
Dorsal Tarsometatarsal 12	90	IF(DM(4415,4416)-8.6208:0,0,-90*(DM(4415,4416)-8.6208)-0.1*VR(4415,4416))
Dorsal Tarsometatarsal 13	90	IF(DM(5639,5640)-8.6112:0,0,-90*(DM(5639,5640)-8.6112)-0.1*VR(5639,5640))
Dorsal Tarsometatarsal 14	90	IF(DM(5641,5642)-7.296:0,0,-90*(DM(5641,5642)-7.296)-0.1*VR(5641,5642))
Dorsal Tarsometatarsal 2	90	IF(DM(4391,4392)-6.7872:0,0,-90*(DM(4391,4392)-6.7872)-0.1*VR(4391,4392))
Dorsal Tarsometatarsal 3	90	IF(DM(4393,4394)-5.4048:0,0,-90*(DM(4393,4394)-5.4048)-0.1*VR(4393,4394))
Dorsal Tarsometatarsal 4	90	IF(DM(4395,4396)-5.2512:0,0,-90*(DM(4395,4396)-5.2512)-0.1*VR(4395,4396))
Dorsal Tarsometatarsal 5	90	IF(DM(4397,4398)-6.096:0,0,-90*(DM(4397,4398)-6.096)-0.1*VR(4397,4398))
Dorsal Tarsometatarsal 6	90	IF(DM(4399,4400)-4.9728:0,0,-90*(DM(4399,4400)-4.9728)-0.1*VR(4399,4400))
Dorsal Tarsometatarsal 7	90	IF(DM(4403,4404)-7.6128:0,0,-90*(DM(4403,4404)-7.6128)-0.1*VR(4403,4404))
Dorsal Tarsometatarsal 8	90	IF(DM(4405,4406)-4.6464:0,0,-90*(DM(4405,4406)-4.6464)-0.1*VR(4405,4406))
Dorsal Tarsometatarsal 9	90	IF(DM(4407,4408)-5.2992:0,0,-90*(DM(4407,4408)-5.2992)-0.1*VR(4407,4408))
Inferior Calcaneocuboid	90	IF(DM(4419,4420)-5.04:0,0,-90*(DM(4419,4420)-5.04)-0.1*VR(4419,4420))
IOM 1	126	IF(DM(4429,4430)-13.3824:0,0,-126*(DM(4429,4430)-13.3824)-0.1*VR(4429,4430))
IOM 2	126	IF(DM(4431,4432)-18.3456:0,0,-126*(DM(4431,4432)-18.3456)-0.1*VR(4431,4432))
IOM 3	126	IF(DM(4433,4434)-17.616:0,0,-126*(DM(4433,4434)-17.616)-0.1*VR(4433,4434))
IOM 4	126	IF(DM(4435,4436)-13.8432:0,0,-126*(DM(4435,4436)-13.8432)-0.1*VR(4435,4436))
IOM 5	126	IF(DM(4437,4438)-9.12:0,0,-126*(DM(4437,4438)-9.12)-0.1*VR(4437,4438))
IOM 6	126	IF(DM(4439,4440)-6.4032:0,0,-126*(DM(4439,4440)-6.4032)-0.1*VR(4439,4440))
IOM 7	126	IF(DM(4441,4442)-6.3264:0,0,-126*(DM(4441,4442)-6.3264)-0.1*VR(4441,4442))

Ligament	Stiffness	Physical Length	Settle 1 Length	Settled 3 (Gen 5)	Marker 1	Marker 2
Interosseus Talocalcaneal 1	90	8.901	7.700	7.97	4421	4422
Interosseus Talocalcaneal 2	90	6.559	5.400	6.27	4423	4424
Interosseus Talocalcaneal 3	90	5.701	4.200	5.16	4425	4426
Lateral Talocalcaneal	90	4.985	4.100	4.45	4449	4450
PL1 Distal	40	28.54	25.500	26.32	11449	11450
PL1 Proximal	40	39.83	36.000	37	11451	11452
PL2 Distal	40	28.58	27.000	27.43	11453	11454
PL2 Proximal	40	45.04	40.000	41.68	11455	11456
PL3 Distal	40	25.13	22.000	23.16	11457	11458
PL3 Proximal	40	48.42	44.000	46.23	11459	11460
PL4 Distal	40	24	22.000	22.3	11461	11462
PL4 Proximal	40	59.18	54.800	56.64	11463	11464
PL5 Distal	40	15.41	14.000	14.3	11465	11466
PL5 Proximal	40	56.03	52.000	53.88	11467	11468
PL6 Distal	40	18.33	17.000	17.31	11469	11470
PL6 Proximal	40	52.7	48.600	50.34	11471	11472
Long Plantar Ligament 5-1	40	47.270	42.000	43.70	5429	5430
Long Plantar Ligament 5-2	40	55.640	50.000	52.20	5431	5432
Medial Talocalcaneal	120	9.602	7.800	8.27	4471	4472
Planar Cuneocuboid 1	90	12.558	11.900	12.15	4473	4474
Planar Cuneocuboid 2	90	9.304	9.370	9.23	4475	4476
Plantar Calcaneocuboid 1	90	28.220	26.300	27.10	4479	4480
Plantar Calcaneocuboid 2	90	47.195	40.700	41.78	4481	4482
Plantar Calcaneocuboid 3	90	46.228	38.800	40.15	4483	4484
ntar Calcaneonavicular (Spring	50	25.472	22.500	23.08	4487	4488
ntar Calcaneonavicular (Spring	50	22.576	20.100	20.83	4489	4490
ntar Calcaneonavicular (Spring	50	18.302	18.600	18.40	4491	4492
ntar Calcaneonavicular (Spring	50	18.566	16.900	17.97	4493	4494
Plantar CalcCub Capsule 1	90	8.680	8.500	8.57	5597	5598
Plantar CalcCub Capsule 2	90	7.870	7.000	7.31	5599	5600
Plantar CalcCub Capsule 3	90	8.130	6.400	6.88	5601	5602
Plantar Cuboideonavicular 1	90	23.266	18.000	17.90	4497	4498
Plantar Cuboideonavicular 2	90	23.450	19.000	18.91	4499	4500
Plantar Cuneonavicular 1	90	8.337	6.900	7.92	4501	4502
Plantar Cuneonavicular 2	90	5.500	3.900	3.900	4503	4504
Plantar Cuneonavicular 3	90	8.450	6.400	6.400	15881	15882
Plantar Fascia Base 1	40	67.660	63.000	64.87	5515	5516
Plantar Fascia Base 2	40	64.560	60.000	61.77	5517	5518
Plantar Fascia Base 3	40	62.510	58.000	59.86	5519	5520
Plantar Fascia Base 4	40	60.070	56.000	57.68	5521	5522
Plantar Fascia Base 5	40	59.750	56.000	57.43	5523	5524
Plantar Fascia End 1	60	69.550	63.000	65.65	5525	5526
Plantar Fascia End 2	50	74.070	69.000	71.06	5527	5528
Plantar Fascia End 3	50	70.730	65.000	67.15	5529	5530
Plantar Fascia End 4	20	64.560	61.000	62.04	5531	5532
Plantar Fascia End 5	20	57.660	52.000	53.25	5533	5534

Ligament	Stiffness	Settled 3 4% strain
Interosseus Talocalcaneal 1	90	IF(DM(4421,4422)-7.6512:0,0,-90*(DM(4421,4422)-7.6512)-0.1*VR(4421,4422))
Interosseus Talocalcaneal 2	90	IF(DM(4423,4424)-6.0192:0,0,-90*(DM(4423,4424)-6.0192)-0.1*VR(4423,4424))
Interosseus Talocalcaneal 3	90	IF(DM(4425,4426)-4.9536:0,0,-90*(DM(4425,4426)-4.9536)-0.1*VR(4425,4426))
Lateral Talocalcaneal	90	IF(DM(4449,4450)-4.272:0,0,-90*(DM(4449,4450)-4.272)-0.1*VR(4449,4450))
PL1 Distal	40	IF(DM(11449,11450)-25.2672:0,0,-40*(DM(11449,11450)-25.2672)-0.1*VR(11449,11450))
PL1 Proximal	40	IF(DM(11451,11452)-35.52:0,0,-40*(DM(11451,11452)-35.52)-0.1*VR(11451,11452))
PL2 Distal	40	IF(DM(11453,11454)-26.3328:0,0,-40*(DM(11453,11454)-26.3328)-0.1*VR(11453,11454))
PL2 Proximal	40	IF(DM(11455,11456)-40.0128:0,0,-40*(DM(11455,11456)-40.0128)-0.1*VR(11455,11456))
PL3 Distal	40	IF(DM(11457,11458)-22.2336:0,0,-40*(DM(11457,11458)-22.2336)-0.1*VR(11457,11458))
PL3 Proximal	40	IF(DM(11459,11460)-44.3808:0,0,-40*(DM(11459,11460)-44.3808)-0.1*VR(11459,11460))
PL4 Distal	40	IF(DM(11461,11462)-21.408:0,0,-40*(DM(11461,11462)-21.408)-0.1*VR(11461,11462))
PL4 Proximal	40	IF(DM(11463,11464)-54.3744:0,0,-40*(DM(11463,11464)-54.3744)-0.1*VR(11463,11464))
PL5 Distal	40	IF(DM(11465,11466)-13.728:0,0,-40*(DM(11465,11466)-13.728)-0.1*VR(11465,11466))
PL5 Proximal	40	IF(DM(11467,11468)-51.7248:0,0,-40*(DM(11467,11468)-51.7248)-0.1*VR(11467,11468))
PL6 Distal	40	IF(DM(11469,11470)-16.6176:0,0,-40*(DM(11469,11470)-16.6176)-0.1*VR(11469,11470))
PL6 Proximal	40	IF(DM(11471,11472)-48.3264:0,0,-40*(DM(11471,11472)-48.3264)-0.1*VR(11471,11472))
Long Plantar Ligament 5-1	40	IF(DM(5429,5430)-41.952:0,0,-40*(DM(5429,5430)-41.952)-0.1*VR(5429,5430))
Long Plantar Ligament 5-2	40	IF(DM(5431,5432)-50.112:0,0,-40*(DM(5431,5432)-50.112)-0.1*VR(5431,5432))
Medial Talocalcaneal	120	IF(DM(4471,4472)-7.9392:0,0,-120*(DM(4471,4472)-7.9392)-0.1*VR(4471,4472))
Planar Cuneocuboid 1	90	IF(DM(4473,4474)-11.664:0,0,-90*(DM(4473,4474)-11.664)-0.1*VR(4473,4474))
Planar Cuneocuboid 2	90	IF(DM(4475,4476)-8.8608:0,0,-90*(DM(4475,4476)-8.8608)-0.1*VR(4475,4476))
Plantar Calcaneocuboid 1	90	IF(DM(4479,4480)-26.016:0,0,-90*(DM(4479,4480)-26.016)-0.1*VR(4479,4480))
Plantar Calcaneocuboid 2	90	IF(DM(4481,4482)-40.1088:0,0,-90*(DM(4481,4482)-40.1088)-0.1*VR(4481,4482))
Plantar Calcaneocuboid 3	90	IF(DM(4483,4484)-38.544:0,0,-90*(DM(4483,4484)-38.544)-0.1*VR(4483,4484))
ıntar Calcaneonavicular (Sprinç	50	IF(DM(4487,4488)-22.1568:0,0,-50*(DM(4487,4488)-22.1568)-0.1*VR(4487,4488))
ıntar Calcaneonavicular (Sprinç	50	IF(DM(4489,4490)-19.9968:0,0,-50*(DM(4489,4490)-19.9968)-0.1*VR(4489,4490))
ıntar Calcaneonavicular (Sprinç	50	IF(DM(4491,4492)-17.664:0,0,-50*(DM(4491,4492)-17.664)-0.1*VR(4491,4492))
ıntar Calcaneonavicular (Sprinç	50	IF(DM(4493,4494)-17.2512:0,0,-50*(DM(4493,4494)-17.2512)-0.1*VR(4493,4494))
Plantar CalcCub Capsule 1	90	IF(DM(5597,5598)-8.2272:0,0,-90*(DM(5597,5598)-8.2272)-0.1*VR(5597,5598))
Plantar CalcCub Capsule 2	90	IF(DM(5599,5600)-7.0176:0,0,-90*(DM(5599,5600)-7.0176)-0.1*VR(5599,5600))
Plantar CalcCub Capsule 3	90	IF(DM(5601,5602)-6.6048:0,0,-90*(DM(5601,5602)-6.6048)-0.1*VR(5601,5602))
Plantar Cuboideonavicular 1	90	IF(DM(4497,4498)-17.184:0,0,-90*(DM(4497,4498)-17.184)-0.1*VR(4497,4498))
Plantar Cuboideonavicular 2	90	IF(DM(4499,4500)-18.1536:0,0,-90*(DM(4499,4500)-18.1536)-0.1*VR(4499,4500))
Plantar Cuneonavicular 1	90	IF(DM(4501,4502)-7.6032:0,0,-90*(DM(4501,4502)-7.6032)-0.1*VR(4501,4502))
Plantar Cuneonavicular 2	90	IF(DM(4503,4504)-3.744:0,0,-90*(DM(4503,4504)-3.744)-0.1*VR(4503,4504))
Plantar Cuneonavicular 3	90	IF(DM(15881,15882)-6.144:0,0,-90*(DM(15881,15882)-6.144)-0.1*VR(15881,15882))
Plantar Fascia Base 1	40	IF(DM(5515,5516)-62.2752:0,0,-40*(DM(5515,5516)-62.2752)-0.1*VR(5515,5516))
Plantar Fascia Base 2	40	IF(DM(5517,5518)-59.2992:0,0,-40*(DM(5517,5518)-59.2992)-0.1*VR(5517,5518))
Plantar Fascia Base 3	40	IF(DM(5519,5520)-57.4656:0,0,-40*(DM(5519,5520)-57.4656)-0.1*VR(5519,5520))
Plantar Fascia Base 4	40	IF(DM(5521,5522)-55.3728:0,0,-40*(DM(5521,5522)-55.3728)-0.1*VR(5521,5522))
Plantar Fascia Base 5	40	IF(DM(5523,5524)-55.1328:0,0,-40*(DM(5523,5524)-55.1328)-0.1*VR(5523,5524))
Plantar Fascia End 1	60	IF(DM(5525,5526)-63.024:0,0,-60*(DM(5525,5526)-63.024)-0.1*VR(5525,5526))
Plantar Fascia End 2	50	IF(DM(5527,5528)-68.2176:0,0,-50*(DM(5527,5528)-68.2176)-0.1*VR(5527,5528))
Plantar Fascia End 3	50	IF(DM(5529,5530)-64.464:0,0,-50*(DM(5529,5530)-64.464)-0.1*VR(5529,5530))
Plantar Fascia End 4	20	IF(DM(5531,5532)-59.5584:0,0,-20*(DM(5531,5532)-59.5584)-0.1*VR(5531,5532))
Plantar Fascia End 5	20	IF(DM(5533,5534)-51.12:0,0,-20*(DM(5533,5534)-51.12)-0.1*VR(5533,5534))

Ligament	Stiffness	Physical Length	Settle 1 Length	Settled 3 (Gen 5)	Marker 1	Marker 2
Plantar Fascia Lateral 1	40	60.320	56.000	56.000	4529	4530
Plantar Fascia Lateral 2	40	57.110	53.000	53.000	4531	4532
Plantar Intercuneio 1	90	7.783	6.100	6.21	4539	4540
Plantar Intercuneio 2	90	7.638	5.600	5.90	4541	4542
Plantar Intercuneio 3	90	8.680	6.100	6.100	4543	4544
Plantar Intercuneio 4	90	6.010	4.500	4.500	4545	4546
Plantar Intermetatarsal 1	90	9.277	8.900	8.85	4549	4550
Plantar Intermetatarsal 2	90	9.782	7.500	7.68	4551	4552
Plantar Intermetatarsal 3	90	8.142	6.200	6.03	4553	4554
Plantar Intermetatarsal 4	90	14.654	13.300	14.15	4555	4556
Plantar Tarsometatarsal 1	90	11.200	8.500	8.500	4559	4560
Plantar Tarsometatarsal 2	90	6.645	5.600	5.48	4561	4562
Plantar Tarsometatarsal 3	90	10.714	7.000	7.80	4563	4564
Plantar Tarsometatarsal 4	90	6.348	5.500	5.52	4565	4566
Plantar Tarsometatarsal 5	90	5.635	3.900	4.44	4567	4568
Plantar Tarsometatarsal 6	90	6.897	5.000	5.17	4569	4570
Plantar Tarsometatarsal 7	90	12.551	10.800	10.75	4571	4572
Plantar Tarsometatarsal 8	90	8.820	6.500	7.55	4573	4574
Plantar Tarsometatarsal 9	90	8.693	8.100	8.36	4575	4576
Plantar Tarsometatarsal 10	90	8.600	7.900	8.07	4577	4578
Plantar Tarsometatarsal 11	90	13.569	11.800	11.98	4579	4580
Posterior Talocalcaneal 1	90	6.421	5.800	5.28	4583	4584
Posterior Talocalcaneal 2	90	7.877	7.600	7.08	4585	4586
Posterior Talofibular 1	82	15.243	13.100	13.38	4587	4588
Posterior Talofibular 2	82	17.279	15.600	15.54	4589	4590
Posterior Tibiofibular	90	11.384	8.900	9.28	4593	4594
Posterior Tibiotalar Part 1	117	17.392	15.500	15.42	4595	4596
Posterior Tibiotalar Part 2	117	18.800	17.700	17.52	4597	4598
Proximal Tibiofibular 1	200	15.929	15.000	14.16	4599	4600
Proximal Tibiofibular 2	200	7.518	7.900	7.48	4601	4602
Proximal Tibiofibular 3	200	16.493	5.000	5.68	4623	4624
Proximal Tibiofibular 4	200	14.110	13.600	13.34	4903	4904
Proximal Tibiofibular 5	200	16.530	11.500	11.74	4905	4906
Proximal Tibiofibular 6	200	15.120	12.200	12.15	4907	4908
Superior Fibular Retinaculum 1	90	16.824	13.200	13.53	4607	4608
Superior Fibular Retinaculum 2	90	19.063	17.400	17.57	4609	4610
Tibiocalcaneal Part 1	200	25.961	22.000	22.30	4621	4622
Tibiocalcaneal Part 2	200	26.507	17.400	22.67	4623	4624
Tibionavicular Part 1	40	29.678	28.600	29.00	4625	4626
Tibionavicular Part 2	40	27.788	26.900	26.78	4627	4628
Tibiospring 1	200	22.810	18.100	18.93	4629	4630
Tibiospring 2	61	28.388	25.600	26.60	4631	4632

Ligament	Stiffness	Settled 3 4% strain
Plantar Fascia Lateral 1	40	IF(DM(4529,4530)-53.76:0,0,-40*(DM(4529,4530)-53.76)-0.1*VR(4529,4530))
Plantar Fascia Lateral 2	40	IF(DM(4531,4532)-50.88:0,0,-40*(DM(4531,4532)-50.88)-0.1*VR(4531,4532))
Plantar Intercuneio 1	90	IF(DM(4539,4540)-5.9616:0,0,-90*(DM(4539,4540)-5.9616)-0.1*VR(4539,4540))
Plantar Intercuneio 2	90	IF(DM(4541,4542)-5.664:0,0,-90*(DM(4541,4542)-5.664)-0.1*VR(4541,4542))
Plantar Intercuneio 3	90	IF(DM(4543,4544)-5.856:0,0,-90*(DM(4543,4544)-5.856)-0.1*VR(4543,4544))
Plantar Intercuneio 4	90	IF(DM(4545,4546)-4.32:0,0,-90*(DM(4545,4546)-4.32)-0.1*VR(4545,4546))
Plantar Intermetatarsal 1	90	IF(DM(4549,4550)-8.496:0,0,-90*(DM(4549,4550)-8.496)-0.1*VR(4549,4550))
Plantar Intermetatarsal 2	90	IF(DM(4551,4552)-7.3728:0,0,-90*(DM(4551,4552)-7.3728)-0.1*VR(4551,4552))
Plantar Intermetatarsal 3	90	IF(DM(4553,4554)-5.7888:0,0,-90*(DM(4553,4554)-5.7888)-0.1*VR(4553,4554))
Plantar Intermetatarsal 4	90	IF(DM(4555,4556)-13.584:0,0,-90*(DM(4555,4556)-13.584)-0.1*VR(4555,4556))
Plantar Tarsometatarsal 1	90	IF(DM(4559,4560)-8.16:0,0,-90*(DM(4559,4560)-8.16)-0.1*VR(4559,4560))
Plantar Tarsometatarsal 2	90	IF(DM(4561,4562)-5.2608:0,0,-90*(DM(4561,4562)-5.2608)-0.1*VR(4561,4562))
Plantar Tarsometatarsal 3	90	IF(DM(4563,4564)-7.488:0,0,-90*(DM(4563,4564)-7.488)-0.1*VR(4563,4564))
Plantar Tarsometatarsal 4	90	IF(DM(4565,4566)-5.2992:0,0,-90*(DM(4565,4566)-5.2992)-0.1*VR(4565,4566))
Plantar Tarsometatarsal 5	90	IF(DM(4567,4568)-4.2624:0,0,-90*(DM(4567,4568)-4.2624)-0.1*VR(4567,4568))
Plantar Tarsometatarsal 6	90	IF(DM(4569,4570)-4.9632:0,0,-90*(DM(4569,4570)-4.9632)-0.1*VR(4569,4570))
Plantar Tarsometatarsal 7	90	IF(DM(4571,4572)-10.32:0,0,-90*(DM(4571,4572)-10.32)-0.1*VR(4571,4572))
Plantar Tarsometatarsal 8	90	IF(DM(4573,4574)-7.248:0,0,-90*(DM(4573,4574)-7.248)-0.1*VR(4573,4574))
Plantar Tarsometatarsal 9	90	IF(DM(4575,4576)-8.0256:0,0,-90*(DM(4575,4576)-8.0256)-0.1*VR(4575,4576))
Plantar Tarsometatarsal 10	90	IF(DM(4577,4578)-7.7472:0,0,-90*(DM(4577,4578)-7.7472)-0.1*VR(4577,4578))
Plantar Tarsometatarsal 11	90	IF(DM(4579,4580)-11.5008:0,0,-90*(DM(4579,4580)-11.5008)-0.1*VR(4579,4580))
Posterior Talocalcaneal 1	90	IF(DM(4583,4584)-5.0688:0,0,-90*(DM(4583,4584)-5.0688)-0.1*VR(4583,4584))
Posterior Talocalcaneal 2	90	IF(DM(4585,4586)-6.7968:0,0,-90*(DM(4585,4586)-6.7968)-0.1*VR(4585,4586))
Posterior Talofibular 1	82	IF(DM(4587,4588)-12.8448:0,0,-82*(DM(4587,4588)-12.8448)-0.1*VR(4587,4588))
Posterior Talofibular 2	82	IF(DM(4589,4590)-14.9184:0,0,-82*(DM(4589,4590)-14.9184)-0.1*VR(4589,4590))
Posterior Tibiofibular	90	IF(DM(4593,4594)-8.9088:0,0,-90*(DM(4593,4594)-8.9088)-0.1*VR(4593,4594))
Posterior Tibiotalar Part 1	117	IF(DM(4595,4596)-14.8032:0,0,-117*(DM(4595,4596)-14.8032)-0.1*VR(4595,4596))
Posterior Tibiotalar Part 2	117	IF(DM(4597,4598)-16.8192:0,0,-117*(DM(4597,4598)-16.8192)-0.1*VR(4597,4598))
Proximal Tibiofibular 1	200	IF(DM(4599,4600)-13.5936:0,0,-200*(DM(4599,4600)-13.5936)-0.1*VR(4599,4600))
Proximal Tibiofibular 2	200	IF(DM(4601,4602)-7.1808:0,0,-200*(DM(4601,4602)-7.1808)-0.1*VR(4601,4602))
Proximal Tibiofibular 3	200	IF(DM(4623,4624)-5.4528:0,0,-200*(DM(4623,4624)-5.4528)-0.1*VR(4623,4624))
Proximal Tibiofibular 4	200	IF(DM(4903,4904)-12.8064:0,0,-200*(DM(4903,4904)-12.8064)-0.1*VR(4903,4904))
Proximal Tibiofibular 5	200	IF(DM(4905,4906)-11.2704:0,0,-200*(DM(4905,4906)-11.2704)-0.1*VR(4905,4906))
Proximal Tibiofibular 6	200	IF(DM(4907,4908)-11.664:0,0,-200*(DM(4907,4908)-11.664)-0.1*VR(4907,4908))
Superior Fibular Retinaculum 1	90	IF(DM(4607,4608)-12.9888:0,0,-90*(DM(4607,4608)-12.9888)-0.1*VR(4607,4608))
Superior Fibular Retinaculum 2	90	IF(DM(4609,4610)-16.8672:0,0,-90*(DM(4609,4610)-16.8672)-0.1*VR(4609,4610))
Tibiocalcaneal Part 1	200	IF(DM(4621,4622)-21.408:0,0,-200*(DM(4621,4622)-21.408)-0.1*VR(4621,4622))
Tibiocalcaneal Part 2	200	IF(DM(4623,4624)-21.7632:0,0,-200*(DM(4623,4624)-21.7632)-0.1*VR(4623,4624))
Tibionavicular Part 1	40	IF(DM(4625,4626)-27.84:0,0,-40*(DM(4625,4626)-27.84)-0.1*VR(4625,4626))
Tibionavicular Part 2	40	IF(DM(4627,4628)-25.7088:0,0,-40*(DM(4627,4628)-25.7088)-0.1*VR(4627,4628))
Tibiospring 1	200	IF(DM(4629,4630)-18.1728:0,0,-200*(DM(4629,4630)-18.1728)-0.1*VR(4629,4630))
Tibiospring 2	61	IF(DM(4631,4632)-25.536:0,0,-61*(DM(4631,4632)-25.536)-0.1*VR(4631,4632))

Appendix III: Bi-Linear ligament behavior

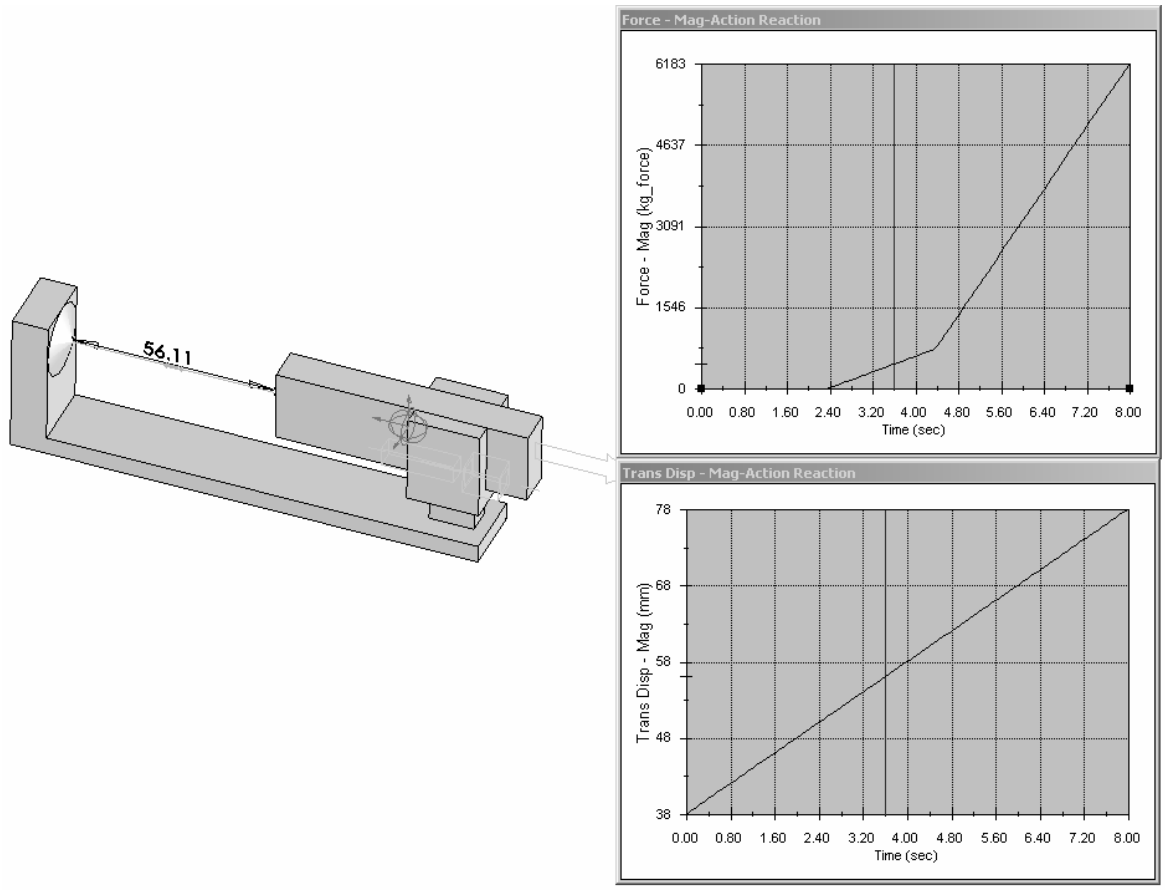

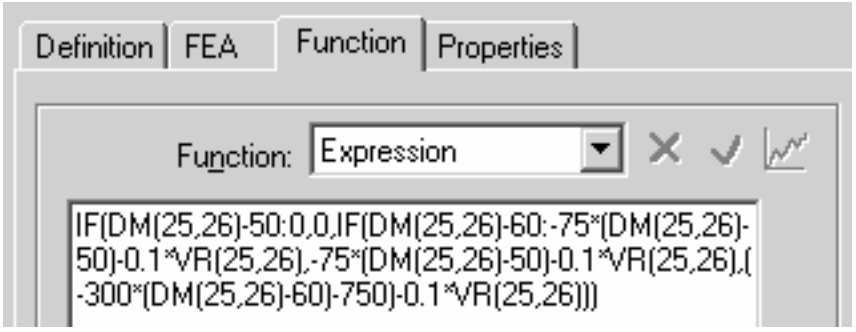

The bi-linear behavior is essentially a nested "if" statement in the function expression, bottom. This allows a simple test part (top left) to provide a slack, low-linear toe and high-linear region across a range of displacements (top right).

Appendix VI: Muscle Inclusion

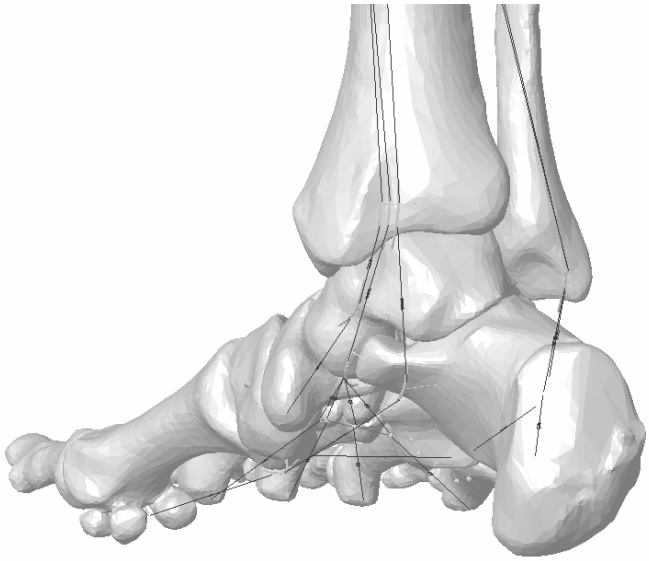

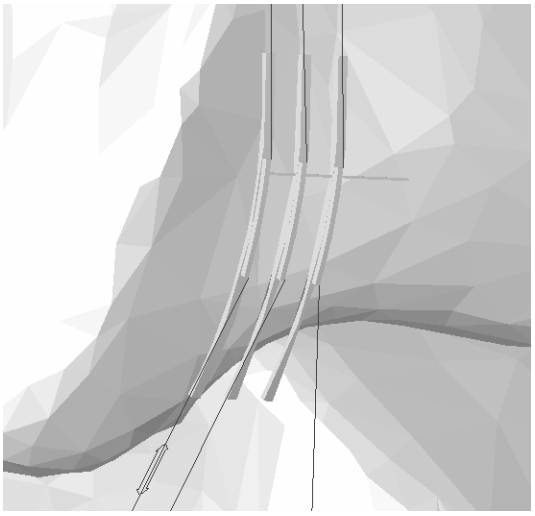

Musculature modeled for peroneal longus and brevis, flexor hallucis longus, flexor digitorum longus and tibiailis posterior. Wrapping at each bone level accomplished by a curved slider bar and slider shuttle. Distal tendon segments given high stiffness' to reflect the low elongation of these structures naturally.

VITA

Joseph Michael Iaquinto was born on September 13, 1982 in Fairfax, Virginia. He is a proud citizen of the United States of America. He graduated from Loudoun County High school in 2000; upon graduating he enrolled as an undergraduate in Biomedical Engineering at Virginia Commonwealth University where he received the degree of Bachelor of Science in the spring of 2004 and Master of Science in the summer of 2006. He has since continued at Virginia Commonwealth University to pursue his Doctoral degree in the developing field of orthopaedic computational simulation. In that time he has explored many roles including Resident Assistant (3 years), Resident Director (1 semester), Teaching Assistant (4+ years), and Research Assistant (2 years). He was a graphic designer and assistant experimenter on numerous basic science research projects. He was a co-author on two peer reviewed publications, and first author for two additional publications. He has presented at yearly meetings by the Bioengineering Division of ASME, as well as meetings hosted by the Orthopaedic Research Society. As part of his teaching experience he has taught undergraduate anatomy modules, demonstrated software, written assignments/laboratories/projects/exams and has given prepared lectures for numerous faculty professors. He was awarded the Alexander M. Clarke award for academic excellence in 2010. He has served on faculty search, tenure review, industry endowment, and departmental chair search committees. In his spare time he dabbles in various cooking techniques, practice and teaches the martial art of fencing, tells really lame jokes and uses a variety of small metal-joining techniques to explore sculpture. Upon graduation, he will prepare for and ultimately seek a faculty position to continue his interest in orthopaedic research and further his joy of teaching.